2013

Low Energy Tests of the Standard Model

Benjamin Carl Rislow
College of William & Mary - Arts & Sciences

Recommended Citation

Rislow, Benjamin Carl, "Low Energy Tests of the Standard Model" (2013). *Dissertations, Theses, and Masters Projects.* Paper 1539623625.
https://dx.doi.org/doi:10.21220/s2-enft-0z92

Low Energy Tests of the Standard Model

Benjamin Carl Rislow

Lewiston, Minnesota

Master of Science, The College of William and Mary, 2010
Bachelor of Arts, University of Minnesota, Morris, 2008

A Dissertation presented to the Graduate Faculty
of the College of William and Mary in Candidacy for the Degree of
Doctor of Philosophy

Department of Physics

The College of William and Mary
August, 2013

APPROVAL PAGE

This Dissertation is submitted in partial fulfillment of
the requirements for the degree of

Doctor of Philosophy

Benjamin Carl Rislow

Approved by the Committee, May, 2013

Committee Chair
Class of 1962 Professor Carl Carlson, Physics
The College of William and Mary

Chancellor Professor David Armstrong, Physics
The College of William and Mary

Associate Professor Joshua Erlich, Physics
The College of William and Mary

Assistant Professor Wouter Deconinck, Physics
The College of William and Mary

Theory Center Senior Staff, David Richards
Thomas Jefferson National Accelerator Facility

ABSTRACT

The Standard Model describes a wide range of fundamental interactions. Searches are ongoing for experimental results that differ from the Standard Model predictions. Such disagreements would both indicate that the Standard Model is incomplete and constrain the properties of New Physics scenarios. To probe the Standard Model over a wide kinematic range, low energy tests are necessary to complement experiments in the high energy regime. We perform calculations for experiments that are representative of two general types of low energy tests. The Qweak experiment at Jefferson Lab is a low energy measurement of the weak charge of the proton. Since the weak charge is proportional to the weak mixing angle, the result can be interpreted as a test of the Standard Model prediction that coupling parameters "run" as the energy of the interaction changes. To determine whether New Physics is present in the Qweak measurement, all Standard Model physics must be correctly accounted for. We present our calculation of a particularly troublesome radiative correction, the γZ box. We focus particularly on our models of the unmeasured structure functions $F_{1,2,3}^{\gamma Z}(x, Q^2)$ and discuss how they can be experimentally determined in the future. Atomic systems can also be used to test the Standard Model at low energies. Recently, there has been a discrepancy between the proton's charge radius extracted from electronic and muonic hydrogen measurements. This discrepancy could be a sign of New Physics for the muon and we present our model that bring the two radii extractions into agreement.

TABLE OF CONTENTS

CHAPTER

ACKNOWLEDGMENTS

I received a tremendous amount of professional and personal support while working on this dissertation. I thank my advisor, Carl Carlson, for his patience and guidance throughout my graduate career. I could not have completed the one loop derivation of the proton's weak charge without the enlightening comments of Michael Ramsey-Musolf and William Marciano. My understanding of the γZ box calculation was improved through conversations with Wally Melnitchouk, Peter Blunden, and Mikhail Gorchtein. I am grateful to all of them for taking time to help a lowly graduate student.

I thank the National Science Foundation for support under Grant Nos. PHY-0855618 and PHY-1205905. I also thank the Helmholtz Institute at the Johannes Gutenberg-Universität in Mainz for their hospitality during my stay in the fall of 2010.

Finally, I thank my friends and family for listening to my complaints and providing encouragement.

I present this dissertation in honor of my family.

LIST OF TABLES

LIST OF FIGURES

LOW ENERGY TESTS OF THE STANDARD MODEL

CHAPTER 1

Introduction

A naive reason to perform low energy tests of the Standard Model is that not all physicists can work at the Large Hadron Collider. A better reason to perform low energy tests of the Standard Model is that not all physicists should work at the Large Hadron Collider. Though high energies are indeed needed to produce and directly detect heavy particles, such particles should also appear in low energy processes through small but measurable loop effects. These low energy processes cannot be ignored. If the Standard Model is the theory that describes the way the world works, it must agree with experimental tests at all energies. We can only begin to resolve a complete picture of fundamental physics when the results of both high and low energy experiments are combined.

This introductory chapter is organized as follows. Sec. 1.1 introduces the basic elements of the Electroweak Lagrangian that are probed by low energy experiments. Secs. 1.2 and 1.3 provide an overview of two general types of low energy tests of the Standard Model. Sec. 1.2 describes how the Standard Model has definite predictions on how coupling and mass parameters should "run" as energies change. Discrepancies between the measured running and Standard Model prediction would indicate the presence of previously unaccounted for particles or interactions (New Physics). Much of this thesis will focus on the Qweak experiment at Jefferson Lab and the extraction of the running of the weak mixing angle. Sec. 1.3 describes measurements of the Lamb Shifts of electronic and muonic hydrogen. The Lamb Shift is a quantum field theory effect. Applying Standard Model physics to Lamb Shifts of both types of hydrogen allows for the extraction of the proton's charge radius. The present discrepancy between the extracted charge radii of electronic and muonic hydrogen may be the result of New Physics. Several New Physics proposals exist that "explain" the discrepancy.

1.1 Introduction to the Electroweak Lagrangian.

Low energy experiments can probe the Electroweak Lagrangian of the Standard Model. The Electroweak Lagrangian is a gauge theory that combines the $SU(2)_L$ and $U(1)_Y$ groups [1]. The interaction and kinetic terms for fermions and gauge bosons of the Electroweak Lagrangian are given by

$$\begin{aligned}
\mathcal{L}_{EW} &= \bar{\chi}_L \gamma^\mu \Big(i\partial_\mu - g\vec{T}\cdot\vec{W}_\mu - g'\frac{Y}{2}B_\mu \Big)\chi_L \\
&+ \bar{\psi}_R \gamma^\mu \Big(i\partial_\mu - g'\frac{Y}{2}B_\mu \Big)\psi_R \\
&- \frac{1}{4}\vec{W}_{\mu\nu}\cdot\vec{W}^{\mu\nu} - \frac{1}{4}B_{\mu\nu}B^{\mu\nu} \\
&= \bar{\chi}_L \gamma^\mu i\partial_\mu \chi_L - gJ^{i\mu}\cdot W^i_\mu - g'\frac{1}{2}j^{Y\mu}B_\mu \\
&+ \bar{\psi}_R \gamma^\mu i\partial_\mu \psi_R - g'\frac{1}{2}j^{Y\mu}B_\mu \\
&- \frac{1}{4}\vec{W}_{\mu\nu}\cdot\vec{W}^{\mu\nu} - \frac{1}{4}B_{\mu\nu}B^{\mu\nu}. \qquad (1.1)
\end{aligned}$$

In the above expression χ_L is a fermion doublet with left-handed chirality and ψ_R is a right-handed fermion singlet. $\vec{T}$ are the generators of $SU(2)_L$ and the hypercharge Y is the generator of $U(1)_Y$. $\vec{W}_\mu$ and B_μ are the gauge fields for $SU(2)_L$ and $U(1)_Y$, respectively. g and g' are the couplings between the fermions and gauge fields. $J^{i\mu}$ and $j^{Y\mu}$ are concise ways of expressing the weak and weak hypercharge currents:

$$\begin{aligned} J^{i\mu} &= \bar{\chi}_L \gamma^\mu T^i \chi_L, \\ j^{Y\mu} &= \bar{\psi}\gamma^\mu Y \psi. \end{aligned} \tag{1.2}$$

$\vec{W}_{\mu\nu}$ and $B_{\mu\nu}$ are given by

$$\begin{aligned} \vec{W}_{\mu\nu} &= \partial_\mu \vec{W}_\nu - \partial_\nu \vec{W}_\mu - g\vec{W}_\mu \times \vec{W}_\nu \\ B_{\mu\nu} &= \partial_\mu B_\nu - \partial_\nu B_\mu \end{aligned} \tag{1.3}$$

A gauge theory remains unchanged under internal, unmeasurable shifts in the fermion and gauge fields. In order for the Lagrangian to be invariant under the $SU(2)_L$ and $U(1)_Y$ transformations,

$$\begin{aligned} \chi_L &\to e^{i\vec{\alpha}(x)\cdot\vec{T}+i\beta(x)Y}\chi_L, \\ \psi_R &\to e^{i\beta(x)Y}\psi_R, \end{aligned} \tag{1.4}$$

the gauge fields, to leading order in $\vec{\alpha}$ and β, must concurrently transform as

$$\begin{aligned} \vec{W}_\mu &\to \vec{W}_\mu - \frac{1}{g}\partial_\mu\vec{\alpha} - \vec{\alpha} \times \vec{W}_\mu \\ B_\mu &\to B_\mu - \frac{1}{g'}\partial_\mu\beta. \end{aligned} \tag{1.5}$$

The above Lagrangian is a gauge invariant theory but work remains for it to be interpreted as a physical theory. To describe real physics, the gauge fields $\vec{W}_\mu$ and B_μ must be redefined in terms of the observed fields $W_\mu^\pm$, Z_μ, and A_μ.

$W^\pm$ bosons couple only to left-handed fermion doublets and their fields can be expressed as

$$W_\mu^\pm = \sqrt{\frac{1}{2}}(W^1 \mp iW^2)_\mu. \tag{1.6}$$

The charged current is defined as

$$J_\mu^\pm = \bar{\chi}_L \gamma_\mu \tau_\pm \chi_L \tag{1.7}$$

where $\tau_\pm = T_1 \pm iT_2 = 1/2(\tau_1 \pm i\tau_2)$ and τ are Pauli isospin matrices.

Z bosons and photons couple to both left- and right-handed fermions. It is thererfore necessary to mix the field that couples only to left-handed currents, W_μ^3, with the field that couples to both, B_μ. We define

$$A_\mu = B_\mu \cos\theta_W + W_\mu^3 \sin\theta_W \tag{1.8}$$

and

$$Z_\mu = -B_\mu \sin\theta_W + W_\mu^3 \cos\theta_W \tag{1.9}$$

where θ_W is the weak mixing angle.

We also identify the electromagnetic current as

$$j_\mu^{em} = J_\mu^3 + \frac{1}{2} j_\mu^Y, \tag{1.10}$$

or, in terms of the generators,

$$Q = T^3 + \frac{Y}{2}. \tag{1.11}$$

Substituting these values into the relevant part of the Lagrangian, we see

$$\begin{aligned} -gJ^3_\mu W^{3\mu} - \frac{g'}{2} j^Y_\mu B^\mu = &-\left(g \sin\theta_W J^3_\mu + g' \cos\theta_W \frac{j^Y_\mu}{2}\right) A^\mu \\ &- \left(g \cos\theta_W J^3_\mu - g' \sin\theta_W \frac{j^Y_\mu}{2}\right) Z^\mu \end{aligned} \tag{1.12}$$

Identifying $g \sin\theta_W = g' \cos\theta_W = e$, Eq. (1.12) becomes

$$-gJ^3_\mu W^{3\mu} - \frac{g'}{2} j^Y_\mu B^\mu = -ej^{em}_\mu A^\mu - \frac{g}{\cos\theta_W}(J^3_\mu - \sin^2\theta_W) Z^\mu \tag{1.13}$$

where $J^3_\mu - \sin^2\theta_W \equiv J^{NC}_\mu$.

The neutral current can be reexpressed as

$$\begin{aligned} J^{NC}_\mu Z^\mu &= \bar{\psi}_f \gamma_\mu \left[\frac{1}{2}(1-\gamma^5)T^3_f - \sin^2\theta_W Q_f\right] \psi_f Z^\mu \\ &= \bar{\psi}_f \gamma_\mu \frac{1}{2}\left[g^f_V - g^f_A \gamma^5\right] \psi_f Z^\mu \end{aligned} \tag{1.14}$$

where $g^f_V = T^3_f - 2Q_f \sin^2\theta_W$ and $g^f_A = T^3_f$.

The interaction and kinetic terms of the Electroweak Lagrangian describing real physics are now

$$
\begin{aligned}
\mathcal{L}_{EW} &= \bar{\chi}_L(i\gamma^\mu\partial_\mu)\chi_L + \bar{\psi}_R(i\gamma^\mu\partial_\mu)\psi_R \\
&- \frac{g}{\sqrt{2}}(J^{+\mu}W^+_\mu + J^{-\mu}W^-_\mu) \\
&- ej^{em\mu}A_\mu - \frac{g}{\cos\theta_W}J^{NC\mu}Z_\mu \\
&- \frac{1}{4}\vec{W}_{\mu\nu}\vec{W}^{\mu\nu} - \frac{1}{4}B_{\mu\nu}B^{\mu\nu}. \qquad (1.15)
\end{aligned}
$$

Mass terms for the fermions and gauge bosons are generated from spontaneous symmetry breaking of the ground state potential of the Higgs field. The $SU(2)_L \times U(1)_Y$ gauge invariant Lagrangian for the Higgs scalar doublet, ϕ, is

$$
\mathcal{L}_2 = \left| \left(i\partial_\mu - g\vec{T}\cdot\vec{W}_\mu - g'\frac{Y}{2}B_\mu \right)\phi \right|^2 - \mu^2\phi^\dagger\phi - \lambda(\phi^\dagger\phi)^2. \qquad (1.16)
$$

The last two terms of the above expression represent the potential of the Higgs field. For the case $\mu^2 < 0$ and $\lambda > 0$, the ground state of the potential does not occur at $\phi = 0$. In fact, there are an infinite number of minima distributed on a circle centered around $\phi = 0$. We are free to choose a minimum and by convention,

$$
\phi_0 = \sqrt{\frac{1}{2}}\begin{pmatrix} 0 \\ v \end{pmatrix}. \qquad (1.17)
$$

Here, v is the vacuum expectation value. Although the ground state is not symmetric, the overall symmetry (and gauge invariance) of the Lagrangian is preserved. Selecting a minimum out of an infinite number of minima is known as spontaneous symmetry breaking.

The part of Eq. (1.16) that generates mass terms is

$$\left|\left(g\vec{T}\cdot\vec{W}_\mu + g'\frac{Y=1}{2}B_\mu\right)\phi_0\right|^2 = \left(\frac{1}{2}vg\right)^2 W_\mu^+ W^{-\mu} + \frac{1}{8}v^2(gW_\mu^3 - g'B_\mu)^2 + 0(g'W_\mu^3 + gB_\mu)^2. \tag{1.18}$$

Identifying $\sin\theta_W = g'/\sqrt{g^2+g'^2}$ and $\cos\theta_W = g/\sqrt{g^2+g'^2}$, Eq. (1.18) becomes

$$\left|\left(g\vec{T}\cdot\vec{W}_\mu + g'\frac{Y=1}{2}B_\mu\right)\phi_0\right|^2 = \left(\frac{1}{2}vg\right)^2 W_\mu^+ W^{-\mu} + \frac{1}{8}(g^2+g'^2)v^2 Z_\mu^2 + 0A_\mu^2. \tag{1.19}$$

As desired, the photon is massless. The mass terms for the W and Z bosons are identified as $M_W = \frac{1}{2}vg$ and $M_Z = \frac{1}{2}v\sqrt{g^2+g'^2}$, respectively. Taking the ratio of these masses yields

$$\frac{M_W}{M_Z} = \cos\theta_W, \tag{1.20}$$

to leading order in perturbation theory. The next-to-leading order mass ratio is calculated in Chapter 2.

1.2 Low Energy Test of the Standard Model 1: Measurement of Coupling Running.

1.2.1 Tree Level Analysis of Electroweak Interactions

The Electroweak Lagrangian operates between initial and final states as a time-ordered exponential and produces a scattering amplitude multiplied by a four-momentumconserving δ-function,

$$i\mathcal{M}(2\pi)^4\delta^4(p_f - p_i) = \langle f|T\{e^{i\int d^4x\mathcal{L}(x)}\}|i\rangle. \tag{1.21}$$

This exponential must be expanded in a time-ordered power series. Each term represents a higher order in perturbation theory. The minimum number of orders required to produce an interaction is known as the "tree level" amplitude. For example, an unpolarized electron scattering off of an unpolarized proton via photon exchange can be described by the second order term,

$$\begin{aligned} i\mathcal{M}_\gamma(2\pi)^4\delta^4(p' + k' - p - k) = \langle e(k')p(p')|\frac{i^2}{2!}T\bigg\{ \int d^4x(-ie)\bar{\psi}(x)_p\gamma_\mu\psi_p(x)A^\mu(x) \\ \times \int d^4y(+ie)\bar{\psi}(y)_e\gamma_\nu\psi_e(y)A^\nu(y)\bigg\}|e(k)p(p)\rangle. \end{aligned} \tag{1.22}$$

Because there are two orderings, the factor of 1/2! can be dropped. After expanding the field operators and operating on the initial and final states, the amplitude becomes

$$i\mathcal{M}_\gamma = \bar{u}_{k',\lambda'}(ie\gamma^\mu)u_{k,\lambda}\frac{-ig_{\mu\nu}}{q^2 + i\epsilon}\bar{u}_{p',s'}(-ie\gamma^\nu)u_{p,s}. \tag{1.23}$$

By applying tree level analysis to electron proton scattering, the tree level coupling parameter, $\alpha = e^2/4\pi$, can in principle be determined.

1.2.2 Loops, Renormalization, and Running

As the orders of the exponential expansion increase in Eq. (1.21), the field operators begin forming loops. These loops produce divergent, momentum-dependent integrals. To cancel the divergences of the loops, the fields must be renormalized. They "absorb" the divergence, but the momentum dependence of the loops remains.

Couplings redefined to account for loop corrections are often referred to as effective couplings. The effective coupling is what is measured experimentally. The momentum dependence of the loops is what causes effective couplings to "run" from their tree level value.

For example, consider the expansion of a photon progagator. Because a photon propagator couples to fermions, it depends upon α. An expansion of the propagator can therefore be interpreted as a correction to the tree level value of α. The expansion, in terms of one loop corrections $\Pi(q^2)$, is

$$\begin{aligned}\frac{-i\alpha}{q^2+i\epsilon}+\frac{-i\alpha}{q^2+i\epsilon}(i\Pi(q^2))\frac{-i}{q^2+i\epsilon}+\ldots &= \frac{-i\alpha}{(q^2+i\epsilon)(1-\Pi(q^2))}\\ &= \frac{-iZ_3\alpha}{q^2+i\epsilon}\text{ (in } q^2\rightarrow 0 \text{ limit)}\end{aligned} \tag{1.24}$$

Renormalizing the field $A_\mu \rightarrow Z_3^{1/2}A_\mu^r$ absorbs the divergence of $\Pi(q^2)$ into the definition of the field. The kinetic energy term shifts to

$$-\frac{1}{4}(F_{\mu\nu})^2 \rightarrow -\frac{1}{4}(F_{\mu\nu}^r)^2-\frac{1}{4}\delta_3(F_{\mu\nu}^r)^2 \tag{1.25}$$

where $\delta_3 = Z_3 - 1$. The new term is the counterterm.

After renormalization the expansion up to one loop order is

$$\begin{aligned}\frac{-i\alpha}{q^2+i\epsilon}+\frac{-i\alpha}{q^2+i\epsilon}(i\Pi(q^2)-i\delta)\frac{-i}{q^2+i\epsilon}+\ldots &= \frac{-i\alpha}{q^2+i\epsilon-(\Pi(q^2)-\delta_3)}\\ &= \frac{-i\alpha}{q^2+i\epsilon}(1+(\Pi_2(q^2)-\delta_3)+\ldots),\end{aligned} \tag{1.26}$$

where $\Pi_2(q^2)$ indicates a single loop. δ_3 is a constant that subtracts away the divergence. There is not a unique choice for this subtraction. In the commonly used modified minimal subtraction ($\overline{MS}$) scheme, δ_3 is chosen to be equal to $\Pi_2(q^2)$ evaluated at a specific momentum. The choice of the subtracted momentum is known as the renormalization condition.

The effective value of alpha at one loop order is

$$\alpha_{eff}(q^2) = \alpha\big(1 + (\Pi_2(q^2) - \delta_3)\big). \tag{1.27}$$

Notice that the effective coupling is a function of the scheme-dependent choice of δ_3. When discussing effective couplings, one must make clear what renormalization scheme is being used. We will use the MS bar scheme in all of our analysis.

For momentum at the renormalization condition, all higher order loop corrections cancel. Thus, measurements at the renormalization condition isolate tree level masses and coupling parameters. Masses and coupling parameters run as the momentum of the exchanged boson evolves from that of the renormalization condition. The Electroweak Lagrangian predicts how the couplings run. Experiments at momentum away from the renormalization condition can be used to test the Standard Model prediction.

1.2.3 The Qweak Experiment: Extracting the Running of $\sin^2\theta_W$.

Different initial and final states isolate different parts of the Electroweak Lagrangian. In the illustrative example above we saw that unpolarized electron-proton scattering allows for the extraction of α. Suppose we now consider polarized electrons scattering off an unpolarized proton. When compared to protons, electrons are essentially massless. In the massless limit, chirality and helicity are equivalent. The neutral current for a massless electron becomes

$$\begin{aligned} J_\mu^{NC}|_e &= \bar{\psi}_f \gamma_\mu \frac{1}{2}[g_V^e - g_A^e \gamma^5]\psi_f \\ &\to \bar{\psi}_f \gamma_\mu \frac{1}{2}[g_V^e - g_A^e(2\lambda)]\psi_f, \end{aligned} \tag{1.28}$$

where $\lambda = \pm 1/2$ is the helicity of the incoming electron. For an unpolarized proton the parity-violating piece of the neutral current gets washed out,

$$J_\mu^{NC}|_p = \bar{\psi}_f \gamma_\mu \frac{1}{2} g_V^p \psi_f. \tag{1.29}$$

At tree level the proton's weak charge is defined as $Q_W^{p,LO} = 2g_V^p = 1 - 4\sin^2\theta_W$.

By scattering electrons of opposite helicity off an unpolarized proton and taking the difference, the combination $g_A^e g_V^p$ can be measured. Assuming $g_A^e = -1/2$, such parity-violating measurements can be used to extract the proton's weak charge and the weak mixing angle.

The renormalization condition of the weak mixing angle is often chosen at the Z-pole. Its value in the MS bar scheme is $\sin^2\theta_W(Q^2 = M_Z^2) = 0.2313$ [2]. The Qweak experiment at Jefferson Lab [3] measured parity-violating electron proton scattering at a momentum transfer of $Q^2 = 0.025$ GeV^2. The Qweak measurement is far from the Z-pole and can be used to test for discrepancies between experiment and the Standard Model prediction for the running of the weak mixing angle. Such discrepancies would indicate the presence of hitherto unaccounted for New Physics loop corrections.

The presence of New Physics effects can only be determined if the Standard Model loop corrections are correctly accounted for. In Chapter 2 we discuss the Standard Model expansion of Q_W^p to one loop order. The expansion is well-known, but an explicit derivation for all the terms is lacking in the literature. In Chapter 3 we focus on a particularly bothersome one loop correction, the γZ box. Several groups have studied this diagram and each has slightly different results due to differing treatments of γZ structure functions. In Chapter 4 we highlight how the PVDIS experimental result at Jefferson Lab [4] can be used as a first test of the differing treatments.

1.3 Low Energy Test of the Standard Model 2: Measurement of Muonic Hydrogen Lamb Shift.

1.3.1 The Proton Charge Radius and Its Contribution to the Lamb Shift

Atomic systems are natural laboratories for low energy tests of the Standard Model. The Lamb Shift between $2S$ and $2P$ orbitals is a quantum field effect. The energy of the electron in the $2S$ state is shifted due to the vacuum polarization of the photon exchanged between the electron and proton. Vacuum polarization occurs when the photon splits into a fermion-anti-fermion pair which annihilate into a photon. This polarization is not accounted for in relativistic quantum mechanics. Applying Standard Model physics to Lamb Shift measurements of hydrogen allows for the extraction of the proton's charge radius.

The lowest order contribution of the proton charge radius to the Lamb shift is in the exchange of a photon between the lepton and proton. The proton's charge radius is found by an examination of its form factors. For a point particle, $F_1(0) = 1$. Thus, the finite size contribution to the amplitude is

$$\mathcal{M} = \frac{e^2}{Q^2}\bar{u}(k')\gamma^\mu u(k)\bar{u}(p')\Big(\gamma_\mu\big(F_1(Q^2)-1\big) + \frac{i}{2M}\sigma_{\mu\nu}q^\nu F_2(Q^2)\Big)u(p), \tag{1.30}$$

where M is the proton mass and $q^2 = -Q^2$ is the square of the exchanged momentum. These form factors can be rewritten in terms of Sachs form factors,

$$\begin{aligned} G_E &\equiv F_1 + \frac{q^2}{4M^2} F_2 \\ G_M &\equiv F_1 + F_2. \end{aligned} \tag{1.31}$$

In the nonrelativistic limit the electronic Sachs form factor, $G_E(Q^2)$, represents the nucleon charge distribution in momentum space. It is expressed as a Fourier transformation

$$G_E(Q^2) = \int \rho(\vec{x}) e^{-\vec{q}\cdot\vec{x}} d^3x, \tag{1.32}$$

where $\rho(\vec{x})$ is the charge distribution in position space. Expanding this integral, the square of the charge radius is found to be

$$R_E^2 = \langle r_p^2 \rangle \equiv -6 \frac{dG_E(Q^2)}{dQ^2}\bigg|_{Q^2=0}. \tag{1.33}$$

Eq. (1.33) is also taken to be the definition of the charge radius in relativistic situations.

Returning to Eq. (1.30), we see that in the low Q^2 limit

$$\begin{aligned} \mathcal{M} &= \frac{e^2}{4} M m_e \bar{u} \left(\frac{dF_1(Q^2)}{dQ^2}\bigg|_{Q^2=0} - \frac{1}{4M^2} F_2(0) \right) \\ &= e^2 4 M m_e \frac{dG_E(Q^2)}{dQ^2}\bigg|_{Q^2=0}. \end{aligned} \tag{1.34}$$

The proton charge radius produces the shift

$$E_{2S} - E_{2p} = \frac{2\pi\alpha}{3} \left(|\phi_{2S}(0)|^2 - |\phi_{2P}(0)|^2 \right) R_E^2, \tag{1.35}$$

where $\phi(0)$ is the lepton wavefunction evaluated at the origin ($\phi_{2P}(0) = 0$). The radial wave functions for the $2S$ and $2P$ states are

$$\begin{aligned} R_{20} &= \frac{1}{(2a)^{3/2}}\left(2 - \frac{r}{a}\right)e^{-r/2a} \\ R_{21} &= \frac{1}{(2a)^{3/2}}\frac{r}{\sqrt{3}a}e^{-r/2a} \end{aligned} \tag{1.36}$$

where $a = 1/(m_r\alpha)$ is the Bohr radius and m_r is the reduced mass of the bound system.

The above energy shift is only a small contribution to the total Lamb Shift. The charge radius can only be extracted when the energy shifts of all Standard Model processes (vacuum polarization, two photon exchange, etc.) are calculated.

1.3.2 Atomic Measurements of the Proton Charge Radius

The CODATA value for the proton charge radius is $R_E = 0.8775(51)$ fm [5] and relies largely on Lamb Shift and other energy splitting measurements from electronic hydrogen.

Since muons are roughly 200 times heavier than electrons, muonic orbitals should be more sensitive to proton size effects. Recently, Pohl *et al.* [6] measured the Lamb Shift between the energy levels $2S_{1/2}^{F=1} - 2P_{3/2}^{F=2}$ of muonic hydrogen. They expected to find a more precise value of the proton charge radius that would still agree with previous electronic measurements. Instead, Pohl and collaborators extracted a charge radius of $R_E = 0.84184(67)$ fm. A more recent muon Lamb Shift analysis, including the energy level splitting $2S_{1/2}^{F=0} - 2P_{3/2}^{F=1}$ yielded a charge radius of $R_E = 0.84087(39)$ fm [7]. The muon measurements are 7σ smaller than the CODATA value.

Assuming the experimentalists truly obtained their stated accuracy and accounted for all Standard Model corrections, the smaller muon measurement is indicative of New Physics. The smaller muonic hydrogen measurements could be due to energy shifts from new muon-proton interactions being wrongly attributed to proton size effects. In order to bring the muonic measurement of the proton charge radius into agreement with the electronic measurement, New Physics must lower the muonic Lamb Shift by 310 μeV. Since this New Physics scenario involves muons, any models should also not conflict with the well-known muon anomalous magnetic moment discrepancy. In Chapter 5 we present our New Physics proposal that "explains" both the muon discrepancies. Concluding Remarks are made in Chapter 6.

CHAPTER 2

One Loop Contributions to the Proton's Weak Charge

The Standard Model Electroweak Lagrangian has a definite prediction for how the weak mixing angle, θ_W, should change at different momentum. The renormalization condition of the weak mixing angle is often chosen at the Z-pole because many measurements have been taken in this region [8]. This result in the modified minimal subtraction scheme is $\sin^2\theta_W(Q^2 = M_Z^2) = 0.2313$ [2]. Measurements of this parameter at momenta different than the Z-pole can be used to test for discrepancies between experiment and the prediction of the Standard Model. Such discrepancies would indicate the presence of hitherto unaccounted for New Physics.

The aim of the Qweak experiment at Jefferson Lab [3] is to obtain a 4% measurement of the proton's weak charge, Q_W^p. The experiment measured the asymmetry between left- and right-polarized scattered off an unpolarized proton target. The incoming electrons had an energy of $E = 1.165$ GeV and the momentum transfer was $Q^2 = -q^2 = 0.025$ GeV^2. Data analysis is ongoing at the time of this writing.

To extract the weak mixing angle from the measured value of Q_W^p and place constraints on New Physics at the desired precision, all radiative corrections must be well understood. This chapter identifies and evaluates all of the one loop diagrams contributing to Q_W^p, with the very notable exception of the bothersome $\Box_{\gamma Z}$. The $\Box_{\gamma Z}$ is discussed in Chap. 3.

2.1 Definition of Q_W^P at One Loop Order.

The parity-violating asymmetry for left- and right-handed electrons scattering off an unpolarized proton target is given by

$$A_{PV} \equiv \frac{\sigma_L - \sigma_R}{\sigma_L + \sigma_R} \tag{2.1}$$

where $\sigma_{L(R)}$ is the cross section for left (right) polarized electrons. Since σ is proportional to the modulus squared of the amplitude, the tree level (or lowest order) asymmetry can be rewritten as

$$A_{PV}|_{LO} = \frac{|\mathcal{M}_\gamma + \mathcal{M}_Z|^2_{\lambda=-1/2} - |\mathcal{M}_\gamma + \mathcal{M}_Z|^2_{\lambda=1/2}}{|\mathcal{M}_\gamma + \mathcal{M}_Z|^2_{\lambda=-1/2} + |\mathcal{M}_\gamma + \mathcal{M}_Z|^2_{\lambda=1/2}} \tag{2.2}$$

where $\mathcal{M}_\gamma$ and $\mathcal{M}_Z$ are the amplitudes for the exchange of a photon and Z boson and λ indicates the helicity of the incoming electron. The lowest order amplitudes, Fig. 2.1, are given by

$$i\mathcal{M}_\gamma = \bar{u}_{k',\lambda'}(ie\gamma^\mu)u_{k,\lambda}\frac{-ig_{\mu\nu}}{q^2 + i\epsilon}\bar{u}_{p',s'}(-ie\gamma^\nu)u_{p,s} \tag{2.3}$$

and

$$i\mathcal{M}_Z = \left(\frac{-ig}{2\cos^2\theta_W}\right)^2 \bar{u}_{k',\lambda'}\gamma^\mu(g_V^e - g_A^e\gamma^5)u_{k,\lambda}\frac{-ig_{\mu\nu}}{q^2 - M_Z^2 + i\epsilon}\bar{u}_{p',s'}\gamma^\nu(g_V^p - g_A^p\gamma^5)u_{p,s}. \tag{2.4}$$

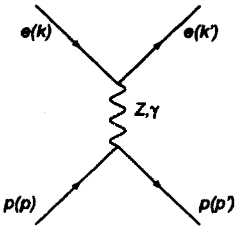

FIG. 2.1: Tree level diagram contributions to Q_W^p.

At low Q^2, the tree level asymmetry is

$$A_{PV}\Big|_{LO} = \frac{\mathcal{M}_Z|_{\lambda=-1/2} - \mathcal{M}_Z|_{\lambda=1/2}}{\mathcal{M}_\gamma} = \frac{G_F Q^2}{4\sqrt{2}\pi\alpha} Q_W^{p,LO}. \tag{2.5}$$

Here, $Q_W^{p,LO} = 2g_V^p = 1-4\sin^2\theta_W$ is the weak charge of the proton at tree level and G_F is the Fermi constant defined as $\sqrt{2}g^2/(8M_W^2)$. At tree level $\rho_{NC} \equiv M_W^2/(M_Z^2\cos^2\theta_W) = 1$.

To all order in perturbation theory, Eq. (2.1) can be rewritten as

$$A_{PV} = \frac{|\mathcal{M}_\gamma + \mathcal{M}_Z + \mathcal{M}_{RC}|^2_{\lambda=-1/2} - |\mathcal{M}_\gamma + \mathcal{M}_Z + \mathcal{M}_{RC}|^2_{\lambda=1/2}}{|\mathcal{M}_\gamma + \mathcal{M}_Z + \mathcal{M}_{RC}|^2_{\lambda=-1/2} + |\mathcal{M}_\gamma + \mathcal{M}_Z + \mathcal{M}_{RC}|^2_{\lambda=1/2}} \tag{2.6}$$

where $\mathcal{M}_{RC}$ are amplitudes for higher order radiative corrections.

Factoring out the tree level amplitudes, Eq. (2.6) becomes

$$A_{PV} = \frac{G_F Q^2}{4\sqrt{2}\pi\alpha} Q_W^{p,LO}\left(\rho_{NC} + \frac{\mathcal{M}_{RC}|_{\lambda=-1/2} - \mathcal{M}_{RC}|_{\lambda=1/2}}{\mathcal{M}_Z|_{\lambda=-1/2} - \mathcal{M}_Z|_{\lambda=1/2}}\right) \tag{2.7}$$

In the low Q^2, forward-scattering limit, the one loop asymmetry can be expressed as the expansion

$$A_{PV}\Big|_{1\text{ Loop}} = \frac{G_F Q^2}{4\sqrt{2}\pi\alpha}(Q_W^p + B_4 Q^2 + ...) \tag{2.8}$$

where B_4 contains hadronic corrections and

$$\begin{aligned} Q_W^p = Q_W^{p,LO}\Bigg(&\rho_{NC} + \frac{1}{\mathcal{M}_Z|_{\lambda=-1/2} - \mathcal{M}_Z|_{\lambda=1/2}} \\ &\times \left[(\mathcal{M}_V + \mathcal{M}_\Box + \mathcal{M}_{\gamma Z} + \mathcal{M}_{an}|_p + \mathcal{M}_p|_p)|_{\lambda=-1/2}\right. \\ &\left.- (\mathcal{M}_V + \mathcal{M}_\Box + \mathcal{M}_{\gamma Z} + \mathcal{M}_{an}|_p + \mathcal{M}_p|_p)|_{\lambda=1/2}\right]\Bigg)\Bigg|_{Q^2\to 0, E\to 0} . \end{aligned} \tag{2.9}$$

The only hadronic corrections included in the definition of Q_W^p is the "pinched" part of the proton's vertex correction ($\mathcal{M}_p|_p$). The pinch technique will be discussed in Sec. 2.6. The remaining radiative corrections to Q_W^p are gauge boson mass renormalizations (ρ_{NC}), electron vertex corrections ($\mathcal{M}_V$), box diagrams ($\mathcal{M}_\Box$), γZ propagator mixing ($\mathcal{M}_{mix}$), and the "pinched" part of the electron's anapole moment ($\mathcal{M}_{an}|_p$). The Feynman diagrams for ρ_{NC}, $\mathcal{M}_V$, and $\mathcal{M}_\Box$ are shown in Fig. 2.2. The diagrams for $\mathcal{M}_{\gamma Z}$, $\mathcal{M}_{an}$, and $\mathcal{M}_p$ are shown in Fig. 2.3 and contribute to the one loop running of $\sin^2\theta_W$.

Obviously, the Qweak experiment is not performed at $Q^2 = 0$ and incoming electron energy $E = 0$. Q_W^p can only be extracted when the Qweak data point is fitted with other low Q^2 parity-violating data from SAMPLE [9, 10], PVA4 [11, 12], HAPPEX [13, 14] and G0 [15] and extrapolated down to $Q^2 = 0$.

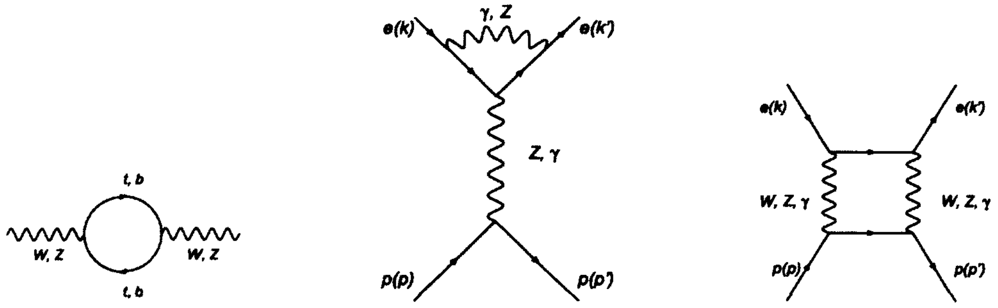

FIG. 2.2: One loop contributions to Q_W^p. The first diagram contributes to gauge boson mass renormalization (ρ_{NC}). The second diagram represents lepton vertex corrections ($\mathcal{M}_V$). The third diagram represents box diagrams ($\mathcal{M}_\Box$).

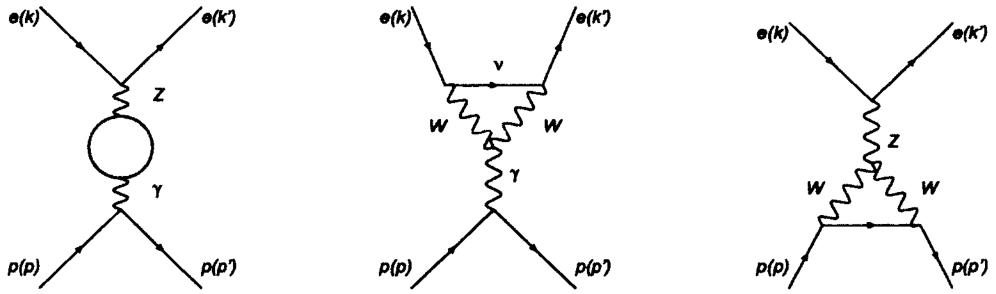

FIG. 2.3: Remaining one loop contributions to Q_W^p. The diagrams are for γZ propagator mixing ($\mathcal{M}_{\gamma Z}$), the electron's anapole moment ($\mathcal{M}_{an}$), and the proton's vertex correction ($\mathcal{M}_p$). The "pinched" parts of the latter two diagrams together with $\mathcal{M}_{mix}$ produce the running of $\sin^2\theta_W$ at one loop order.

The next sections will evaluate each type of one loop correction to Q_W^p. In the final section of this chapter we will connect the results of our calculations to the notation used in Eq. (4) of Erler *et al.* [16]

$$Q_W^p = [\rho_{NC} + \Delta_e][1 - 4\sin^2\theta_W(0) + \Delta_e'] + \Box_{WW} + \Box_{ZZ} + \Box_{\gamma Z}. \qquad (2.10)$$

In their notation, Δ_e and Δ_e' are terms containing corrections to the lepton vertex, $\sin^2\theta_W(0)$ is the one loop definition of the sine of the weak mixing angle evaluated at $Q^2 = 0$, and the $\Box$s are terms containing corrections to the exchange of two gauge bosons ("box" diagrams) indicated by the subscript.

For all of our calculations we use $\xi = 1$ gauge.

2.2 Evaluation of ρ_{NC}

At tree level $\rho_{NC} \equiv M_W^2/(M_Z^2\cos^2\theta_W) = 1$. At one loop order we must account for the corrections to the gauge boson propagators. The corrections renormalize the masses of the gauge boson and shift the value of ρ_{NC}. The one loop correction to the W propagator is

$$i\Pi_W^{\mu\nu}(q^2) = \left(\frac{-ig}{2\sqrt{2}}\right)^2 (-1) \int \frac{d^d\bar{q}}{(2\pi)^d} \frac{i}{(q+\bar{q})^2 - m_t^2} \frac{i}{\bar{q}^2 - m_b^2}$$
$$\times \operatorname{Tr}\left[\gamma^\mu (1-\gamma^5)((\not{q} + \not{\bar{q}}) + m_t)\gamma^\nu (1-\gamma^5)(\not{q} + m_b)\right] \tag{2.11}$$

where m_t and m_b are the masses of the top and bottom quarks. Other quark loops also exist, but their masses are negligible compared to those of the third generation. $\bar{q}$ is the momentum inside the loop and will be used throughout this chapter to indicate such.

Note that we are integrating over dimensions d in anticipation of using dimensional regularization to evaluate the divergent integral. Also note that the factors of $i\epsilon$ have been dropped in the denominator to clean up the notation. We can drop them as long as we remember that we are calculating propagators using the Feynman prescription.

The denominator of the above amplitude can be reexpressed using "Feynman's famous formula" (FFF),

$$\frac{1}{((q+\bar{q})^2 - m_t^2} \frac{1}{\bar{q}^2 - m_b^2} = \int_0^1 dx \frac{1}{\left(x(q+\bar{q})^2 - xm_t^2 + (1-x)(\bar{q}^2 - m_b^2)\right)^2}. \tag{2.12}$$

By redefining our momentum variable as $l = \bar{q} + xq$, the integrals for the quark loop become

$$\int \frac{d^d\bar{q}}{(2\pi)^d} \frac{1}{((q+\bar{q})^2 - m_t^2} \frac{1}{\bar{q}^2 - m_b^2} = \int_0^1 dx \int \frac{d^dl}{(2\pi)^d} \frac{1}{(l^2 - \Delta)^2} \tag{2.13}$$

where $\Delta = -x(1-x)q^2 + xm_t^2 + (1-x)m_b^2$.

After dropping terms proportional to odd powers of l, the trace simplifies to

$$\begin{aligned}
&\mathrm{Tr}\big[\gamma^\mu(1-\gamma^5)((\not{q}+\not{\bar{q}})+m_t)\gamma^\nu(1-\gamma^5)(\not{\bar{q}}+m_b)\big]\\
&\qquad = 8\bigg[-\left(1-\frac{2}{d}\right)l^2g^{\mu\nu}-2x(1-x)q^\mu q^\nu+x(1-x)q^2g^{\mu\nu}\bigg]
\end{aligned}\tag{2.14}$$

Performing the momentum integrals, the amplitude reduces to

$$\begin{aligned}
i\Pi_W^{\mu\nu}(q^2) = \left(\frac{-ig}{2\sqrt{2}}\right)^2\frac{8i}{(4\pi)^2}\int dx\big[-(xm_t^2+(1-x)m_b^2)g^{\mu\nu}\\
-2x(1-x)(q^\mu q^\nu-q^2g^{\mu\nu})\big]\left(\frac{2}{\epsilon}-\gamma+\log 4\pi-\log\Delta\right)
\end{aligned}\tag{2.15}$$

where $\epsilon = 4-d$ and γ is the Euler-Mascheroni constant. In the $\overline{MS}$ scheme, the divergent term, $\frac{2}{\epsilon}$, as well as γ and $\log 4\pi$ are subtracted off. A momentum-independent counterterm is also subtracted.

Since the weak charge is defined at $Q^2 = 0$, we are free to set $q^2 = -Q^2 = 0$. Subtracting off a generic counterterm $\log\Lambda^2$, the amplitude becomes

$$\begin{aligned}
i\Pi_W g^{\mu\nu} &= i\Pi_W^{\mu\nu}(0)\\
&= -\frac{ig^2}{32\pi^2}g^{\mu\nu}\bigg[-\frac{1}{2}(m_t^2+m_b^2)\\
&+\frac{m_t^4}{m_t^2-m_b^2}\log\frac{m_t^2}{\Lambda^2}-\frac{m_b^4}{m_t^2-m_b^2}\log\frac{m_b^2}{\Lambda^2}\bigg]
\end{aligned}\tag{2.16}$$

The amplitude for the one loop correction to the Z boson propagator is

$$\begin{aligned}
i\Pi_Z^{\mu\nu}(q^2) = \left(\frac{-ig}{2\cos^2\theta_W}\right)^2(-1)\sum_{i=b,t}\int\frac{d^d\bar{q}}{(2\pi)^d}\frac{i}{(q+\bar{q})^2-m_i^2}\frac{i}{\bar{q}^2-m_i^2}\\
\times\,\mathrm{Tr}\big[\gamma^\mu(1-\gamma^5)((\not{q}+\not{\bar{q}})+m_i)\gamma^\nu(1-\gamma^5)(\not{\bar{q}}+m_i)\big]
\end{aligned}\tag{2.17}$$

The breakdown of the denominators and momentum integral are nearly identical to that of Π_W. As for the previous amplitude, $l = \bar{q} + xq$. Here, $\Delta = -x(1-x)q^2 + m_i^2$.

Once again we take the $q^2 \to 0$ limit. The amplitude simplifies to

$$\begin{aligned} i\Pi_Z g^{\mu\nu} &= i\Pi_Z^{\mu\nu}(0) \\ &= -\frac{ig^2}{32\pi^2 \cos^2\theta_W} \sum_{i=b,t} m_i^2 \log\frac{m_i^2}{\Lambda^2} g^{\mu\nu} \end{aligned} \tag{2.18}$$

ρ is now renormalized to

$$\begin{aligned} \rho_{NC} &= \frac{M_W^2(1+\frac{\Pi_W}{M_W^2})}{M_Z^2\cos^2\theta_W(1+\frac{\Pi_Z}{M_Z^2})} \\ &= \frac{M_W^2}{M_Z^2\cos^2\theta_W}\left[1+\frac{g^2}{64\pi^2 M_W^2}\left(m_t^2+m_b^2-2\frac{m_t^2 m_b^2}{m_t^2-m_b^2}\log\frac{m_t^2}{m_b^2}\right)\right] \\ &= 1+\frac{G_F}{8\sqrt{2}\pi^2}\left(m_t^2+m_b^2-2\frac{m_t^2 m_b^2}{m_t^2-m_b^2}\log\frac{m_t^2}{m_b^2}\right) \\ &= 1+\Delta\rho \end{aligned} \tag{2.19}$$

The term on the left side represents "running" masses. All of the terms on the right side are all still tree level values. Thus, the substitutions $G_F = \sqrt{2}g^2/(8M_W^2)$ and $M_W^2/M_Z^2\cos^2\theta_W = 1$ are still valid.

Using $G_F = 1.1664 \times 10^{-5}$ GeV^2, $m_b = 4.198$ GeV, and, $m_t = 173.1$ GeV taken from the Particle Data Group [2], $\rho_{NC} = 1.0031$.

2.3 Evaluation of the Vertex Corrections: Δ_e and Δ'_e

There are two parity-violating lepton vertex diagrams. The first is a photon loop correction to Z boson exchange and the second is a Z boson loop correction to photon exchange.

2.3.1 Evaluation of Δ_e

The first diagram contributes to Δ_e and has the following amplitude

$$\begin{aligned} i\mathcal{M}_{Z,\gamma\text{-Loop}} = \left(\frac{-ig}{2\cos^2\theta_W}\right)^2 \bar{u}_{k,\lambda'}(ie\gamma^\tau) \int \frac{d^d\bar{q}}{(2\pi)^d} \frac{-ig_{\rho\tau}}{(k-\bar{q})^2} \frac{i(\not{\bar{q}}' + m)}{\bar{q}'^2 - m^2} \gamma^\mu (g_V^e - g_A^e\gamma^5) \\ \times \frac{i(\not{\bar{q}} + m)}{\bar{q}^2 - m^2}(ie\gamma^\rho) u_{k,\lambda} \frac{-ig_{\mu\nu}}{q^2 - M_Z^2} \bar{u}_{p,s'}\gamma^\nu (g_V^p - g_A^p\gamma^5) u_{p,s}, \end{aligned} \tag{2.20}$$

where m is the mass of the electron.

The denominator of the lepton current can be reexpressed using FFF,

$$\frac{1}{(k-\bar{q})^2}\frac{1}{(\bar{q}^2 - m^2)^2} = \int_0^1 dx \frac{2(1-x)}{\left((1-x)(\bar{q}^2 - m^2) + x(k-\bar{q})^2\right)^3}. \tag{2.21}$$

By redefining our momentum variable as $l = \bar{q} - xk$, the integrals for the lepton current become

$$\int \frac{d^d\bar{q}}{(2\pi)^d} \frac{1}{(k-\bar{q})^2} \frac{1}{(\bar{q}^2 - m^2)^2} = 2\int_0^1 dx(1-x) \int \frac{d^dl}{(2\pi)^d} \frac{1}{(l^2 - \Delta)^3} \tag{2.22}$$

where $\Delta = (1-x)^2 m^2$.

The numerator of the lepton current evaluates to

$$\begin{aligned} &\bar{u}_{k,\lambda'}(ie\gamma^\tau)(-ig_{\rho\tau}) i(\not{\bar{q}} + m)\gamma^\mu(g_V^e - g_A^e\gamma^5) i(\not{\bar{q}} + m)(ie\gamma^\rho) u_{k,\lambda} = \\ &\qquad (ie)^2 i\bar{u}_{k,\lambda'}\left[\left(\left(d - 4 + \frac{4}{d}\right) l^2 + 2m^2(x(4-x) - 1)\right)\gamma^\mu (g_V^e - g_A^e\gamma^5) \right. \\ &\qquad\qquad \left. - 4m^2(1-x)^2 g_A^e \gamma^\mu\gamma^5\right] u_{k,\lambda} \end{aligned} \tag{2.23}$$

where we have dropped terms proportional to odd l since they will integrate to zero.

In a renormalized gauge theory, there exist vertex counterterms that cancel loop contributions at one specific momentum. For vertex corrections, the renormatization condition is usually chosen at $Q = 0$. Such a counterterm cancels the contribution proportional to $(g_V^e - g_A^e\gamma^5)$. For momentum different than $Q = 0$, the counterterm will still cancel the divergent part but not the entire contribution. The vertex correction would cause the coupling to "run" when $Q \neq 0$.

As a check that the above algebra is correct, we can calculate the counterterm directly. The counterterm has the form of the derivative of the electron self-energy, $d\Sigma/d\not k|_{\not k=m}$. Specifically, the self-energy is an electron line with a photon loop,

$$-i\Sigma(\not k)|_{\gamma \text{ Loop}} = (ie)^2 \int \frac{d^d\bar{q}}{(2\pi)^d}\gamma^\alpha \frac{i(\not\bar{q} + m)}{(\bar{q}^2 - m^2)}\gamma^\beta \frac{-ig_{\alpha\beta}}{(k - \bar{q})^2}. \tag{2.24}$$

For an accurate calculation of the photon loop correction, the term proportional to $(g_V^e - g_A^e\gamma^5)$ should exactly cancel the derivative of the electron self-energy diagram, $d\Sigma/d\not k$. This cancelation has been verified.

The remaining amplitude at $Q = 0$ is

$$\begin{aligned} i\mathcal{M}_{Z,\gamma\text{-Loop}} =& \left(\frac{-ig}{2\cos^2\theta_W}\right)^2 \bar{u}_{k,\lambda'}(-g_A^e\gamma^\mu\gamma^5)u_{k,\lambda} \\ &\times \frac{-ig_{\mu\nu}}{-M_Z^2}\bar{u}_{p,s'}\gamma^\nu(g_V^p - g_A^p\gamma^5)u_{p,s} \\ &\times 8im^2(ie)^2\int_0^1 dx(1-x)^3 \int \frac{d^dl}{(2\pi)^d}\frac{1}{(l^2-\Delta)^3}. \end{aligned} \tag{2.25}$$

The remaining integral is actually convergent at $d = 4$ and evaluates to

$$\int_0^1 dx(1-x)^3 \int \frac{d^4l}{(2\pi)^4}\frac{1}{(l^2-\Delta)^3} = \frac{-i}{(4\pi)^2 4m^2}. \tag{2.26}$$

The ratio between this vertex correction and Z exchange amplitudes is Δ_e,

$$\begin{aligned}\Delta_e &= \frac{\mathcal{M}_{Z,\gamma\text{-Loop}}|_{\lambda=-1/2} - \mathcal{M}_{Z,\gamma\text{-Loop}}|_{\lambda=1/2}}{\mathcal{M}_Z|_{\lambda=-1/2} - \mathcal{M}_Z|_{\lambda=1/2}} \\ &= -\frac{\alpha}{2\pi} \end{aligned} \tag{2.27}$$

Using the value of α at $Q = 0$, this term evaluates to -0.00116.

2.3.2 Evaluation of Δ_e'

The amplitude for a Z boson loop correction to photon exchange contributes to Δ_e' is

$$\begin{aligned} i\mathcal{M}_{\gamma,Z\text{-Loop}} = \left(\frac{-ig}{2\cos^2\theta_W}\right)^2 \bar{u}_{k',\lambda'} \int \frac{d^d\bar{q}}{(2\pi)^d} \frac{-ig_{\sigma\tau}}{(k-\bar{q})^2 - M_Z^2} \gamma^\tau (g_V^e - g_A^e\gamma^5) \frac{i(\bar{q}\!\!/' + m)}{\bar{q}'^2 - m^2} \\ \times (ie\gamma^\mu) \frac{i(\bar{q}\!\!/ + m)}{\bar{q}^2 - m^2} \gamma^\sigma (g_V^e - g_A^e\gamma^5) u_{k,\lambda} \frac{-ig_{\mu\nu}}{q^2} \bar{u}_{p',s'}(-ie\gamma^\nu) u_{p,s}. \end{aligned} \tag{2.28}$$

Unlike the amplitude for the γ-loop correction to Z boson exchange, we cannot immediately take the $Q \to 0$ limit. The reason is that the photon propagator diverges as $Q \to 0$ wheras the Z boson propagator does not. We must keep terms in the lepton current proportional to q^2 to produce a cancelation with the denominator of the photon propagator. By redefining our momentum variable as $l = \bar{q} - x_1 k - x_2 q$ as before, the integrals for the lepton current become

$$\begin{aligned} \int \frac{d^d\bar{q}}{(2\pi)^d} \frac{1}{((k-\bar{q})^2 - M_Z^2)} \frac{1}{(\bar{q}'^2 - m^2)} \frac{1}{(\bar{q}^2 - m^2)} \\ = 2\int_0^1 dx_1 \int_0^{1-x_1} dx_2 \int \frac{d^dl}{(2\pi)^d} \frac{1}{(l^2 - \Delta)^3} \end{aligned} \tag{2.29}$$

where $\Delta = (1-x_1)^2 m^2 + x_1 M_Z^2 - x_2(1 - x_1 - x_2)q^2$.

The numerator of the lepton current evaluates to

$$
\begin{aligned}
\bar{u}_{k',\lambda'}(-ig_{\sigma\tau})\gamma^{\tau}(g_V^e - g_A^e\gamma^5)i(\not{q}' + m)(ie\gamma^{\mu})i(\not{q} + m)\gamma^{\sigma}(g_V^e - g_A^e\gamma^5)u_{k,\lambda} &= \\
i(ie)\bar{u}_{k',\lambda'}\Big\{(g_V^e)^2\big[-(2-d)(1-2/d)l^2\gamma^{\mu} \\
-2m^2(3-2x_1-x_1^2)\gamma^{\mu} + 2q^2(x_2-1)(x_1+x_2)\gamma^{\mu} \\
+4mk'^{\mu}((x_2-1)x_1-2x_2) + 4mk^{\mu}(1+2x_1+2x_2-x_1(x_1+x_2))\big] \\
+(g_A^e)^2\big[-(2-d)(1-2/d)l^2\gamma^{\mu} \\
-2m^2(-1-2x_1-x_1^2)\gamma^{\mu} + 2q^2(x_2-1)(x_1+x_2)\gamma^{\mu} \\
+4mk'^{\mu}((x_2-1)x_1+2x_2) - 4mk^{\mu}(1+2x_1+2x_2+x_1(x_1+x_2))\big] \\
+(-2g_A^e g_V^e)\big[-(2-d)(1-2/d)l^2\gamma^{\mu} \\
-2m^2(1-x_1^2)\gamma^{\mu} + 2q^2(x_2-1)(x_1+x_2)\gamma^{\mu} \\
-4mk'^{\mu}(x_2-1)(x_1+2x_2) + 4mk^{\mu}(x_1+x_2)(x_1+2x_2-2)\big]\gamma^5\Big\}u_{k,\lambda} \quad (2.30)
\end{aligned}
$$

The vector part of the numerator is not necessary for calculating a parity-violating asymmetry. It is included for completeness and as a check that the algebra is correct. In the limit $Q \to 0$ the vector part cancels with the counterterm given by the derivative of the electron self-energy diagram. This self-energy diagram is different than the previous one in that the electron line emits and reabsorbs a Z boson. Its amplitude is

$$
\begin{aligned}
-i\Sigma(\not{k})|_{\text{Z Loop}} = \left(\frac{-iq}{2\cos\theta_W}\right)^2 \int \frac{d^d\bar{q}}{(2\pi)^d}\gamma^{\alpha}(g_V^e - g_A^e\gamma^5)\frac{-ig_{\alpha\beta}}{(k-\bar{q})^2 - M_Z^2}\frac{i(\not{\bar{q}}+m)}{(\bar{q}^2-m^2)} \\
\times \gamma^{\beta}(g_V^e - g_A^e\gamma^5). \quad (2.31)
\end{aligned}
$$

Upon subtracting off the axial part of $d\Sigma/d\not{k}|_{\not{k}=m}$ and performing the l integral, the axial part of the loop correction is

$$\begin{aligned} i\mathcal{M}_{\gamma,Z\text{-Loop}}\Big|_{\text{Axial}} = &\left(\frac{-ig}{2\cos^2\theta_W}\right)^2 \frac{-\alpha}{2\pi}\bar{u}_{k',\lambda'} \int_0^1 dx_1 \int_0^{1-x_1} dx_2 \\ &\times \left[\log\left[\frac{x_1 M_Z^2 + (1-x_1)^2 m^2}{\Delta}\right]\gamma^\mu \right. \\ &- m^2(x_1^2 - 1)\left(\frac{1}{\Delta} - \frac{1}{x_1 M_Z^2 + (1-x_1)^2 m^2}\right)\gamma^\mu \\ &- \frac{q^2}{\Delta}(x_2 - 1)(x_1 + x_2)\gamma^\mu + \frac{2m}{\Delta}k'^\mu(x_2 - 1)(x_1 + 2x_2) \\ &\left. - \frac{2m}{\Delta}k^\mu(x_1 + x_2)(x_1 + 2x_2 - 2)\right](-2g_A^e g_V^e \gamma^5)u_{k,\lambda} \\ &\times \frac{-i}{q^2}\bar{u}_{p',s'}\gamma_\mu u_{p,s}. \end{aligned} \tag{2.32}$$

When we rewrite k^μ and k'^μ in terms of q^μ and $(k + k')^\mu$, we see that the coefficient for $(k + k')^\mu$ integrates to zero. q^μ when shifted to the hadron side also yields zero.

Eq. (2.32) is complicated, but simplifies after it is expanded in terms of q^2. When the limit $q^2 \to 0$ is taken, only the term proportional to q^2 survives as it cancels with the denominator of the photon propagator.

The parity-violating ratio between this vertex correction and the treel level Z boson exchange in the $Q \to 0$ limit is

$$\begin{aligned} \frac{\Delta'_e}{Q_W^{p,LO}} &= \frac{\mathcal{M}_{\gamma,Z-Loop}|_{\lambda=-1/2} - \mathcal{M}_{\gamma,Z-Loop}|_{\lambda=1/2}}{\mathcal{M}_Z|_{\lambda=-1/2} - \mathcal{M}_Z|_{\lambda=1/2}} \\ &= -\frac{\alpha}{3\pi}\left(\frac{1}{6} + \log\left[\frac{M_Z^2}{m^2}\right]\right) \end{aligned} \tag{2.33}$$

At $Q = 0$, this term evaluates to -0.00141.

2.4 Box Diagrams: $\Box_{WW}$ and $\Box_{ZZ}$

The box diagrams describe the exchange of two gauge bosons between the electron and proton. The W and Z propagators are dominated by high momentum which allows the hadronic currents to be calculated using pQCD. The WW and ZZ boxes can therefore be calculated directly with quark operators substituted into the hadronic currents. In contrast, the photon propagator is dominated by low momentum exchange outside of the regime of pQCD. The analysis of the γZ box is more involved than the other boxes and we delay a presentation of its analysis until the next chapter.

The calculation of the WW and ZZ boxes is relatively straightforward. Still, we present some of the intermediate results in the evaluation of the boxes highlight their structure and to provide a check for readers interested in working through the calculations themselves.

2.4.1 Evaluation of $\Box_{WW}$

The easiest way to proceed in the analysis of the WW box is to express its amplitude in terms of field operators,

$$\begin{aligned} i\mathcal{M}_{WW}(2\pi)^4\delta(k'+p'-k-p) = {} & \left(\frac{-ig}{\sqrt{2}}\right)^4 \int dwdxdydz \\ & \times \big\langle e(k')p(p')\big|T\{W^-_\mu(w)J^{-\mu}(w)W^+_\nu(x)J^{+\nu}(x) \\ & \times W^-_\alpha(y)J^{-\alpha}(y)W^+_\beta(z)J^{+\beta}(z)\}\big|e(k)p(p)\big\rangle, \end{aligned} \tag{2.34}$$

where $J^{+\nu}(x) = \bar{\psi}_\nu(x)\gamma^\nu 1/2(1-\gamma^5)\psi_e(x)$ and the integrals are taken over four dimensions. Evaluating the gauge field propagators and simpifying gives

$$\begin{aligned} i\mathcal{M}_{WW}(2\pi)^4\delta(k'+p'-k-p) = \left(\frac{-ig}{\sqrt{2}}\right)^4 \int dw dx \langle e(k') \big| T\{J^{-\mu}(w)J^{+\nu}(x)\} \big| e(k)\rangle \\ \times \int dydz \int \frac{d^4\bar{k}}{(2\pi)^4}\frac{-ig_{\mu\beta}}{\bar{k}^2 - M_W^2}e^{-i\bar{k}(z-w)} \int \frac{d^4\bar{k}'}{(2\pi)^4}\frac{-ig_{\nu\alpha}}{\bar{k}'^2 - M_W^2}e^{-i\bar{k}'(x-y)} \\ \times \langle p(p') \big| T\{J^{-\alpha}(y)J^{+\beta}(z)\} \big| p(p)\rangle, \end{aligned} \tag{2.35}$$

We are only interested in the zero-momentum transfer limit, $\bar{k} = \bar{k}' = q$. After evaluating some of the δ-functions, the amplitude becomes

$$\begin{aligned} i\mathcal{M}_{WW} = \left(\frac{-ig}{2\sqrt{2}}\right)^4 (-2i) \int \frac{d^4q}{(2\pi)^4}\frac{1}{q^2(q^2-M_W^2)^2}\bar{u}_{k',\lambda'}\gamma^\mu \not{q}\gamma^\nu(1-\gamma^5)u_{k,\lambda} \\ \times 4 \int d^4y e^{iqy}\langle p(p') \big| T\{J_\mu^+(0)J_\nu^-(y)\} \big| p(p)\rangle. \end{aligned} \tag{2.36}$$

The lepton current simplifies to

$$\bar{u}_{k,\lambda'}\gamma^\mu \not{q}\gamma^\nu(1-\gamma^5)u_{k,\lambda} = q_\alpha k_\beta \mathrm{Tr}\big[\frac{1}{2}(1+(2\lambda)\gamma^5)\gamma^\beta\gamma^\mu\gamma^\alpha\gamma^\nu(1-\gamma^5)\big], \tag{2.37}$$

where λ indicates the helicity of the incoming electron. Only left-handed electrons ($\lambda = -1/2$) give a non-vanishing trace:

$$\bar{u}_{k,\lambda'}\gamma^\mu \not{q}\gamma^\nu(1-\gamma^5)u_{k,\lambda}\big|_{\lambda=-1/2} = 4(k^\mu q^\nu + k^\nu q^\mu - q\cdot k g^{\mu\nu} + i\epsilon^{\beta\mu\alpha\nu}k_\beta q_\alpha) \tag{2.38}$$

For the hadron currents we only consider field operators for the up and down quarks, notated $u(x)$ and $d(x)$ respectively.

$$\begin{aligned}4\int d^4y e^{iqy}\langle p(p')|T\{J_\mu^+(0)J_\nu^-(y)\}|p(p)\rangle = \int d^4y e^{iqy}\langle p(p')|\{&\bar{u}(0)\gamma_\mu(1-\gamma^5)d(0)\\ &\times \bar{d}(y)\gamma_\nu(1-\gamma^5)u(y)\Theta(0-y_0)\\ &+\bar{d}(y)\gamma_\nu(1-\gamma^5)u(y)\\ &\times \bar{u}(0)\gamma_\mu(1-\gamma^5)d(0)\Theta(y_0-0)\}|p(p)\rangle \qquad (2.39)\end{aligned}$$

After some algebra and the approximations $u(y) \approx u(0)$ and $d(y) \approx d(0)$, the currents reduce to

$$\begin{aligned}4\int d^4y e^{iqy}\langle p(p')|T\{J_\mu^+(0)J_\nu^-(y)\}|p(p)\rangle = -\frac{2iq^\sigma}{q^2}\langle p(p')|\{&\bar{u}(0)\gamma_\mu\gamma_\sigma\gamma_\nu(1-\gamma^5)u(0)\\ &-\bar{d}(0)\gamma_\nu\gamma_\sigma\gamma_\mu(1-\gamma^5)d(0)\}|p(p)\rangle \qquad (2.40)\end{aligned}$$

The entire amplitude can be expressed as

$$\begin{aligned}i\mathcal{M}_{WW}\big|_{\lambda=-1/2} = \left(\frac{-ig}{2\sqrt{2}}\right)^4(-2i)^2 4\int &\frac{d^4q}{(2\pi)^4}\frac{1}{q^2(q^2-M_W^2)^2}\\ &\times(k^\mu q^\nu + k^\nu q^\mu - q\cdot k g^{\mu\nu} + i\epsilon^{\beta\mu\alpha\nu}k_\beta q_\alpha)\\ &\times\frac{q^\sigma}{q^2}\langle p(p')|\{\bar{u}(0)\gamma_\mu\gamma_\sigma\gamma_\nu(1-\gamma^5)u(0)\\ &-\bar{d}(0)\gamma_\nu\gamma_\sigma\gamma_\mu(1-\gamma^5)d(0)\}|p(p)\rangle. \qquad (2.41)\end{aligned}$$

To evaluate the first three terms of the lepton current with the hadron current, we must spin-average the hadron currents and rewrite the quark currents in terms of isospin and electromagnetic currents. In the limit of zero momentum transfer, $p' = p$ and the currents simplify to

$$\begin{aligned}\langle p(p')|J^3_\mu|p(p)\rangle &= \frac{1}{2}\langle p(p')|\{\bar{u}(0)\gamma_\mu u(0) - \bar{d}(0)\gamma_\mu d(0)\}|p(p)\rangle \\ &= p_\mu \end{aligned} \tag{2.42}$$

and

$$\begin{aligned}\langle p(p')|J^{em}_\mu|p(p)\rangle &= \langle p(p')|\left\{\frac{2}{3}\bar{u}(0)\gamma_\mu u(0) - \frac{1}{3}\bar{d}(0)\gamma_\mu d(0)\right\}|p(p)\rangle \\ &= 2p_\mu. \end{aligned} \tag{2.43}$$

To evaluate the fourth term of the lepton current with the hadron current, we must invoke the identity,

$$\gamma^\mu\gamma^\alpha\gamma^\nu = g^{\mu\nu}\gamma^\nu - g^{\mu\nu}\gamma^\alpha + g^{\alpha\nu}\gamma^\mu + i\epsilon^{\mu\alpha\nu\sigma}\gamma_\sigma\gamma^5. \tag{2.44}$$

It is important not to spin-average before taking this identity as it contains a γ^5 term.

The amplitude simplifies to

$$i\mathcal{M}_{WW}\big|_{\lambda=-1/2} = i\frac{g^4}{2}\frac{p\cdot k}{16\pi^2 M_W^2}(1+1+1/2+9/2). \tag{2.45}$$

In the $Q^2 \to 0$ limit, the amplitude for Z boson exchange is

$$i\mathcal{M}_Z = -i\frac{g^2}{2\cos^2\theta_W M_Z^2}k\cdot p(g_V^e - (2\lambda)g_A^e)Q_W^{p,LO} \tag{2.46}$$

and the WW box is

$$
\begin{aligned}
\Box_{WW} &= \frac{\mathcal{M}_{WW}|_{\lambda=-1/2} - \mathcal{M}_{WW}|_{\lambda=1/2}}{\mathcal{M}_{Z}|_{\lambda=-1/2} - \mathcal{M}_{Z}|_{\lambda=1/2}} Q_W^{p,LO} \\
&= \frac{7\alpha}{4\pi \sin^2\theta_W}
\end{aligned}
\tag{2.47}
$$

Although the overall momentum transfer is $Q = 0$, the momentum within the loop is high. To evaluate this term, definitions of α and $\sin^2\theta_W$ at the Z pole are used. At the Z pole $\Box_{WW}$ evaluates to 0.0188.

2.4.2 Evaluation of $\Box_{ZZ}$

The ZZ box analysis is very similar to that of the WW box. Substituting $J^{\pm\mu} \to J_Z^\mu$, $W^{\pm\mu} \to Z^\mu$, and $\frac{-ig}{\sqrt{2}} \to \frac{-ig}{\cos^2\theta_W}$ in Eq. (2.35), the ZZ amplitude is

$$
\begin{aligned}
i\mathcal{M}_{ZZ}(2\pi)^4\delta(k'+p'-k-p) &= \left(\frac{-ig}{\cos^2\theta_W}\right)^4 \int dwdx \big\langle e(k')\big|T\{J_Z^\mu(w)J_Z^\nu(x)\}\big|e(k)\big\rangle \\
&\times \int dydz \int \frac{d^4\bar{k}}{(2\pi)^4}\frac{-ig_{\mu\beta}}{\bar{k}^2 - M_Z^2} e^{-i\bar{k}(z-w)} \int \frac{d^4\bar{k}'}{(2\pi)^4}\frac{-ig_{\nu\alpha}}{\bar{k}'^2 - M_Z^2} e^{-i\bar{k}'(x-y)} \\
&\times \big\langle p(p')\big|T\{J_Z^\alpha(y)J_Z^\beta(z)\}\big|p(p)\big\rangle,
\end{aligned}
\tag{2.48}
$$

where $J_Z^\nu(x) = \bar{\psi}_e(x)\gamma^\nu 1/2(g_V^e - g_A^e\gamma^5)\psi_e(x)$. Once again we are only interested in the zero-momentum transfer limit, $\bar{k} = \bar{k}' = q$. After evaluating some of the δ-functions, the amplitude becomes

$$
\begin{aligned}
i\mathcal{M}_{ZZ}(2\pi)^4\delta(k'+p'-k-p) &= \left(\frac{-ig}{2\cos^2\theta_W}\right)^4 (-i) \int \frac{d^4q}{(2\pi)^4}\frac{1}{q^2(q^2-M_Z^2)^2} \\
&\times \bar{u}_{k',\lambda'}\gamma^\mu \not{q}\gamma^\nu((g_V^e)^2 + (g_A^e)^2 - 2g_V^e g_A^e\gamma^5)u_{k,\lambda} \\
&\times 4\int d^4y e^{iqy}\big\langle p(p')\big|T\{J_{Z\mu}(0)J_{Z\nu}(y)\}\big|p(p)\big\rangle.
\end{aligned}
\tag{2.49}
$$

The lepton current simplifies to

$$\bar{u}_{k,\lambda'}\gamma^{\mu}\ \not{q}\gamma^{\nu}((g_V^e)^2+(g_A^e)^2-2g_V^e g_A^e\gamma^5)u_{k,\lambda} = q_\alpha k_\beta \mathrm{Tr}\big[\frac{1}{2}(1+(2\lambda)\gamma^5)\gamma^\beta\gamma^\mu\gamma^\alpha\gamma^\nu \\ \times((g_V^e)^2+(g_A^e)^2-2g_V^e g_A^e\gamma^5)\big], \qquad (2.50)$$

where λ indicates the helicity of the incoming electron. Both left- and right-handed electrons give a non-vanishing trace:

$$\bar{u}_{k,\lambda'}\gamma^{\mu}\ \not{q}\gamma^{\nu}((g_V^e)^2+(g_A^e)^2-2g_V^e g_A^e\gamma^5)u_{k,\lambda}\big|_{\lambda=\pm 1/2} = 2((g_V^e \mp g_A^e)^2(k^\mu q^\nu + k^\nu q^\mu \\ - q\cdot k g^{\mu\nu} \mp i\epsilon^{\beta\mu\alpha\nu}k_\beta q_\alpha) \qquad (2.51)$$

For the hadron currents we once again only consider field operators for the up and down quarks, notated $u(x)$ and $d(x)$ respectively.

$$4\int d^4y e^{iqy}\langle p(p')|T\{J_{Z\mu}(0)J_{Z\nu}(y)\}|p(p)\rangle = \int d^4y e^{iqy}\langle p(p')| \\ \sum_{q=u,d}\{\bar{q}(0)\gamma_\mu(g_V^q - g_A^q\gamma^5)q(0) \\ \times \bar{q}(y)\gamma_\nu(g_V^q - g_A^q\gamma^5)q(y)\Theta(0-y_0) \\ + \bar{q}(y)\gamma_\nu(g_V^q - g_A^q\gamma^5)q(y) \\ \times \bar{q}(0)\gamma_\mu(g_V^q - g_A^q\gamma^5)q(0)\Theta(y_0-0)\}|p(p)\rangle \\ (2.52)$$

After some algebra and the approximations $u(y) \approx u(0)$ and $d(y) \approx d(0)$, the currents reduce to

$$\begin{aligned} 4\int d^4y e^{iqy}\langle p(p')|T\{J_{Z\mu}(0)J_{Z\nu}(y)\}|p(p)\rangle = -\frac{iq^\sigma}{q^2}\langle p(p')| &\sum_{q=u,d}\{\bar{q}(0)\gamma_\mu\gamma_\sigma\gamma_\nu \\ &\times((g_V^e)^2+(g_A^e)^2-2g_V^e g_A^e\gamma^5)q(0) \\ &-\bar{q}(0)\gamma_\nu\gamma_\sigma\gamma_\mu \\ &\times((g_V^e)^2+(g_A^e)^2-2g_V^e g_A^e\gamma^5)q(0)\}|p(p)\rangle \end{aligned} \tag{2.53}$$

The entire amplitude can be expressed as

$$\begin{aligned} i\mathcal{M}_{ZZ}\big|_{\lambda=-1/2} - i\mathcal{M}_{ZZ}\big|_{\lambda=1/2} = \left(\frac{-ig}{2\cos^2\theta_W}\right)^4 &(-2i)(-i)\int\frac{d^4q}{(2\pi)^4}\frac{1}{q^2(q^2-M_Z^2)^2} \\ &\times\left[((g_V^e+g_A^e)^2-(g_V^e-g_A^e)^2)(k^\mu q^\nu+k^\nu q^\mu-q\cdot k g^{\mu\nu})\right. \\ &\left.+i\epsilon^{\beta\mu\alpha\nu}k_\beta q_\alpha)((g_V^e+g_A^e)^2+(g_V^e-g_A^e)^2)\right] \\ &\times\frac{q^\sigma}{q^2}\langle p(p')|\sum_{q=u,d}\{\bar{q}(0)\gamma_\mu\gamma_\sigma\gamma_\nu \\ &\times((g_V^e)^2+(g_A^e)^2-2g_V^e g_A^e\gamma^5)q(0) \\ &-\bar{q}(0)\gamma_\nu\gamma_\sigma\gamma_\mu \\ &\times((g_V^e)^2+(g_A^e)^2-2g_V^e g_A^e\gamma^5)q(0)\}|p(p)\rangle \end{aligned} \tag{2.54}$$

The first three terms of the lepton current cancel with the hadron current in a straightforward manner. To evaluate the fourth term we once again must invoke the identity of

Eq. (2.44). After spin-averaging this term becomes

$$
\begin{aligned}
i\epsilon^{\beta\mu\alpha\nu}k_\beta q_\alpha \times \frac{q^\sigma}{q^2}\langle\ldots\rangle &= 6 < p(p')\big|\sum_{q=u,d} g_V^q g_A^q q(0)\gamma_\beta q(0)\big|p(p)\big\rangle \\
&= 6k^\beta((g_V^e + g_A^e)^2 + (g_V^e - g_A^e)^2) \\
&\times < p(p')\big|\Big(\frac{3}{2} - 3\sin^2\theta_W\Big)J_\beta^{em} + \Big(-\frac{3}{2} + \frac{8}{3}\sin^2\theta_W\Big)J_\beta^3\big|p(p)\big\rangle.
\end{aligned}
\tag{2.55}
$$

The amplitude simplifies to

$$
\begin{aligned}
i\mathcal{M}_{ZZ}\big|_{\lambda=-1/2} - i\mathcal{M}_{ZZ}\big|_{\lambda=1/2} &= i\Big(\frac{-ig}{2\cos^2\theta_W}\Big)^4 \frac{24p\cdot k}{16\pi^2 M_Z^2}\Big(\frac{3}{4} - \frac{5}{3}\sin^2\theta_W\Big) \\
&\times (1 - 4\sin^2\theta_W + 8\sin^4\theta_W)
\end{aligned}
\tag{2.56}
$$

The ZZ box is

$$
\begin{aligned}
\Box_{ZZ} &= \frac{\mathcal{M}_{ZZ}|_{\lambda=-1/2} - \mathcal{M}_{ZZ}|_{\lambda=1/2}}{\mathcal{M}_Z|_{\lambda=-1/2} - \mathcal{M}_Z|_{\lambda=1/2}} Q_W^{p,LO} \\
&= \frac{\alpha}{4\pi\sin^2\theta_W\cos^2\theta_W}\Big(\frac{9}{4} - 5\sin^2\theta_W\Big)(1 - 4\sin^2\theta_W + 8\sin^4\theta_W)
\end{aligned}
\tag{2.57}
$$

As with the other box diagram, we evaluate $\Box_{ZZ}$ using Z pole definitions of parameters. $\Box_{ZZ}$ evaluates to 0.00192.

2.5 Contribution of $\mathcal{M}_{mix}$ to $\sin^2\theta_W(Q^2)$

A Z boson propagator can fluctuate into a photon propagator through a fermion or W boson loop. Such diagrams, $\mathcal{M}_{mix}$, contribute to the running of $\sin^2\theta_W$.

All amplitudes have the form

$$i\mathcal{M}_{mix} = \frac{-ig}{2\cos^2\theta_W}\bar{u}_{k',\lambda'}\gamma_\mu(g_V^e - g_A^e\gamma^5)u_{k,\lambda}\frac{-ig^{\alpha\mu}}{q^2 - M_Z^2}\{i\Pi_{\alpha\beta}\}$$
$$\times \frac{-ig^{\beta\nu}}{q^2}\bar{u}_{p',s'}(-ie\gamma^\nu)u_{p,s} \tag{2.58}$$

Notice that we have dropped the $q_\alpha q_\mu$ term in the numerator of the Z boson propagator since it will evaluate to zero when confronted with the hadron current.

All of the loops with fermions or two W bosons feature the same substitution $l = \bar{q}+xq$. The integrals for these loops become

$$\int \frac{d^d\bar{q}}{(2\pi)^d}\frac{1}{\bar{q}^2 - m_i^2}\frac{1}{(\bar{q}+q)^2 - m_i^2} = \int_0^1 dx \int \frac{d^dl}{(2\pi)^d}\frac{1}{(l^2-\Delta)^2}, \tag{2.59}$$

where $\Delta = -x(1-x)q^2 + m_i^2$ and m_i is the mass of either a fermion or W boson.

2.5.1 Contribution of the fermion loop.

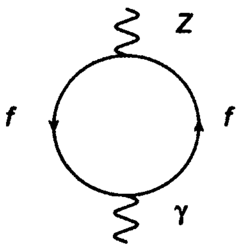

FIG. 2.4: Fermion loop.

The fermion loop is shown in Fig. 2.4 and its amplitude is

$$\begin{aligned} i\Pi_{\alpha\beta,\ \text{Fermion Loop}} = (-1) \int \frac{d^d\bar{q}}{(2\pi)^d} \sum_i \sum_{\text{color}} \text{Tr}\Big[(-iQ_i e\gamma_\beta) \frac{i(\bar{\not{q}} + \not{q} + m_i)}{(\bar{q}+q)^2 - m_i^2} \\ \times \frac{-ig}{2\cos^2\theta_W} \gamma_\alpha (g_V^i - g_A^i \gamma^5) \frac{i(\bar{\not{q}} + m_i)}{\bar{q}^2 - m_i^2} \Big], \end{aligned} \tag{2.60}$$

where Σ_i is a sum over fermions. The sum over color only applies to the quark loops. Plugging Eq. (2.60) into Eq. (2.58) gives

$$\begin{aligned} i\mathcal{M}_{mix,\ \text{Fermion Loop}} = \left(\frac{-ig}{2\cos^2\theta_W}\right)^2 \bar{u}_{k',\lambda'}\gamma^\mu (g_V^e - g_A^e\gamma^5) u_{k,\lambda} \frac{-ig_{\mu\nu}}{q^2 - M_Z^2} \bar{u}_{p',s'}(\gamma^\nu) u_{p,s} \\ \times \frac{2\alpha}{\pi} \sum_i \sum_{\text{color}} (-Q_i) g_V^i \int_0^1 dx (1-x)x \left(\frac{2}{\epsilon} - \gamma + \log 4\pi - \log\Delta\right), \end{aligned} \tag{2.61}$$

Using the $\overline{MS}$ scheme, the divergent parts as well as γ and $\log 4\pi$ are subtracted off.

We are free to choose a renormalization condition. Because the Particle Data Group [2] quotes a value of $\sin^2\theta_W$ at the Z pole, we renormalize at the mass of the Z boson. To invoke our renormalization condition $\sin^2\theta_W(Q^2 = M_Z^2) = 0.2313$, we subtract off $\Delta = x(1-x)M_Z^2 + m_i^2$. For the remainder of this chapter, $\sin^2\theta_W = 0.2313$.

Notice that the first line of Eq. (2.61) is very similar to Eq. (2.4). Adding the hadronic vector part of these two equations together gives

$$\begin{aligned} & i\mathcal{M}_Z + i\mathcal{M}_{mix,\ \text{Fermion Loop}} \\ & = \left(\frac{-ig}{2\cos^2\theta_W}\right)^2 \bar{u}_{k',\lambda'}\gamma^\mu (g_V^e - g_A^e\gamma^5) u_{k,\lambda} \frac{-ig_{\mu\nu}}{q^2 - M_Z^2} \bar{u}_{p',s'}(\gamma^\nu) u_{p,s} \\ & \times \left(g_V^p - \frac{2\alpha}{\pi} \sum_i \sum_{\text{color}} Q_i g_V^i \int_0^1 dx (1-x)x \log\left[\frac{m_i^2 + x(1-x)M_Z^2}{m_i^2 + x(1-x)Q^2}\right]\right). \end{aligned} \tag{2.62}$$

Following the notation of Czarnecki and Marciano [17, 18, 19], the second line of

Eq. (2.62) can be interpreted as the fermion loop's contribution to the "running" of $\sin^2\theta_W$,

$$\frac{1}{2}(1 - 4\sin^2\theta_W(Q^2)|_{\text{fermion loop}}) = \frac{1}{2}(1 - 4\kappa_f(Q^2)\sin^2\theta_W(M_Z^2)) \tag{2.63}$$

where

$$\begin{aligned}\kappa_f(Q^2) &= 1 + \frac{\alpha}{\pi\sin^2\theta_W}\sum_i\sum_{\text{color}} Q_i g_V^i \int_0^1 dx(1-x)x\log\left[\frac{m_i^2 + x(1-x)M_Z^2}{m_i^2 + x(1-x)Q^2}\right] \\ &= 1 + \kappa_{lep}(Q^2) + \kappa_{quark}(Q^2).\end{aligned} \tag{2.64}$$

The ratio involved in the one loop expansion of Q_W^p is

$$\begin{aligned}&\frac{\mathcal{M}_{mix,\text{ Fermion Loop}}|_{\lambda=-1/2} - \mathcal{M}_{mix,\text{ Fermion Loop}}|_{\lambda=1/2}}{\mathcal{M}_Z|_{\lambda=-1/2} - \mathcal{M}_Z|_{\lambda=1/2}} Q_W^{p,LO} \\ &\qquad = -4(\kappa_f(Q^2) - 1)\sin^2\theta_W(M_Z^2).\end{aligned} \tag{2.65}$$

Fig. 2.5 displays the running of $\sin^2\theta_W$ due to the fermion loop. The value of α was chosen at the Z pole. Fig. 2.6 breaks down the running into the lepton and quark contributions. The top quark contribution is neglible and is not included.

The behavior of the plots can be understood if we look closely at the logarithm:

$$\log\left[\frac{m_i^2 + x(1-x)M_Z^2}{m_i^2 + x(1-x)Q^2}\right] = \log\left[\frac{M_Z^2}{m_i^2}\right] + \log\left[\frac{m_i^2/M_Z^2 + x(1-x)}{1 + x(1-x)Q^2/m_i^2}\right]. \tag{2.66}$$

When $Q^2 < m_i^2$, the first logarithm dominates. Fermions with smaller masses produce a larger value for the first logarithm. At low Q^2 we clearly see the contribution of each fermion follows the mass spectrum, with lighter fermions producing a larger contribution. As Q^2 increases the second logarithm decreases the overall contribution. This decrease does not become substantial until $Q^2 = m_i^2$. Thus, the contribution of each fermion remains relatively constant for $Q^2 < m_i^2$.

The quark contributions are greater than the lepton contributions for two reasons. First, g_V^i is larger for quarks than for charged leptons. Second, the quark contributions are tripled due to the sum over color. All the fermion contributions converge to 0 as $Q^2 \to M_Z^2$ because of our choice for the renormalization condition.

Our fermion contribution is smooth and calculated using the conventions of Czarnecki and Marciano [17, 18, 19]. In contrast, the fermion contribution to the $\sin^2\theta_W$ running plot calculated by Erler *et al.* [16, 20] is not smooth. The jaggedness comes about because they chose not to include particle i in the summation of $\kappa_f(Q^2)$ when $Q^2 < m_i^2$. They also evaluated Eq. (2.66) in the limit $Q^2 >> m_i^2$. Taking the high Q^2 limit of Eq. (2.66) and plugging it into Eq. (2.64) gives the Erler *et al.* expression for $\kappa_f(Q^2)$:

$$\kappa_f(Q^2)|_{\text{Erler}} = 1 + \frac{\alpha}{6\pi\sin^2\theta_W}\sum_i\sum_{\text{color}} Q_i g_V^i\left\{\log\left[\frac{M_Z^2}{m_i^2}\right] + \log\left[\frac{m_i^2}{Q^2}\right]\Theta(Q^2 - m_i^2)\right\}, \quad (2.67)$$

where $\Theta(Q^2 - m_i^2)$ is the Heaviside step function.

The above quark loop analyses for both Czarnecki and Marciano and Erler *et al.* overlook a crucial problem at low Q^2. As discussed by Marciano and Sirlin [21] and Czarnecki and Marciano [17], QCD effects in the quark loops dominate at low Q^2 and electroweak calculations are insufficient. Estimates of these low Q^2 loops are found by performing dispersion relations on experimental results of $e^+e^- \to$ hadron reactions. For $Q^2 = 0$, Czarnecki and Marciano [17] give the overall correction to $\sin^2\theta_W(M_Z^2)$ as $\kappa(Q^2 = 0) = 1.0301 \pm 0.0025$. This correction yields $\sin^2\theta_W(0) = \kappa(0)\sin^2\theta_W(M_Z^2) = 0.2383 \pm 0.0006$. A more recent and precise value for $\kappa(0)$ was calculated by Erler *et al.* [20] and Ferroglia *et al.* [22]. The Erler *et al.* calculation yielded $\sin^2\theta_W(0) = \kappa(0)\sin^2\theta_W(M_Z^2) = 0.23867 \pm 0.00016$. We chose to use this more precise value instead of the Czarnecki and

Marciano result.

Following the lead of Czarnecki and Marciano [19], we consider QCD effects in the range $Q < 0.1$ GeV. Czarnecki and Marciano presumably chose an upper bound of $Q = 0.1$ GeV because it is at the scale of pion production. After including the W loop and pinch corrections of the next sections, we perform a simple modification to the total running of $\sin^2\theta_W$ by substituting $\sin^2\theta_W(Q^2) = 0.23867$ for $Q < 0.1$ GeV.

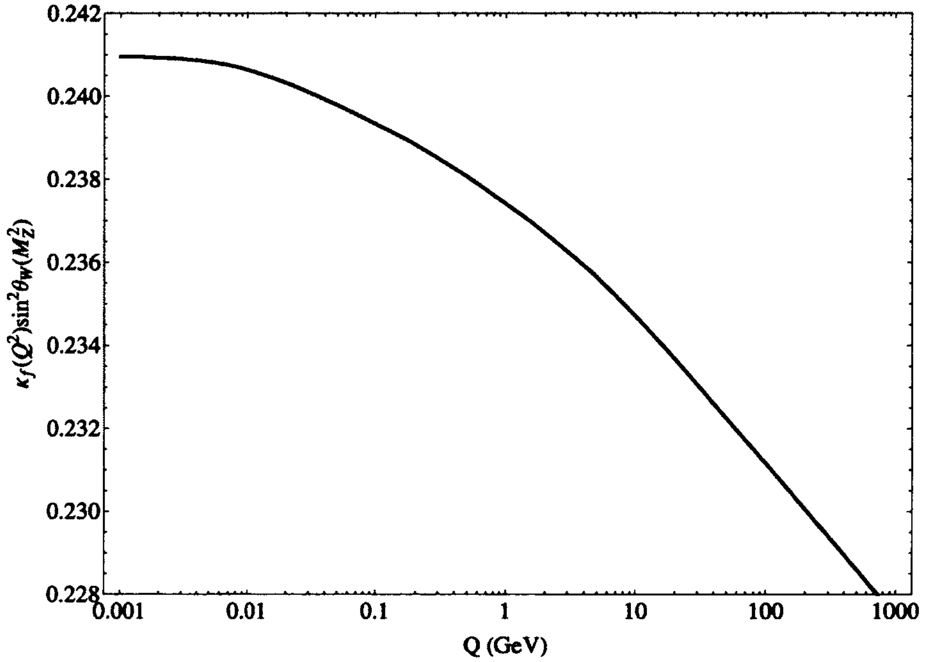

FIG. 2.5: The running of $\sin^2\theta_W$ due to γZ mixing via a fermion loop.

2.5.2 Contribution of the two W loop.

The mixing of a Z boson and a photon propagator can also occur via a W loop. In $\xi = 1$ gauge, there are five diagrams that contribute to the loop with two bosons (see

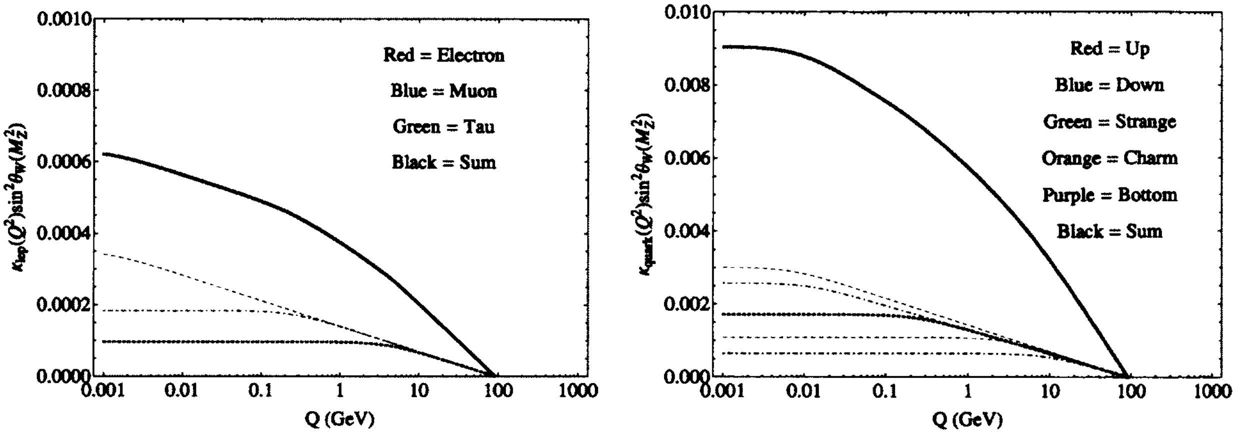

FIG. 2.6: Left: the running of $\sin^2\theta_W$ due to lepton loops. Right: the running due to quark loops.

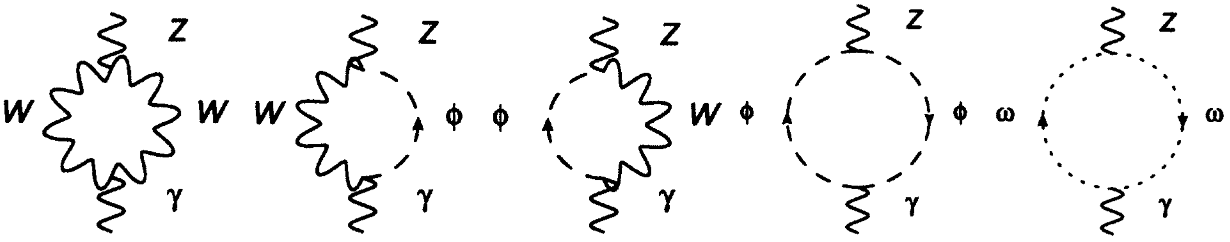

FIG. 2.7: Two boson loop diagrams in $\xi = 1$ gauge. The first diagram contains two W bosons. The second and third diagrams contain a W and Goldstone boson. The fourth diagram is a two Goldstone Boson loop and the fifth diagram is a ghost loop.

Fig. 2.7). The first diagram gives

$$\begin{aligned} i\Pi^1_{\alpha\beta,\text{W-Loop}} = &\int \frac{d^d\bar{q}}{(2\pi)^d}(-ig\cos\theta_W)\big[(2q+\bar{q})_\sigma g_{\alpha\rho} + (\bar{q}-q)_\rho g_{\alpha\sigma} \\ &+ (-q-2\bar{q})_\alpha g_{\sigma\rho}\big]\frac{-ig^{\rho\xi}}{(q+\bar{q})^2 - M_W^2} \\ &\times (-ie)\big[(-q+\bar{q})_\xi g_{\beta\tau} + (2q+\bar{q})_\tau g_{\xi\beta} + (-q-2\bar{q})_\beta g_{\tau\xi}\big]\frac{-ig^{\tau\sigma}}{\bar{q}^2 - M_W^2}. \end{aligned} \tag{2.68}$$

After invoking Eq. (2.59) and performing the momentum integrals, the amplitude reduces to

$$i\Pi^1_{\alpha\beta,\text{W-Loop}} = \frac{i}{(4\pi)^{\frac{d}{2}}}\int dx\Gamma\Big(2-\frac{d}{2}\Big)\Big(\frac{1}{\Delta}\Big)^{2-\frac{d}{2}} g\cos\theta_W e\Big(A - B\frac{d}{2}\frac{1}{1-\frac{d}{2}}\Delta\Big) \tag{2.69}$$

where

$$A = q_\alpha q_\beta\big(d-6-2(2d-3)x(1-x)\big) + g_{\alpha\beta}q^2\big(5-2x(1-x)\big) \tag{2.70}$$

and

$$B = g_{\alpha\beta}6\Big(1-\frac{1}{d}\Big). \tag{2.71}$$

The two diagrams with a W^+ and ϕ^+ give identical amplitudes. Their sum is

$$\begin{aligned} i\Pi^{2+3}_{\alpha\beta,\text{W-Loop}} &= 2\int \frac{d^d\bar{q}}{(2\pi)^d}\frac{-ig^{\rho\xi}}{(q+\bar{q})^2 - M_W^2}\frac{i}{\bar{q}^2 - M_W^2} \\ &\quad \times ieM_W g_{\beta\xi}(-ig)M_Z\sin^2\theta_W g_{\alpha\rho} \\ &= \frac{i}{(4\pi)^{\frac{d}{2}}}\int dx\Gamma\Big(2-\frac{d}{2}\Big)\Big(\frac{1}{\Delta}\Big)^{2-\frac{d}{2}} 2geM_W^2\frac{\sin^2\theta_W}{\cos\theta_W}g_{\alpha\beta}. \end{aligned} \tag{2.72}$$

In the above equation, we are allowed to make the substitution $M_Z\cos\theta_W = M_W$ since the gauge bosons are tree level.

The diagram with two ϕ^+ evaluates to

$$\begin{aligned} i\Pi^4_{\alpha\beta,\text{W-Loop}} &= \int \frac{d^d\bar{q}}{(2\pi)^d}\frac{i}{2}g\left(\cos\theta_W - \frac{\sin^2\theta_W}{\cos\theta_W}\right)(-q-2\bar{q})_\alpha\frac{i}{(q+\bar{q})^2-M_W^2} \\ &\times (ie)(-q-2\bar{q})_\beta\frac{i}{\bar{q}^2-M_W^2} \\ &= \frac{i}{(4\pi)^{\frac{d}{2}}}\int dx\Gamma\left(2-\frac{d}{2}\right)\left(\frac{1}{\Delta}\right)^{2-\frac{d}{2}}\frac{g}{2}\left(\cos\theta_W - \frac{\sin^2\theta_W}{\cos\theta_W}\right)e \\ &\times \left(C - D\frac{d}{2}\frac{1}{1-\frac{d}{2}}\Delta\right), \end{aligned} \tag{2.73}$$

where

$$C = q_\alpha q_\beta\big(1-4x(1-x)\big) \tag{2.74}$$

and

$$D = g_{\alpha\beta}\frac{4}{d}. \tag{2.75}$$

The ghost loop amplitude is given by

$$\begin{aligned} i\Pi^5_{\alpha\beta,\text{W-Loop}} &= (-1)\int \frac{d^d\bar{q}}{(2\pi)^d}\frac{-i}{(q+\bar{q})^2-M_W^2}\frac{-i}{\bar{q}^2-M_W^2}(-e)(-g\cos\theta_W)(q+\bar{q})_\alpha \\ &\times f^{abc}(-q+(q+\bar{q}))_\beta f^{cba} \\ &= \frac{i}{(4\pi)^{\frac{d}{2}}}\int dx\Gamma\left(2-\frac{d}{2}\right)\left(\frac{1}{\Delta}\right)^{2-\frac{d}{2}} \\ &\times g\cos\theta_W e\left(2x(1-x)q_\alpha q_\beta + g_{\alpha\beta}\frac{1}{1-\frac{d}{2}}\Delta\right) \end{aligned} \tag{2.76}$$

FIG. 2.8: One boson loop diagrams in $\xi = 1$ gauge. The first diagram contains one W boson. The second diagram contains one Goldstone boson.

2.5.3 Contribution of the single W loop.

In $\xi = 1$ gauge, there are two, one boson loop diagrams (see Fig. 2.8). The amplitude with one W propagator gives

$$\begin{aligned} i\Pi^6_{\alpha\beta,\text{W-Loop}} &= \int \frac{d^d\bar{q}}{(2\pi)^d}\frac{-ig^{\sigma\tau}}{\bar{q}^2 - M_W^2}(-ig\cos\theta_W e)(2g_{\alpha\beta}g_{\sigma\tau} - g_{\beta\sigma}g_{\alpha\tau} - g_{\beta\tau}g_{\alpha\sigma}) \\ &= \frac{i}{(4\pi)^{\frac{d}{2}}}\Gamma\left(2-\frac{d}{2}\right)\left(\frac{1}{M_W^2}\right)^{1-\frac{d}{2}}\frac{1}{1-\frac{d}{2}}2g\cos\theta_W e(d-1)g_{\alpha\beta} \end{aligned} \tag{2.77}$$

The amplitude with one ϕ propagator gives

$$\begin{aligned} i\Pi^7_{\alpha\beta,\text{W-Loop}} &= \int \frac{d^d\bar{q}}{(2\pi)^d}\frac{i}{\bar{q}^2 - M_W^2}(ieg)\big(\cos\theta_W - \frac{\sin^2\theta_W}{\cos\theta_W}\big)g_{\alpha\beta} \\ &= \frac{i}{(4\pi)^{\frac{d}{2}}}\Gamma\left(2-\frac{d}{2}\right)\left(\frac{1}{M_W^2}\right)^{1-\frac{d}{2}}\frac{1}{1-\frac{d}{2}}ge\left(\cos\theta_W - \frac{\sin^2\theta_W}{\cos\theta_W}\right)g_{\alpha\beta} \end{aligned} \tag{2.78}$$

2.5.4 Sum of W loops.

The sum of $\Pi_{\alpha\beta}$ is

$$\begin{aligned} i\sum_i \Pi^i_{\alpha\beta,\text{W-Loop}} &= \frac{i}{(4\pi)^{\frac{d}{2}}} \int dx \Gamma\Big(2-\frac{d}{2}\Big)\Big(\frac{1}{\Delta}\Big)^{2-\frac{d}{2}} \\ &\times \Big[(q^2 g_{\alpha\beta} - q_\alpha q_\beta)\Big(ge\cos\theta_W (5 - 4x(1-x) - (3-\epsilon)(1-2x)^2) \\ &- ge\Big(\cos\theta_W - \frac{\sin^2\theta_W}{\cos\theta_W}\Big)\frac{1}{2}(1-2x)^2\Big) \\ &+ 2M_Z^2 ge\cos\theta_W g_{\alpha\beta}\Big] \\ &= \frac{i}{(4\pi)^2}\Big(\frac{2}{\epsilon} - \gamma + \log 4\pi - \log\Delta\Big) ge\cos\theta_W \\ &\times \Big[(q^2 g_{\alpha\beta} - q_\alpha q_\beta)(5 - 4x(1-x) \\ &- \frac{7}{2}(1-2x)^2 + \frac{1}{2}(1-2x)^2\tan^2\theta_W) + 2M_Z^2 g_{\alpha\beta}\Big] \\ &+ \frac{i}{(4\pi)^2} 2ge\cos\theta_W (1-2x)^2 (q^2 g_{\alpha\beta} - q_\alpha q_\beta), \end{aligned} \tag{2.79}$$

where $d = 4 - \epsilon$. To obtain this sum it was necessary to use the identity,

$$\frac{(M_W^2)^{1-\frac{\epsilon}{2}}}{1-\frac{\epsilon}{2}} = \int dx \Big(\frac{\Delta^{1-\frac{\epsilon}{2}}}{1-\frac{\epsilon}{2}} + \frac{1}{2}(1-2x)^2 q^2 \Delta^{-\frac{\epsilon}{2}}\Big). \tag{2.80}$$

Notice that this amplitude does not satisfy the Ward Identity. The "pinched" part of the anapole moments will add to this term and preserve gauge invariance. The pinch technique will be examined in the next section.

Substituting Eq. (2.79) into Eq. (2.58) gives

$$
\begin{aligned}
i\mathcal{M}_{mix,\text{W-Loop}} = {} & \left(\frac{-ig}{2\cos^2\theta_W}\right)^2 \bar{u}_{k',\lambda'}\gamma_\mu(g_V^e - g_A^e\gamma^5)u_{k,\lambda}\frac{-i}{q^2 - M_Z^2}\bar{u}_{p',s'}(\gamma^\mu)u_{p,s} \\
& \times \frac{\alpha}{2\pi}\left\{\left(\frac{2}{\epsilon} - \gamma + \log 4\pi - \log\Delta\right)\right. \\
& \times \cos^2\theta_W\left[\left(\frac{3}{2} + 10x(1-x)\right.\right. \\
& \left.\left. + \frac{1}{2}(1-2x)^2\tan^2\theta_W\right) + \frac{2}{q^2}M_Z^2 g_{\alpha\beta}\right] \\
& \left. + 2\cos^2\theta_W(1-2x)^2\right\}
\end{aligned}
\tag{2.81}
$$

To interpret this result as a correction to the weak mixing angle, we renormalize to define $\sin^2\theta_W$ at the Z pole and add it to the tree level Z exchange,

$$
\begin{aligned}
i\mathcal{M}_Z + i\mathcal{M}_{mix,\text{W-Loop}}\Big|_{\text{renorm}} = {} & \left(\frac{-ig}{2\cos^2\theta_W}\right)^2 \bar{u}_{k',\lambda'}\gamma^\mu(-g_A^e\gamma^5)u_{k,\lambda}\frac{-ig^{\mu\nu}}{q^2 - M_Z^2}\bar{u}_{p',s'}\gamma_\nu u_{p,s} \\
& \left(g_V^p + \frac{\alpha}{2\pi}\int dx \log\frac{M_W^2 + x(1-x)M_Z^2}{\Delta}\right. \\
& \times \left[\cos^2\theta_W\left(\frac{3}{2} + 10x(1-x)\right.\right. \\
& \left.\left.\left. + \frac{1}{2}(1-2x)^2\tan^2\theta_W\right) - \frac{2}{Q^2}M_W^2\right]\right).
\end{aligned}
\tag{2.82}
$$

This expression can be interpreted as giving

$$
\frac{1}{2}(1 - 4\sin^2\theta_W(Q^2)\big|_{mix}) = \frac{1}{2}(1 - 4\kappa_b(Q^2)\sin^2\theta_W(M_Z^2)),
\tag{2.83}
$$

where

$$\begin{aligned}\kappa_b(Q^2) = 1 - \frac{\alpha}{4\pi}\frac{1}{\sin^2\theta_W}\int dx \log\frac{M_W^2 + x(1-x)M_Z^2}{\Delta} \\ \times \left[\cos^2\theta_W\left(\frac{3}{2} + 10x(1-x)\right.\right. \\ \left.\left. + \frac{1}{2}(1-2x)^2\tan^2\theta_W\right) - \frac{2}{Q^2}M_W^2\right]. \qquad (2.84)\end{aligned}$$

2.6 Pinch Technique Evaluation of the Electron's Anapole Moment and the Proton Vertex.

The pinched part of the anapole moment diagrams is considered part of the definition of $\sin^2\theta_W(Q^2)$. The anapole diagram has two boson and one fermion propagator in its loop. The pinch technique [23] involves expanding the anapole moment to find a term which cancels the fermion propagator. The so-called pinch terms for the anapolo moment and the proton vertex effectively describe two boson loops and are added to the γZ mixing diagram. Together, they satisfy the Ward Identity.

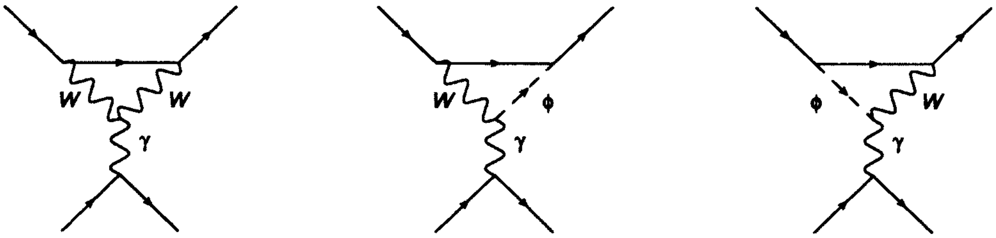

FIG. 2.9: One loop diagrams for the electron's anapole moment in $\xi = 1$ gauge. Only the first diagram has a non-zero pinch term.

In $\xi = 1$ gauge there are three relevant diagrams that contribute to the electron's anapole moment (See Fig. (2.9). A fourth diagram involving two Goldstone bosons is proportional to m^2/M_W^2 and can be neglected. The first amplitude is

$$\begin{aligned} i\mathcal{M}^1_{an} = {} & \left(\frac{-ig}{2\sqrt{2}}\right)^2 \bar{u}_{k',\lambda'}\gamma^\sigma(1-\gamma^5) \int \frac{d^d\bar{q}}{(2\pi)^d} \frac{-ig_{\sigma\tau}}{(q-\bar{q})^2 - M_W^2} \frac{-ig_{\alpha\mu}}{\bar{q}^2 - M_W^2} \frac{i(\not{k} - \not{\bar{q}})}{(k-\bar{q})^2} \\ & \times \gamma^\mu(1-\gamma^5)u_{k,\lambda}(-ie)\left[(-q-\bar{q})^\tau g^{\alpha\beta} + (2q-\bar{q})^\alpha g^{\beta\tau} + (2\bar{q}-q)^\beta g^{\tau\alpha}\right] \\ & \times \frac{-ig_{\beta\nu}}{q^2}\bar{u}_{p',s'}(-ie\gamma^\nu)u_{p,s}. \end{aligned} \tag{2.85}$$

Expanding this equation gives the pinch term as

$$\begin{aligned} i\mathcal{M}^1_{an}|_{\text{pinch}} = {} & \left(\frac{-ig}{2\sqrt{2}}\right)^2 (-ie)^2(-4i) \int \frac{d^d\bar{q}}{(2\pi)^d} \frac{1}{(q-\bar{q})^2 - M_W^2} \frac{1}{\bar{q}^2 - M_W^2} \\ & \times \bar{u}_{k',\lambda'}\gamma^\beta(1-\gamma^5)u_{k,\lambda}\frac{-ig_{\beta\nu}}{q^2}\bar{u}_{p',s'}\gamma^\nu u_{p,s} \\ = {} & \left(\frac{-ig}{2\sqrt{2}}\right)^2 \frac{-\alpha}{\pi} \int dx \log\left[\frac{M_W^2 + x(1-x)M_Z^2}{\Delta}\right] \\ & \times \bar{u}_{k',\lambda'}\gamma^\beta(1-\gamma^5)u_{k,\lambda}\frac{-ig_{\beta\nu}}{q^2}\bar{u}_{p',s'}\gamma^\nu u_{p,s}, \end{aligned} \tag{2.86}$$

where $\Delta = M_W^2 - x(1-x)q^2$.

Renormalizing at the Z pole and only focusing on the axial contribution gives

$$\begin{aligned} i\mathcal{M}^1_{an}|_{\text{pinch}} = {} & \left(\frac{-ig}{2\cos^2\theta_W}\right)^2 \bar{u}_{k',\lambda'}\gamma^\mu(-g^e_A\gamma^5)u_{k,\lambda}\frac{-ig_{\mu\nu}}{q^2 - M_Z^2}\bar{u}_{p',s'}\gamma^\nu u_{p,s} \\ & \frac{\alpha}{\pi}\cos^2\theta_W \int dx \log\left[\frac{M_W^2 + x(1-x)M_Z^2}{\Delta}\right]\frac{Q^2 + M_Z^2}{Q^2}. \end{aligned} \tag{2.87}$$

The amplitudes for the electron's other two anapole moment diagrams add to

$$\begin{aligned} i\mathcal{M}_{an}^{2+3} = {} & \left(\frac{-ig}{2\sqrt{2}}\right)^2 \frac{m}{M_W}\bar{u}_{k',\lambda'} \int \frac{d^d\bar{q}}{(2\pi)^d}\left\{\gamma^\mu(1-\gamma^5)\frac{-ig_{\beta\mu}}{(q-\bar{q})^2-M_W^2} iM_W e g^{\beta\tau}\right. \\ & \times \frac{i(\not{k}-\bar{\not{q}})}{(k-\bar{q})^2}\frac{i}{\bar{q}^2-M_W^2}(1+\gamma^5) \\ & \left. + (1-\gamma^5)\frac{i}{(q-\bar{q})^2-M_W^2} iM_W e g^{\beta\tau}\frac{i(\not{k}-\bar{\not{q}})}{(k-\bar{q})^2}\frac{-ig_{\beta\mu}}{\bar{q}^2-M_W^2}\gamma^\mu(1-\gamma^5)\right\}u_{k,\lambda} \\ & \times \frac{-ig_{\beta\nu}}{q^2}\bar{u}_{p',s'}(-ie\gamma^\nu)u_{p,s}. \end{aligned} \tag{2.88}$$

The numerator of this amplitude does not have the necessary momentum-dependence to produce a pinch term. It does not contribute to the running of the weak mixing angle.

Notice that the lepton anapole moment Eq. (2.87) alone is adequate to cancel the Ward Identity-violating piece of Eq. (2.81). However, we must also add the pinch part of the proton's vertex correction (see Fig. 2.3) for Z exchange to preserve the Ward Identity in the general gauge [24]. We approximate the intermediate fermion as a massless quark.

As with the lepton's anapole moment, in $\xi = 1$ gauge there is only one amplitude for the proton's vertex correction that possesses a non-zero pinch part. This amplitude is

$$\begin{aligned} i\mathcal{M}_p = {} & \left(\frac{-ig}{2\sqrt{2}}\right)^2 \frac{-ig}{2\cos\theta_W}\bar{u}_{k',\lambda'}\gamma^\nu(g_V^e - g_A^e\gamma^5)u_{k,\lambda} \\ & \times \frac{-ig_{\beta\nu}}{q^2-M_Z^2}u_{p',s'}\gamma^\mu(1-\gamma^5)(\not{p}''-\bar{\not{q}})\gamma_\tau(1-\gamma^5)u_{p,s} \\ & \times (-ig\cos\theta_W)\left[(q-\bar{q})^\tau g_\mu^\beta + (-2q-\bar{q})_\mu g^{\beta\tau} + (2\bar{q}+q)^\beta g_\mu^\tau\right] \\ & \times \int \frac{d^d\bar{q}}{(2\pi)^d}\frac{-i}{(\bar{q}^2-M_W^2)((\bar{q}+q)^2-M_W^2)(p''+\bar{q})^2} \end{aligned} \tag{2.89}$$

Expanding this equation gives the pinch term. Renormalizing at the Z pole and keeping only the lepton's axial contribution gives

$$i\mathcal{M}_p|_{\text{pinch}} = \left(\frac{-ig}{2\cos^2\theta_W}\right)^2 \bar{u}_{k',\lambda'}\gamma^\mu(-g_A^e\gamma^5)u_{k,\lambda}\frac{-ig_{\mu\nu}}{q^2-M_Z^2}\bar{u}_{p',s'}\gamma^\nu(1-\gamma^5)u_{p,s}$$
$$\times \frac{\alpha}{4\sin^2\theta_W\pi}\cos^2\theta_W\int dx \log\left[\frac{M_W^2+x(1-x)M_Z^2}{\Delta}\right]. \tag{2.90}$$

One further manipulation must be made. The hadron current is

$$\bar{u}_{p',s'}\gamma_\nu(1-\gamma^5)u_{p,s} = 4J_\nu^3$$
$$= 4J_\nu^Z + 4\sin^2\theta_W J_\nu^{em} \tag{2.91}$$

The neutral current contribution is dropped since it will not contribute to the running of $\sin^2\theta_W$. The relevant part of the pinch term is

$$i\mathcal{M}_p|_{\text{pinch}} = \left(\frac{-ig}{2\cos^2\theta_W}\right)^2 \bar{u}_{k',\lambda'}\gamma^\mu(-g_A^e\gamma^5)u_{k,\lambda}\frac{-ig_{\mu\nu}}{q^2-M_Z^2}\bar{u}_{p',s'}\gamma^\nu u_{p,s}$$
$$\times \frac{\alpha}{\pi}\cos^2\theta_W\int dx \log\left[\frac{M_W^2+x(1-x)M_Z^2}{\Delta}\right]. \tag{2.92}$$

This expression can be interpreted as giving

$$\frac{1}{2}(1-4\sin^2\theta_W(Q^2)|_{mix,\text{W-Loop}} - 4\sin^2\theta_W(Q^2)|_{\text{pinch}}) = \frac{1}{2}(1-4\kappa_b'(Q^2)\sin^2\theta_W(M_Z^2)) \tag{2.93}$$

where

$$\kappa_b'(Q^2) = 1 - \frac{\alpha}{4\pi}\frac{1}{\sin^2\theta_W}\int dx \log\frac{M_W^2+x(1-x)M_Z^2}{\Delta}$$
$$\times\left(\cos^2\theta_W(5+12x(1-x)) + \frac{1}{2}(1-2x)^2\right). \tag{2.94}$$

Fig. 2.10 shows the contribution of the boson loop added with the "pinched" part of the electron's anapole moment and the proton's vertex correction. This curve is smooth and follows the conventions of Czarnecki and Marciano [17, 18, 19]. In contrast, the boson contribution to the $\sin^2\theta_W$ running plot calculated by Erler *et al.* [16, 20] is jagged. It appears Erler and collaborators make similar approximations to what were made in their fermion calculation. Their boson curve is proportional to $\log(M_W^2/Q^2)\Theta(Q^2 - M_W^2)$.

The ratio involved in the one loop expansion of Q_W^p is

$$\begin{aligned}\frac{(\mathcal{M}_{mix,\text{W-Loop}} + \mathcal{M}_{an})|_{\lambda=-1/2} - (\mathcal{M}_{mix,\text{W-Loop}} + \mathcal{M}_{an})|_{\lambda=1/2}}{\mathcal{M}_Z|_{\lambda=-1/2} - \mathcal{M}_Z|_{\lambda=1/2}} Q_W^{p,LO} \\ = -4(\kappa_b'(Q^2) - 1)\sin^2\theta_W(M_Z^2). \qquad (2.95)\end{aligned}$$

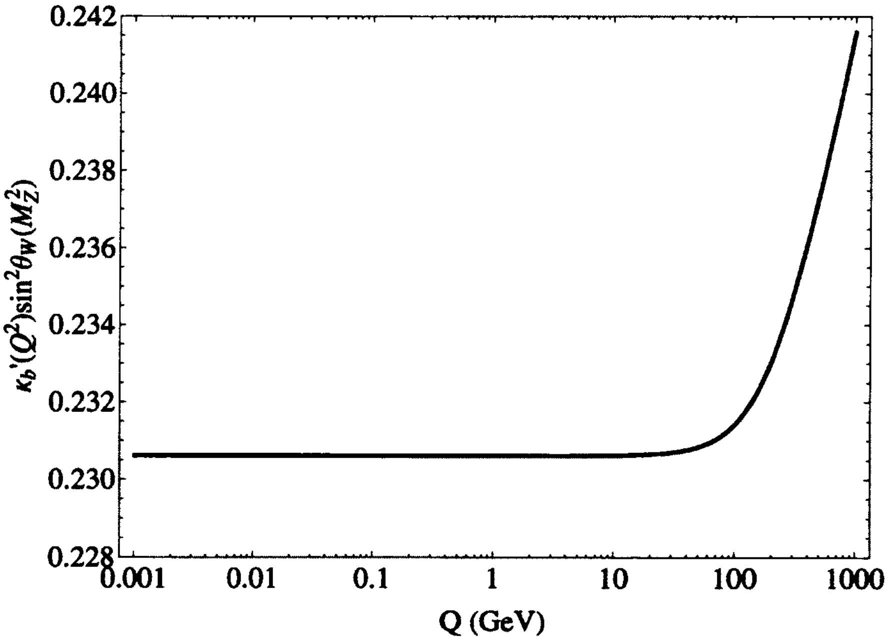

FIG. 2.10: The running of $\sin^2\theta_W$ due to γZ mixing via a W loop and the pinched parts of the electron's anapole moment and proton vertex correction.

The total running of the weak mixing angle is

$$1 - 4\sin^2\theta_W(Q^2) = 1 - 4(\kappa_f(Q^2) + \kappa_b'(Q^2) - 1)\sin^2\theta_W(M_Z^2). \tag{2.96}$$

It is necessary to subtract a 1 when we add the κ's to avoid overcounting the tree level diagram. The total running is shown in Fig. 2.11. As previously discussed, this curve was calculated following the conventions of Czarnecki and Marciano [17, 18, 19]. The jaggedness of the Erler *et al.* [16, 20] plot is due to approximations of the loop logarithms and removing particle contributions to the fermion loops when $Q^2 < m_i^2$. At low Q^2 QCD effects in the fermion loop dominate and the QED running calculation is no longer meaningful. As previously mentioned, for $Q < 0.1$ GeV we used the value $\sin^2\theta_W$=0.23867 calculated by Erler *et al.* [20] in this region.

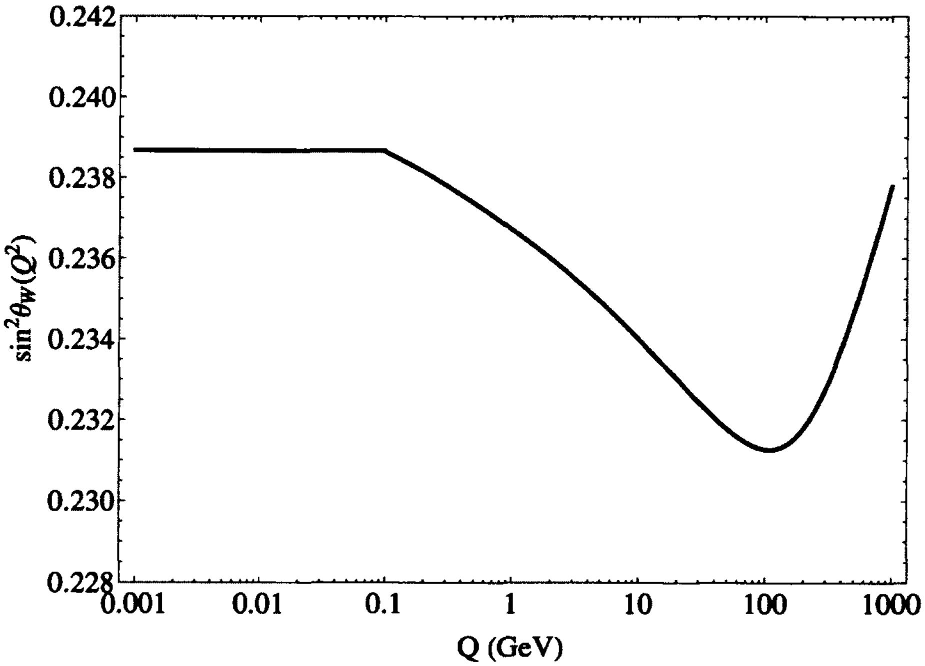

FIG. 2.11: The total running of $\sin^2\theta_W$.

2.7 Comparison of our Definition of Q_W^P to Erler *et al.*

Combining all of our results from the previous sections, our definition of Q_W^p up to one loop order at $Q^2 = 0$ is

$$Q_W^p = (\rho_{NC} + \Delta_e) Q_W^{p,LO} + \Delta_e' - 4(\kappa_f(0) + \kappa_b'(0) - 2)\sin^2\theta_W(M_Z^2) \\ + \Box_{WW} + \Box_{ZZ} + \Box_{\gamma Z} \tag{2.97}$$

We have chosen our renormalization at the Z pole. Thus, $Q_W^{p,LO} = 1 - 4\sin^2\theta_W(M_Z^2)$. Up to one loop order we are free to make the substitution

$$\begin{aligned} &\Delta_e' - 4(\kappa_f(0) + \kappa_b'(0) - 2)\sin^2\theta_W(M_Z^2) \\ &\qquad = (\rho_{NC} + \Delta_e)\left[\Delta_e' - 4(\kappa_f(0) + \kappa_b'(0) - 2)\sin^2\theta_W(M_Z^2)\right] \\ &\qquad = (1 + \Delta\rho + \Delta_e)\left[\Delta_e' - 4(\kappa_f(0) + \kappa_b'(0) - 2)\sin^2\theta_W(M_Z^2)\right], \end{aligned} \tag{2.98}$$

since $\Delta\rho + \Delta_e$ multiplied by the terms in square brackets are higher order corrections that can be dropped. Performing this substitution in Eq. (2.97) yields

$$Q_W^p = [\rho_{NC} + \Delta_e]\left[Q_W^{P,LO} + \Delta_e' - 4(\kappa_f(0) + \kappa_b'(0) - 2)\sin^2\theta_W(M_Z^2)\right] + \Box_{WW} + \Box_{ZZ} + \Box_{\gamma Z}. \tag{2.99}$$

Using the running $\sin^2\theta_W$ definition of Eq. 2.96 returns the Erler *et al.* result:

$$Q_W^p = [\rho_{NC} + \Delta_e][1 - 4\sin^2\theta_W(0) + \Delta_e'] + \Box_{WW} + \Box_{ZZ} + \Box_{\gamma Z}. \tag{2.100}$$

CHAPTER 3

Evaluation of the γZ Box

Marciano and Sirlin first examined the diagrams $\mathcal{M}_{\gamma Z}$, Fig. 3.1, in their study of $O(\alpha)$ radiative corrections to parity violation in atomic systems [25, 21]. Due to the presence of a massless propagator, $\mathcal{M}_{\gamma Z}$ contains low momentum contributions in which the use of pQCD is invalid.

Erler *et al.* [16] concisely express the Marciano and Sirlin result for the proton case as

$$\begin{aligned}\Box_{\gamma Z} &= \frac{\mathcal{M}_{\gamma Z}|_{\lambda=-1/2} - \mathcal{M}_{\gamma Z}|_{\lambda=1/2}}{\mathcal{M}_{Z}|_{\lambda=-1/2} - \mathcal{M}_{Z}|_{\lambda=1/2}} Q_W^{p,LO} \\ &= \frac{5\alpha}{2\pi}(1-4\sin^2\theta_W)\left(\log\frac{M_Z^2}{\Lambda^2} + C_{\gamma Z}(\Lambda)\right). \end{aligned} \tag{3.1}$$

The first term of the above expression comes from the pQCD regime while the second covers the low momentum regime. In the pQCD regime $\mathcal{M}_{\gamma Z}$ was evaluated directly in a manner similar to $\mathcal{M}_{WW}$ and $\mathcal{M}_{ZZ}$. Additionally, it was assumed that the incoming electron energy could be set to zero and the struck quarks behaved non-relativistically.

Below the momentum scale $\Lambda \approx 1$ GeV, the constant term $C_{\gamma Z}(\Lambda)$ both canceled the Λ dependence of the pQCD regime and estimated the magnitude of low momentum exchange. Erler *et al.*'s estimate of $C_{\gamma Z}(\Lambda)$ was $3/2 \pm 1$. Accounting for the prefactor, this term contributes only a 0.65% uncertainty to Q_W^p. Erler *et al.* argued that a more thorough analysis of $C_{\gamma Z}(\Lambda)$ could shift its central value but was unlikely to change the error bars.

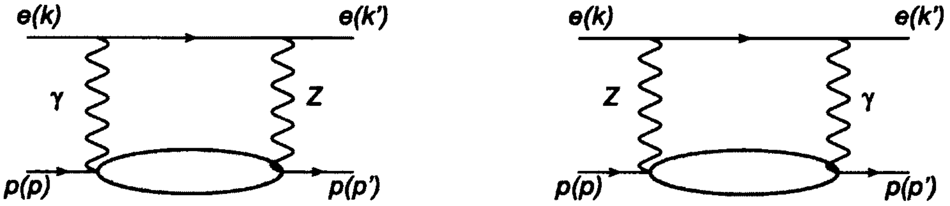

FIG. 3.1: Diagrams for $\mathcal{M}_{\gamma Z}$.

Gorchtein and Horowitz [26] suggested the $\Box_{\gamma Z}$ could be more thoroughly evaluated using a dispersive analysis. Here, the important details to note are that $\Box_{\gamma Z}$ depended on the electron's energy and its error bars were more than double those found by Erler *et al.* This surprising result inspired a check of the dispersive analysis by Sibirtsev *et al.* [27]. Their analytic expression for the dispersion relation was twice that of Gorchtein and Horowitz. We performed a third examination of the dispersion relation [28] and agreed with the expression found by Sibirtsev *et al.* Gorchtein *et al.* [29] reanalyzed their work and now all three groups agree on the analytic form of $\Box_{\gamma Z}$. The details of the dispersive analysis are described in Section 3.1.

The expression for $\Box_{\gamma Z}$ contains presently unmeasured proton structure functions, $F_{1,2,3}^{\gamma Z}(x, Q^2)$. Models for these structure functions must be constructed in order to evaluate $\Box_{\gamma Z}$. Models for $F_{1,2}^{\gamma Z}(x, Q^2)$ are presented in [27, 28, 29, 30]. Models for $F_3^{\gamma Z}(x, Q^2)$ are found in [31, 32, 33]. Section 3.2 describes our model for the structure functions as well as the models used by other groups. Section 3.3 presents the numerical evaluation of $\Box_{\gamma Z}$.

3.1 Dispersive Analysis of $\Box_{\gamma Z}$

3.1.1 Optical Theorem and the Evaluation of the Imaginary Term of $\mathcal{M}_{\gamma Z}$

The Qweak experiment measured electrons scattered off a proton target that exchanged momentum $Q^2 = 0.026$ GeV^2. By approximating this momentum exchange as zero, the optical theorem can be invoked. If the initial and final states of an interaction are the same, then the imaginary part of the amplitude is given by

$$\operatorname{Im} \mathcal{M}_{aa} = \frac{1}{2}\sum_{b}(2\pi)^4\delta^{(4)}(p_a - p_b)\mathcal{M}_{ab}\mathcal{M}_{ba}. \tag{3.2}$$

where subscript "a" labels identical initial and final states and subscript "b" indicates intermediate states.

Invoking the optical theorem, the amplitude for the γZ exchange gives

$$\begin{aligned}\operatorname{Im} \mathcal{M}_{\gamma Z} = \frac{1}{2}\int \frac{d^3\vec{k}_1}{(2\pi)^3 2E_1}&[-(ie)^2]\left(\frac{-ig}{2cos\theta_W}\right)^2 \frac{-1}{q^2}\frac{-1}{q^2 - M_Z^2} \\ &\times \left\{ \sum_{\lambda_1} \bar{u}(k)\gamma^\mu(g_V^e - g_A^e\gamma_5)u(k_1,\lambda_1)\bar{u}(k_1,\lambda_1)\gamma^\nu u(k) \right. \\ &\times \int d^4\eta e^{iq\eta}\langle ps\,|J_{Z\mu}(\eta)J_{\gamma\nu}(0)|\,ps\rangle \\ &+ \sum_{\lambda_1} \bar{u}(k)\gamma^\mu u(k_1,\lambda_1)\bar{u}(k_1,\lambda_1)\gamma^\nu(g_V^e - g_A^e\gamma_5)u(k) \\ &\left. \times \int d^4\eta e^{iq\eta}\langle ps\,|J_{\gamma\mu}(\eta)J_{Z\nu}(0)|\,ps\rangle \right\},\end{aligned} \tag{3.3}$$

where $\vec{k}_1$ and E_1 are the 3-momenta and energy of the intermediate electron.

Rewriting the first line of Eq. (3.3) in terms of G_F, α, and $q^2 = -Q^2$ gives

$$\text{1st Line} = \frac{1}{2}\left(\frac{-2}{\sqrt{2}}G_F\right) 4\pi\alpha \int \frac{d^3\vec{k}_1}{(2\pi)^3 2E_1} \frac{1}{Q^2\left(\frac{Q^2}{M_Z^2}+1\right)}. \tag{3.4}$$

In the limit of a massless electron, the second and fourth lines of Eq. (3.3) yield identical results. Summing over the intermediate spin λ_1, the electron contribution is

$$\begin{aligned}\sum_{\lambda_1} \bar{u}(k)\gamma^\mu u(k_1,\lambda_1)\bar{u}(k_1,\lambda_1)\gamma^\nu(g_V^e - g_A^e\gamma_5)u(k) &= 2(g_V^e - (2\lambda)g_A^e) \\ &\quad\times \left(k_1^\mu k^\nu + k_1^\nu k^\mu - k_1\cdot k g^{\mu\nu} - i(2\lambda)\epsilon^{\mu\nu\alpha\beta}k_\alpha k_{1\beta}\right) \\ &= L_{\gamma Z}^{\mu\nu} \end{aligned} \tag{3.5}$$

where λ is the the helicity of the electron and $\epsilon^{0123} = +1$.

We define the hadronic contribution to Eq. (3.3) as

$$\int d^4\eta e^{iq\eta}\langle ps\,|(J_{Z\mu}(\eta)J_{\gamma\nu}(0) + J_{\gamma\mu}(\eta)J_{Z\nu}(0))|\,ps\rangle = 4\pi W_{\mu\nu}^{\gamma Z}. \tag{3.6}$$

where

$$\begin{aligned} W_{\mu\nu}^{\gamma Z} = \Bigg[&\left(-g_{\mu\nu} + \frac{q_\mu q_\nu}{q^2}\right) F_1^{\gamma Z}(x,Q^2) + \frac{p_\mu p_\nu}{p\cdot q}F_2^{\gamma Z}(x,Q^2) \\ &- i\epsilon_{\mu\nu\sigma\tau}\frac{q^\sigma p^\tau}{2p\cdot q}F_3^{\gamma Z}(x,Q^2)\Bigg]. \end{aligned} \tag{3.7}$$

$F_{1,2,3}^{\gamma Z}(x,Q^2)$ are off-diagonal (γZ) structure functions. Little data exists for the γZ structure functions at low momenta so they are modeled by modifying electromagnetic structure functions $F_{1,2,3}^{\gamma\gamma}(x,Q^2)$ fitted to electromagnetic data. It should be noted that the numerical differences between calculations of $\Box_{\gamma Z}$ are due to different models for $F_{1,2,3}^{\gamma Z}(x,Q^2)$.

Combining Eqs. (3.4), (3.5), and (3.6), we see that Eq. (3.3) becomes

$$
\begin{aligned}
\operatorname{Im}\mathcal{M}_{\gamma Z} = {} & \frac{1}{2}\left(\frac{-2}{\sqrt{2}}G_F\right)4\pi\alpha\int\frac{d^3\vec{k}_1}{(2\pi)^3 2E_1}\frac{1}{Q^2\left(\frac{Q^2}{M_Z^2}+1\right)} \\
& \times 2(g_V^e-(2\lambda)g_A^e)(k_1^\mu k^\nu + k_1^\nu k^\mu - k_1\cdot k g^{\mu\nu} - i(2\lambda)\epsilon^{\mu\nu\alpha\beta}k_\alpha k_{1\beta}) \\
& \times 4\pi\Bigg[\left(-g_{\mu\nu}+\frac{q_\mu q_\nu}{q^2}\right)F_1^{\gamma Z}(x,Q^2)+\frac{p_\mu p_\nu}{p\cdot q}F_2^{\gamma Z}(x,Q^2) \\
& - i\epsilon_{\mu\nu\sigma\tau}\frac{q^\sigma p^\tau}{2p\cdot q}F_3^{\gamma Z}(x,Q^2)\Bigg].
\end{aligned}
\tag{3.8}
$$

Evaluating the last two lines of Eq. (3.8) and substituting $Q^2 = -q^2 \approx 2k\cdot k_1$ gives

$$
\begin{aligned}
8\pi(g_V^e-(2\lambda)g_A^e)Q^2\Bigg\{ & \left[F_1^{\gamma Z}(x,Q^2)+AF_2^{\gamma Z}(x,Q^2)\right] \\
& - (2\lambda)BF_3^{\gamma Z}(x,Q^2)\Bigg\}.
\end{aligned}
\tag{3.9}
$$

where $A = \frac{2p\cdot k_1 p\cdot k}{Q^2 p\cdot q} - \frac{p^2}{2p\cdot q}$ and $B = \frac{p\cdot k + p\cdot k_1}{2p\cdot q}$.

Substituting Eq. (3.9) into Eq. (3.8) and subtracting right- and left-handed electron amplitudes gives

$$
\begin{aligned}
\operatorname{Im}\mathcal{M}_{\gamma Z;\lambda=-1/2} - \operatorname{Im}\mathcal{M}_{\gamma Z;\lambda=1/2} = {} & -\frac{16\pi}{\sqrt{2}}G_F 4\pi\alpha\int\frac{d^3\vec{k}_1}{(2\pi)^3 2E_1} \\
& \times\Bigg\{g_A^e\frac{F_1^{\gamma Z}(x,Q^2)+AF_2^{\gamma Z}(x,Q^2)}{\frac{Q^2}{M_Z^2}+1} \\
& + g_V^e\frac{BF_3^{\gamma Z}(x,Q^2)}{\frac{Q^2}{M_Z^2}+1}\Bigg\}.
\end{aligned}
\tag{3.10}
$$

3.1.2 Calculation of $\mathrm{Im}\,\Box_{\gamma Z}$

Dividing Eq. (3.10) by lowest order Z exchange gives $\mathrm{Im}\,\Box_{\gamma Z}$:

$$\begin{aligned}\mathrm{Im}\,\Box_{\gamma Z} &= \frac{\mathrm{Im}\,\mathcal{M}_{\gamma Z}|_{\lambda=-1/2} - \mathrm{Im}\,\mathcal{M}_{\gamma Z}|_{\lambda=1/2}}{\mathcal{M}_Z|_{\lambda=-1/2} - \mathcal{M}_Z|_{\lambda=1/2}} Q_W^{p,LO} \\ &= \frac{2\pi 4\pi\alpha}{Q_W^{p,LO}} \int \frac{d^3\vec{k}_1}{(2\pi)^3 2E_1} \left\{ \frac{F_1^{\gamma Z}(x,Q^2) + AF_2^{\gamma Z}(x,Q^2)}{p\cdot k\left(\frac{Q^2}{M_Z^2}+1\right)} \right. \\ &+ \left. \frac{g_V^e}{g_A^e} \frac{BF_3^{\gamma Z}(x,Q^2)}{p\cdot k\left(\frac{Q^2}{M_Z^2}+1\right)} \right\} Q_W^{p,LO}. \end{aligned} \tag{3.11}$$

We desire to change the integration variables from $\vec{k}_1$ to Q^2 and W^2. In the low mass limit of the electron

$$\frac{d^3\vec{k}_1}{(2\pi)^3 2E_1} \approx \frac{2\pi E_1^2 d(cos\theta) dE_1}{(2\pi)^3 2E_1}. \tag{3.12}$$

In the center of mass frame the intermediate electron energy is

$$\begin{aligned} E_1^{CM} &= \frac{s-W^2}{2\sqrt{s}} \\ \Rightarrow dE_1^{CM} &= \frac{-dW^2}{2\sqrt{s}}. \end{aligned} \tag{3.13}$$

In the above expression, $s = (p+k)^2$ is the Mandelstam variable. Q^2 in the center of mass frame is

$$\begin{aligned} Q^2 = 2k\cdot k_1 &= 2E^{CM}E_1^{CM}(1-cos\theta) \\ \Rightarrow d(cos\theta) &= \frac{-dQ^2}{2E^{CM}E_1^{CM}}. \end{aligned} \tag{3.14}$$

Substituting these differentials into Eq. (3.12) gives

$$\begin{aligned}\frac{d^3\vec{k}_1}{(2\pi)^3 2E_1^{CM}} &= \frac{2\pi(E_1^{CM})^2}{(2\pi)^3 2E_1^{CM}}\frac{-dQ^2}{2E^{CM}E_1^{CM}}\frac{-dW^2}{2\sqrt{s}} \\ &= \frac{dQ^2dW^2}{(2\pi)^2 8E^{CM}\sqrt{s}}\end{aligned} \tag{3.15}$$

Subsituting $E^{CM} = \frac{s-M^2}{2\sqrt{s}}$, where M is the proton mass, gives

$$\frac{d^3\vec{k}_1}{(2\pi)^3 2E_1^{CM}} = \frac{dQ^2dW^2}{(2\pi)^2 4(s-M^2)} \tag{3.16}$$

Substituting these new differentials into Eq. (3.11) gives

$$\begin{aligned}\mathrm{Im}\,\Box_{\gamma Z} = \frac{\alpha}{2}\int \frac{dQ^2dW^2}{(s-M^2)p\cdot k}\Bigg\{&\frac{F_1^{\gamma Z}(x,Q^2)+AF_2^{\gamma Z}(x,Q^2)}{\frac{Q^2}{M_Z^2}+1} \\ &+\frac{g_V^e}{g_A^e}\frac{BF_3^{\gamma Z}(x,Q^2)}{\frac{Q^2}{M_Z^2}+1}\Bigg\}.\end{aligned} \tag{3.17}$$

In the lab frame $p\cdot k = \frac{s-M^2}{2}$. Thus, $\mathrm{Im}\,\Box_{\gamma Z}$ is

$$\begin{aligned}\mathrm{Im}\,\Box_{\gamma Z}(E_{Lab}) = \frac{\alpha}{(s-M^2)^2}\int_{W_\pi^2}^{s} dW^2 \int_0^{Q^2_{max}} dQ^2\Bigg\{&\frac{F_1^{\gamma Z}(x,Q^2)+AF_2^{\gamma Z}(x,Q^2)}{\frac{Q^2}{M_Z^2}+1} \\ &+\frac{g_V^e}{g_A^e}\frac{BF_3^{\gamma Z}(x,Q^2)}{\frac{Q^2}{M_Z^2}+1}\Bigg\} \\ = \mathrm{Im}\,\Box_{\gamma Z}^V(E_{Lab}) + \mathrm{Im}\,\Box_{\gamma Z}^A(E_{Lab}).\end{aligned} \tag{3.18}$$

where $Q^2_{max} = \frac{(s-M^2)(s-W^2)}{s}$. This limit is found by plugging $\cos\theta = -1$ into Eq. (3.14). W^2 represents the square of the intermediate hadron mass of the diagram. The minimum mass, W_π^2, is the sum of the proton and a single pion mass and the maximum occurs when all of the initial 4-momenta squared, s, is converted into mass squared.

The first term of Eq. (3.18) is labeled with a superscript "V" since it is associated with vector hadronic structure functions. Similarly, the second term is labeled with an "A" to indicate it contains the axial hadronic structure function.

3.1.3 Dispersion Relations for $\mathrm{Re}\,\Box_{\gamma Z}(E_{Lab})$

We convert the imaginary term of the γZ box to its real term via a dispersion relation over incoming electron energy. The dispersion relation is constructed by evaluating a contour integral in the energy plane. To perform this integral we must understand the imaginary term's behavior under negative energies.

Let us once again examine Eqs. (3.5) and (3.6). A particle with a negative energy is identified as its antiparticle with positive energy. For a positron, Eq. (3.5) evaluates to

$$\text{Positron Line} = 2(g_V^e - (2\lambda)g_A^e)(k_1^\mu k^\nu + k_1^\nu k^\mu - k_1 \cdot k g^{\mu\nu} + i(2\lambda)\epsilon^{\mu\nu\alpha\beta}k_\alpha k_{1\beta}). \tag{3.19}$$

The only difference compared to the electron line is the sign of the Levi-Civita. The hadronic contribution remains the same for both electron and positron scattering. Combining the positron and hadronic contributions gives $\mathrm{Im}\,\mathcal{M}_{\gamma Z;\lambda=-1/2} - \mathrm{Im}\,\mathcal{M}_{\gamma Z;\lambda=1/2}$ for positron scattering. Compared to Eq. (3.10), the positron amplitude difference has the same sign for the terms proportional to $F_1^{\gamma Z}$ and $F_2^{\gamma Z}$ and the opposite sign for the term proportional to $F_3^{\gamma Z}$.

To complete our analysis of the behavior of $\mathrm{Im}\,\Box_{\gamma Z}(E)$ for negative energies, we must also calculate $\mathcal{M}_Z$ for positron scatterings:

$$i\mathcal{M}_Z|_{\text{positron}} = \left(\frac{-ig}{2\cos^2\theta_W}\right)^2 \bar{v}_{k,\lambda}\gamma^\mu(g_V^e - g_A^e\gamma^5)v_{k',\lambda'}\frac{-ig_{\mu\nu}}{q^2 - M_Z^2 + i\epsilon}\bar{u}_{p',s'}\gamma^\nu(g_V^p - g_A^p\gamma^5)u_{p,s}. \tag{3.20}$$

For electron scattering, $\gamma^5 u_{k,\lambda} \to (2\lambda) u_{k,\lambda}$. Positron scattering yields the opposite sign, $\gamma^5 v_{k,\lambda} \to -(2\lambda) v_{k,\lambda}$.

Combining the positron results for $\mathrm{Im}\,\mathcal{M}_{\gamma Z}$ and $\mathcal{M}_Z$ gives us the behavior of $\mathrm{Im}\,\Box_{\gamma Z}(E)$ at negative energies. For the positron we see that terms proportional to $F_1^{\gamma Z}$ and $F_2^{\gamma Z}$ have opposite signs as that for electron scattering while the term proportional to $F_3^{\gamma Z}$ has the same sign. Thus, $\mathrm{Im}\,\Box_{\gamma Z}^V(E_{Lab})$ is an odd function while $\mathrm{Im}\,\Box_{\gamma Z}^A(E_{Lab})$ is an even function.

$\mathrm{Re}\,\Box_{\gamma Z}^V$ is given by the following dispersion relation:

$$\mathrm{Re}\,\Box_{\gamma Z}^V(E_{Lab}) = \frac{2E_{Lab}}{\pi} \int_{\nu_\pi}^{\infty} \frac{dE'_{Lab}}{E'^2_{Lab} - E^2_{Lab}} \mathrm{Im}\,\Box_{\gamma Z}^V(E'_{Lab}). \tag{3.21}$$

where $\nu_\pi = (W_\pi^2 - M^2)/2M$.

Evaluating this triple integral in its present ordering is a time-consuming process. Examining Eq. (3.18) we see that the energy dependent terms can be seperated from those dependent on Q^2 and W^2. The vector part of Eq. (3.18) becomes

$$\begin{aligned} \mathrm{Im}\,\Box_{\gamma Z}^V(E_{Lab}) = {} & \frac{\alpha}{(2ME_{Lab})^2} \int_{W_\pi^2}^{s} dW^2 \int_0^{Q^2_{max}} dQ^2 \frac{F_1^{\gamma Z} - \frac{M^2 F_2^{\gamma Z}}{W^2 - M^2 + Q^2}}{1 + \frac{Q^2}{M_Z^2}} \\ & - \frac{\alpha}{2ME_{Lab}} \int_{W_\pi^2}^{s} dW^2 \int_0^{Q^2_{max}} dQ^2 \frac{F_2^{\gamma Z}}{Q^2 \left(1 + \frac{Q^2}{M_Z^2}\right)} \\ & + \alpha \int_{W_\pi^2}^{s} dW^2 \int_0^{Q^2_{max}} dQ^2 \frac{F_2^{\gamma Z}}{Q^2 \left(1 + \frac{Q^2}{M_Z^2}\right)(W^2 - M^2 + Q^2)}. \end{aligned} \tag{3.22}$$

We see that the energy integral can be evaluated analytically if we change the order of integration. In terms of generic functions, Eq. (3.21) is

$$f(E) = \sum_{i=1}^{3} \int_{\nu_\pi}^{\infty} dE' g_i(E, E') \int_{W_\pi^2}^{2ME' + M^2} dW^2 \int_0^{2ME'\left(1 - \frac{W^2}{M^2 + 2ME'}\right)} dQ^2 h_i(Q^2, W^2) \tag{3.23}$$

where $g_i(E, E')$ represents the three different E' integrands, $h_i(Q^2, W^2)$ are the three Q^2 and W^2 integrands, and the "Lab" subscript has been dropped.

To slide the energy integral through the W^2 integral we must change their integration bounds. Solving the upper bound of the W^2 integral in terms of energy gives a lower bound of $E' = \frac{W^2-M^2}{2M}$. Eq. (3.23) becomes

$$f(E) = \sum_{i=1}^{3} \int_{W_\pi^2}^{\infty} dW^2 \int_{\frac{W^2-M^2}{2M}}^{\infty} dE' g_i(E, E') \int_0^{2ME'\left(1-\frac{W^2}{M^2+2ME'}\right)} dQ^2 h_i(Q^2, W^2). \tag{3.24}$$

To slide the energy integral through the Q^2 integral, the bounds change yet again. Solving the upper bound of the Q^2 integral in terms of energy gives a new lower bound of $E_{min} = \frac{1}{4M}(W^2 - M^2 + Q^2 + \sqrt{(}(W^2 - M^2 + Q^2)^2 + 4M^2Q^2))$. Eq. (3.24) becomes

$$f(E) = \sum_{i=1}^{3} \int_{W_\pi^2}^{\infty} dW^2 \int_0^{\infty} dQ^2 h_i(Q^2, W^2) \int_{E_{min}}^{\infty} dE' g_i(E, E'). \tag{3.25}$$

Solving for each of the energy integrals gives

$$\begin{aligned} \int_{E_{min}}^{\infty} dE' g_1(E, E') &= \frac{2E\alpha}{\pi} \int_{E_{min}}^{\infty} \frac{dE'}{E'^2 - E^2} \frac{1}{(2ME')^2} \\ &= -\frac{2E\alpha}{(2M)^2\pi} \left(\frac{1}{E^2 E_{min}} + \frac{1}{2E^3} \log\left(\frac{|E_{min} - E|}{E_{min} + E} \right) \right), \end{aligned} \tag{3.26}$$

$$\begin{aligned} \int_{E_{min}}^{\infty} dE' g_2(E, E') &= -\frac{2E\alpha}{\pi} \int_{E_{min}}^{\infty} \frac{dE'}{E'^2 - E^2} \frac{1}{2ME'} \\ &= \frac{2E\alpha}{2M\pi} \frac{1}{2E^2} \log\left(\frac{|E_{min}^2 - E^2|}{E_{min}^2} \right), \end{aligned} \tag{3.27}$$

$$\begin{aligned}\int_{E_{min}}^{\infty} dE' g_3(E,E') &= \frac{2E\alpha}{\pi}\int_{E_{min}}^{\infty}\frac{dE'}{E'^2-E^2}\\ &= -\frac{2E\alpha}{\pi}\frac{1}{2E}\log\left(\frac{|E_{min}-E|}{E_{min}+E}\right).\end{aligned} \tag{3.28}$$

Substituting these integrals along with their respective $h_i(Q^2,W^2)$ integrands into Eq. (3.25) gives

$$\begin{aligned}\mathrm{Re}\,\Box^{V}_{\gamma Z}(E) = \int_{W_\pi^2}^{\infty} dW^2\int_0^{\infty} dQ^2\Bigg[&-\frac{2E\alpha}{(2M)^2\pi}\left(\frac{1}{E^2E_{min}}\right.\\ &\left.+\frac{1}{2E^3}\log\left(\frac{|E_{min}-E|}{E_{min}+E}\right)\right)\frac{F_1^{\gamma Z}-\frac{M^2F_2^{\gamma Z}}{W^2-M^2+Q^2}}{1+\frac{Q^2}{M_Z^2}}\\ &+\frac{2E\alpha}{2M\pi}\frac{1}{2E^2}\log\left(\frac{|E_{min}^2-E^2|}{E_{min}^2}\right)\frac{F_2^{\gamma Z}}{Q^2(1+\frac{Q^2}{M_Z^2})}\\ &-\frac{2E\alpha}{\pi}\frac{1}{2E}\log\left(\frac{|E_{min}-E|}{E_{min}+E}\right)\frac{F_2^{\gamma Z}}{Q^2\left(1+\frac{Q^2}{M_Z^2}\right)(W^2-M^2+Q^2)}\Bigg].\end{aligned} \tag{3.29}$$

The dispersion relation for the axial contribution is

$$\mathrm{Re}\,\Box^{A}_{\gamma Z}(E_{Lab}) = \frac{2}{\pi}\int_{\nu_\pi}^{\infty}\frac{E'_{Lab}dE'_{Lab}}{E'^2_{Lab}-E^2_{Lab}}\mathrm{Im}\,\Box^{A}_{\gamma Z}(E'_{Lab}). \tag{3.30}$$

Performing the same order of integration flips as the vector case, the axial dispersion relation becomes

$$\begin{aligned}\mathrm{Re}\,\Box^{A}_{\gamma Z}(E_{Lab}) = \frac{2}{(2M)^2\pi}\int_{W_\pi^2}^{\infty} dW^2\int_0^{\infty} dQ^2\alpha\frac{g_V^e}{g_A^e}\Bigg[&\frac{1}{4E^2_{Lab}}\log\left(\frac{|E^2_{min}-E^2_{Lab}|}{E^2_{min}}\right)\\ &-\frac{M}{E_{Lab}(W^2-M^2+Q^2)}\log\left(\frac{|E_{min}-E_{Lab}|}{E_{min}+E_{Lab}}\right)\Bigg]\frac{F_3^{\gamma Z}}{1+\frac{Q^2}{M_Z^2}}.\end{aligned} \tag{3.31}$$

Notice that α and $g_V^e/g_A^e = 1 - 4\sin^2\theta_W$ are placed inside the integrals. Like Blunden *et al.* [31], we chose to consider the running values of α and the weak mixing angle since the axial γZ box is sensitive to large Q^2. It should also be noted that Eq. (3.31) reproduces the original Marciano and Sirlin result in the $E_{Lab} \to 0$, elastic limit.

3.2 Analysis of $F_{1,2,3}^{\gamma Z}(x, Q^2)$

As previously mentioned, little data exists for the off-diagonal structure functions $F_{1,2,3}^{\gamma Z}(x, Q^2)$. At high momenta these structure functions can be constructed directly using parton distribution functions. In the resonance region off-diagonal structure functions must be modeled by modifying existing fits to $F_{1,2,3}^{\gamma\gamma}(x, Q^2)$. We chose to modify these fits using an $SU(6)$ constituent quark model. Gorchtein *et al.* modified the electromagnetic fits using photoproduction data from the Particle Data Group [2]. A third alternative is to modify the fits using helicity amplitude fits from MAID [34].

3.2.1 Evaluation of $F_{1,2}^{\gamma Z}(x, Q^2)$

Evaluation of Nonresonance Region

To evaluate the remaining double integrals it is necessary to patch together several different fits for $F_1^{\gamma Z}$ and $F_2^{\gamma Z}$ as each is only valid over a specific range of momenta. In our analysis [28] we considered three regions of momenta (see Fig. 3.2). In the scaling region ($Q^2 > 5$ GeV^2 and $W > 2.5$ GeV) we constructed the γZ structure functions directly using CTEQ parton distribution functions [35]. The expression for the off-diagonal structure functions in the scaling region is

$$F_2^{\gamma Z}(x, Q^2) = 2xF_1^{\gamma Z}(x, Q^2) = x\sum_{q,\bar{q}} 2e_q g_V^q(q(x, Q^2) + \bar{q}(x, Q^2)) \tag{3.32}$$

where q ($\bar{q}$) are quark (antiquark) distributions for the proton. Roughly 3% of $\mathrm{Re}\,\Box_{\gamma Z}^{V}(E = 1.165\ \mathrm{GeV})$ is from the CTEQ fit. Its contribution is so negligible that we did not perform any uncertainty analysis for this term.

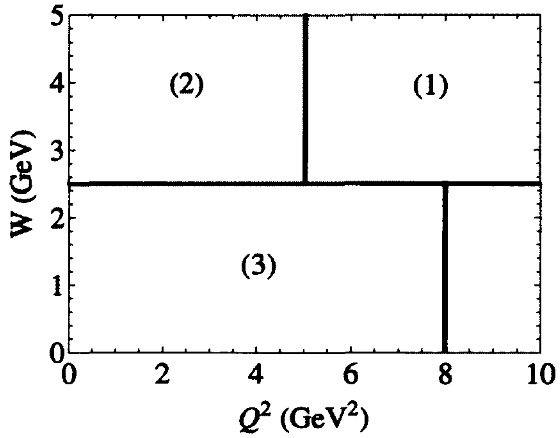

FIG. 3.2: Breakdown of our $F_{1,2}^{\gamma Z}$ fits. (1) is the scaling region. In region (2) we modify the fit by Capella *et al.* [36]. (3) is the resonance region. We consider contributions outside of these regions to be negligible.

In the region $Q^2 \leq 5\ \mathrm{GeV}^2$ and $W > 2.5$ GeV we modified electromagnetic fits by Capella *et al.* [36]. We wanted the Capella and CTEQ fits to smoothly connect at the $Q^2 = 5\ \mathrm{GeV}^2$ boundary. We settled on the modification

$$F_2^{\gamma Z}|_{Capella} = \left[\frac{Q^2}{5\ \mathrm{GeV}^2}\left(\left.\frac{F_2^{\gamma Z}}{F_2^{\gamma\gamma}}\right|_{CTEQ,Q^2=5\ \mathrm{GeV}^2} - 1\right) + 1\right] F_2^{\gamma\gamma}|_{Capella}. \tag{3.33}$$

The uncertainty for the Capella region was estimated to be

$$\Delta F_2^{\gamma Z}|_{Capella} = (F_2^{\gamma\gamma}|_{Capella} - F_2^{\gamma Z}|_{Capella})|_{Q^2=5\ \mathrm{GeV}^2}. \tag{3.34}$$

Roughly 15% of the total uncertainty in $\mathrm{Re}\,\Box_{\gamma Z}^{V}(E = 1.165\ \mathrm{GeV})$ is due to the Capella fit. Fig. 3.3 shows the transition from the Capella to Cteq regions at $W^2 = 7\ \mathrm{GeV}^2$.

It should be noted that the elastic contribution of the vector γZ box was calculated in [37, 38]. It was found to be a factor of $Q_W^{p,LO}$ smaller than the inelastic contributions. This factor comes about for elastic collisions at the proton, Z boson vertex. Because the contribution of the elastic collision is so small, we will not discuss it further.

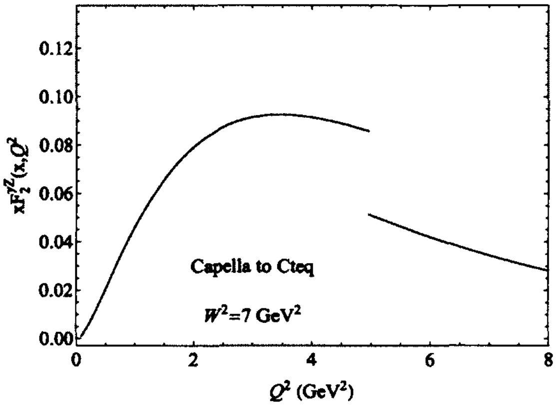

FIG. 3.3: Transition from the Capella to Cteq regions at $W^2 = 7$ GeV^2. Without the modification, the Capella *et al.* fit lies roughly on the upper uncertainty bound at the $Q^2 = 5$ GeV^2 transition.

Evaluation of Resonance Region

For the resonance region ($Q^2 \leq 8$ GeV^2 and $W \leq 2.5$ GeV) we modified the Christy and Bosted electromagnetic fit [39]. Their $F_1^{\gamma\gamma}$, σ_T, and σ_L fits sum a smooth background with the contributions from seven resonances: $P_{33}(1232)$, $S_{11}(1535)$, $D_{13}(1520)$, $F_{15}(1680)$, $S_{11}(1650)$, $P_{11}(1440)$, and $F_{37}(1950)$. Their description and computer code for their fit allowed us to separately modify the resonances and the background. For the resonances, our goal was to find prefactors for the summation

$$F_1^{\gamma Z} = \sum_{res} C_{res} \times F_1^{\gamma\gamma}|_{res} \tag{3.35}$$

such that

$$C_{res} = \left.\frac{F_1^{\gamma Z}}{F_1^{\gamma\gamma}}\right|_{res}. \tag{3.36}$$

Following the normalization of the Particle Data Group [2], the resonant parts of these structure functions can be expressed as a product of the polarization vector, $\epsilon_+^\mu = 1/\sqrt{2}(0, -1, -i, 0)$, and hadronic tensors:

$$\begin{aligned} F_1^{\gamma\gamma(\gamma Z)}\Big|_{N\rightarrow res} &= \epsilon_+^{\mu *}\epsilon_+^{\nu} W_{\mu\nu}^{\gamma\gamma(\gamma Z)} \\ &= (2)\sum_\lambda \int \mathrm{d}^4\mathrm{z} e^{iqz}\big\langle N, s\big|\epsilon_+^* \cdot J^{\gamma(Z,V)}(z)\big|res, \lambda\big\rangle \\ &\times \big\langle res, \lambda\big|\epsilon_+ \cdot J^{\gamma}(0)\big|N, s\big\rangle \\ &= A_\lambda^\gamma(2A_\lambda^Z)A_\lambda^\gamma, \end{aligned} \tag{3.37}$$

where λ and s are the spin projections of the resonance and nucleon, respectively, and γ (Z,V) is the electromagnetic (neutral vector) current. The couplings have been absorbed into the currents. The factor of 2 is present in γZ-exchange to account for the different orderings.

The corrective prefactor can be expressed in terms of helicity amplitudes,

$$C_{res} = \frac{2\sum_\lambda A_\lambda^\gamma A_\lambda^Z}{\sum_\lambda (A_\lambda^\gamma)^2}. \tag{3.38}$$

The above amplitudes can be evaluated by considering $\epsilon_+ \cdot J$ as a quark operator embedded between $SU(6)$ wave function representations of the nucleon and resonances [40]. This operator ignores the spatial wave functions, ψ, and acts only on the flavor, ϕ, and spin, χ, wave functions. Table 3.1 summarizes the multiplet and $SU(6)$ wave function for each resonance.

TABLE 3.1: Resonances and their multiplets. (A)S indicates an (anti)symmetric wave functions while M,(A)S indicates a wave function with two elements that are (anti)symmetric.

Resonance	Multiplet
Proton	$\vert ^2 8, 56\rangle = \frac{1}{\sqrt{2}}\psi^S_{L=0,L_Z=0}(\phi^{M,S}\chi^{M,S}_{S_Z=\pm 1/2} + \phi^{M,A}\chi^{M,A}_{S_Z=\pm 1/2})$
$P_{33}(1232)$	$\vert ^4 10, 56\rangle$
$S_{11}(1535)$	$\vert ^2 8, 70\rangle = \sum_{J_Z=S_Z+L_Z}\langle JJ_Z\vert LL_Z, SS_Z\rangle$ $\times\frac{1}{2}\left[\psi^{M,S}_{LL_Z}\left(\phi^{M,S}\chi^{M,S}_{S_Z} - \phi^{M,A}\chi^{M,S}_{S_Z}\right) + \psi^{M,A}_{LL_Z}\left(\phi^{M,S}\chi^{M,A}_{S_Z} + \phi^{M,A}\chi^{M,S}_{S_Z}\right)\right]$
$D_{13}(1520)$	$\vert ^2 8, 70\rangle$
$F_{15}(1680)$	$\vert ^2 8, 56\rangle$
$S_{11}(1650)$	$\vert ^4 8, 70\rangle = \frac{1}{\sqrt{2}}\psi^S_{L=0,L_Z=0}(\phi^{M,S}\chi^S_{S_Z=\pm 1/2} + \phi^{M,A}\chi^S_{S_Z=\pm 1/2})$
$P_{11}(1440)$	$\vert ^2 8, 56\rangle$
$F_{37}(1950)$	$\vert ^4 10, 56\rangle$

TABLE 3.2: Spin and flavor wave functions. For $S_Z = -1/2$, ↑↔↓ and the sign switches for the mixed symmetric and symmetric wave functions.

Flavor Wave Functions	Spin Wave Functions
$\phi^{M,S} = -\frac{1}{\sqrt{6}}((ud + du)u - 2uud)$	$\chi^{M,S}_{+1/2} = -\frac{1}{\sqrt{6}}((\uparrow\downarrow + \downarrow\uparrow)\uparrow - 2\uparrow\uparrow\downarrow)$
$\phi^{M,A} = \frac{1}{\sqrt{2}}(ud - du)u$	$\chi^{M,A}_{+1/2} = \frac{1}{\sqrt{2}}(\uparrow\downarrow - \downarrow\uparrow)\uparrow$
	$\chi^{S}_{+1/2} = \frac{1}{\sqrt{3}}(\uparrow\uparrow\downarrow + \uparrow\downarrow\uparrow + \downarrow\uparrow\uparrow)$

Because the colorless portion of the total hadronic wave function is symmetric, we are free to operate only on their third components of ϕ and χ and multiply the result by three. The amplitude can be expressed as

$$\begin{aligned}\langle res, \lambda \big| \epsilon_+ \cdot J^{\gamma(Z,V)} \big| N, s \rangle &= 3 \times e_q^{(3)} (g_V^{q(3)}) \\ &\times \langle \psi_{res} \phi_{res} \chi_\lambda \big| \bar{u}(k', \lambda') \epsilon_+ \cdot \gamma u(k, s') \big| \psi_N \phi_N \chi_s \rangle, \end{aligned} \tag{3.39}$$

where k (k') and s' (λ') are the initial (final) momentum and spin projection for the struck quark. The superscript "3" over the quark electromagnetic and weak vector couplings, e_q and g_V^q, indicates that the operators are acting only on the third quark.

Using unit normalized quark spinors,

$$u = \sqrt{\frac{E + m_q}{2m_q}} \begin{pmatrix} \xi_s \\ \frac{\vec{\sigma} \cdot \vec{p}}{2m_q} \xi_s \end{pmatrix}, \tag{3.40}$$

and choosing a frame where the gauge boson is propagating in the z-direction, the current reduces to

$$\bar{u}(k', \lambda') \epsilon_+ \cdot \gamma u(k, s') = \frac{\sqrt{2}}{2m_q} \xi_{\lambda'}^\dagger [P_+ + q_z S_+] \xi_{s'}, \tag{3.41}$$

where m_q is the constituent quark mass, $P_+ = k_1 + ik_2$, $S_+ = 1/2(\sigma_1 + i\sigma_2)$, q_z is the momentum of the boson, and ξ_s are the usual two spinors. The Wigner-Eckart theorem allows us to calculate a matrix element of P_+ as a constant times a matrix element of L_+.

After absorbing the spatial and momentum information, as well as the quark mass coefficient, into parameters A and B, Eq. (3.37) becomes

$$\begin{aligned} F_1^{\gamma\gamma(\gamma Z)}\Big|_{N\to res} = & \\ & 3\times e_q^{(3)}\left(2g_V^{q(3)}\right)\langle\psi_N\phi_N\chi_s\big|[AL_+ + BS_+]^\dagger\big|\psi_{res}\phi_{res}\chi_\lambda\rangle \\ & \times 3e_q^{(3)}\langle\psi_{res}\phi_{res}\chi_\lambda\big|[AL_+ + BS_+]\big|\psi_N\phi_N\chi_s\rangle \\ & = (2)A_\lambda^{\gamma(Z)}. \end{aligned} \tag{3.42}$$

To calculate these amplitudes we operated the Hamiltonian on the $SU(6)$ spatial (ψ), flavor (ϕ), and spin (χ) wave functions of protons and resonances described by Close [40]. As examples, inserting the Hamiltonian into the proton to $D_{13}(1520)$ helicity amplitudes gives

$$\begin{aligned} A_{\lambda=1/2}^{\gamma(Z)} &= 3\times e_q^{(3)}\left(g_V^{q(3)}\right)\langle\psi_{res}\phi_{res}\chi_{+1/2}\big|[AL_+ + BS_+]\big|\psi_N\phi_N\chi_s\rangle \\ &= \frac{1}{\sqrt{6}}\Big(-A_{10}\left[e_u(g_V^u)-e_d(g_V^d)\right] \\ &- \sqrt{2}B_{10}\left[\frac{5}{3}e_u(g_V^u)+\frac{1}{3}e_d g_V^d)\right]\Big) \end{aligned} \tag{3.43}$$

and

$$\begin{aligned} A_{\lambda=3/2}^{\gamma(Z)} &= 3\times e_q^{(3)}\left(g_V^{q(3)}\right)\langle\psi_{res}\phi_{res}\chi_{+3/2}\big|[AL_+ + BS_+]\big|\psi_N\phi_N\chi_s\rangle \\ &= -\frac{1}{\sqrt{2}}A_{10}\left[e_u(g_V^u)-e_d(g_V^d)\right], \end{aligned} \tag{3.44}$$

where λ is the spin projection of the resonance along the direction of the gauge boson momentum. The subscripts of A_{10} and B_{10} indicate the angular momentum dependence of the resonance's wave function.

Obtaining A_{10} and B_{10} without relying on hadronic wave functions requires additional phenomenological information. Data for both of the $D_{13}(1520)$ and $F_{15}(1680)$ resonances [41, 42] show that $A^{\gamma}_{3/2}$ dominates photoproduction whereas $A^{\gamma}_{1/2}$ dominates at high Q^2. Thus, the polarization ratio

$$A = \frac{|A^{\gamma}_{1/2}|^2 - |A^{\gamma}_{3/2}|^2}{|A^{\gamma}_{1/2}|^2 + |A^{\gamma}_{3/2}|^2} \tag{3.45}$$

is close to -1 for photoproduction, and evolves to $+1$ at higher Q^2. The expressions for $D_{13}(1520)$ at low Q^2 yield

$$A_{10}(Q^2 = 0) = -\sqrt{2}B_{10}(Q^2 = 0). \tag{3.46}$$

Since $A^{\gamma}_{1/2}$ is expected to dominate by a power of Q^2 at high Q^2, a form with the correct limits is

$$\frac{A_{10}(Q^2)}{B_{10}(Q^2)} = -\sqrt{2}\, f_1(Q^2) = -\sqrt{2}\frac{1}{1 + Q^2/\Lambda_1^2}\,. \tag{3.47}$$

This leads to

$$C_{D_{13}} = \frac{(\frac{1}{3} - f_1)(1 - f_1) + 3f_1^2}{(1 - f_1)^2 + 3f_1^2} + Q_W^{p,LO}\,. \tag{3.48}$$

A similar analysis gives

$$C_{F_{15}} = \frac{\frac{2}{3}(1 - f_2)}{(1 - f_2)^2 + 2f_2^2} + Q_W^{p,LO}\,. \tag{3.49}$$

We used $\Lambda_1^2 = \Lambda_2^2 = 0.2$ GeV^2 [28]. These values were chosen by comparing our fits constructed using Close's analysis with MAID fits [34] to transition amplitudes. Better agreement can be obtained by setting $\Lambda_1^2 = 0.256$ GeV^2 and $\Lambda_2^2 = 0.635$ GeV^2 (see Fig. 3.4), and while this more thorough analysis lowers the overall $\mathrm{Re}\,\Box^{V}_{\gamma Z}$ result, it does not do so by more than half a percent.

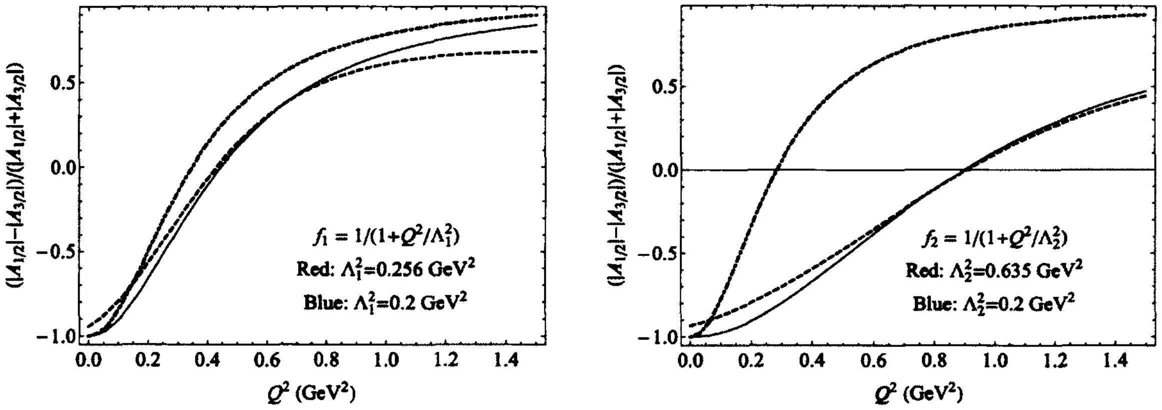

FIG. 3.4: Left: MAID helicity amplitude ratio (black curve) compared with the quark model fit with different Λ_1^2 values for D_{13}. Right: MAID helicity amplitude ratio (black curve) compared with the quark model fit with different Λ_2^2 values for F_{15}.

Table 3.3 summarizes the prefactors for each resonance in the Christy and Bosted fit. The prefactor for the Roper resonance is easily calculated and is Q^2-independent. The two S_{11} states belong to the same $SU(6)$ multiplet as the $D_{13}(1520)$, so A_{10} and B_{10} are the same for all three states, for valid $SU(6)$ symmetry. The S_{11} states can mix. The Moorhouse selection rule [43] indicates that the unmixed γp amplitude for the $S_{11}(1650)$ is zero when the values of the quark charges are inserted. Neglecting also the amplitude for the Z-boson case, the amplitude listed for the $S_{11}(1535)$ gives a ratio

$$C_{S_{11}} = \frac{\frac{1}{3} + 2f_1}{1 + 2f_1} + Q_W^{p,LO}\,. \tag{3.50}$$

In electroproduction, $S_{11}(1650)$ occurs because of mixing with the bare $S_{11}(1535)$, and the above ratio is the same for both the S_{11}'s.

C_{res} for $I = 3/2$ resonances are calculated by considering only the $\Delta I = 1$ portion of the current. This term is proportional to $(e_u - e_d)$. By substituting vector charges, C_{res}

for $I = 3/2$ resonances is found to be $(1 + Q_W^{p,LO})$.

The Christy-Bosted fit lies within 3% of nearly all data points. Our modifications to the resonances undoubtedly increase this uncertainty and we estimated it to be 10%. The uncertainty of the resonances contributes roughly 30% to the total uncertainty of $\mathrm{Re}\,\Box_{\gamma Z}^{V}(E = 1.165\text{ GeV})$.

The Christy-Bosted fit also accounts for a smooth background. To model the γZ-box background we considered two limiting cases. In the low x limit, the light quark distributions are expected to be equal and the corrective coefficient is

$$C_{bkgd}|_{x\to 0} = \frac{\sum_{q=u,d,s} 2e_q g_V^q f_q(x)}{\sum_{q=u,d,s} (e_q)^2 f_q(x)} = 1 + Q_W^{p,LO}. \tag{3.51}$$

In the limit where there are only valence quarks

$$C_{bkgd}|_{\text{valence quarks}} = \frac{\sum_{q=u,u,d} 2e_q g_V^q f_q(x)}{\sum_{q=u,u,d} (e_q)^2 f_q(x)} = \frac{2}{3} + Q_W^{p,LO}. \tag{3.52}$$

We used these limits as the error bounds and their average as the background correction.

The background limits were used as uncertainty bounds. A little over half of the total uncertainty in $\mathrm{Re}\,\Box_{\gamma Z}^{V}(E = 1.165\text{ GeV})$ is due to this background uncertainty.

$F_2^{\gamma\gamma}$ is related to $F_1^{\gamma\gamma}$ by

$$F_2^{\gamma\gamma} = \frac{Q^2}{p\cdot q}\left(1 + \frac{\sigma_L}{\sigma_T}\right)\frac{F_1^{\gamma\gamma}}{1 + \frac{M^2Q^2}{(p\cdot q)^2}}. \tag{3.53}$$

We substituted $F_1^{\gamma Z}$ into the above expression to obtain $F_2^{\gamma Z}$. We also assumed the modifications were the same for both the transverse and longitudinal cross sections.

TABLE 3.3: The seven Christy-Bosted resonances along with their electromagnetic helicity amplitudes along and corresponding corrective prefactors for the proton. The $(pZ \rightarrow N_p^*)$ helicity amplitudes are calculated by substituting $e_q \rightarrow g_V^q = T_q^3 - 2e_q \sin^2\theta_W(0)$.

resonance	proton electroproduction amplitudes	C^p_{res}
$P_{33}(1232)$	$A^\gamma_{1/2} \propto (e_u - e_d)$	$1 + Q_W^{p,LO}$
$S_{11}(1535)$	$A^\gamma_{1/2} = \frac{1}{\sqrt{6}}\big(\sqrt{2}A_{10}(e_u - e_d)$ $-B_{10}(\frac{5}{3}e_u + \frac{1}{3}e_d)\big)$	$\frac{1/3+2f_1}{1+2f_1} + Q_W^{p,LO}$
$D_{13}(1520)$	$A^\gamma_{1/2} = \frac{1}{\sqrt{6}}\big(A_{10}(e_u - e_d)$ $+\sqrt{2}B_{10}(\frac{5}{3}e_u + \frac{1}{3}e_d)\big)$ $A^\gamma_{3/2} = \frac{1}{\sqrt{2}}A_{10}(e_u - e_d)$	$\frac{(1-f_1)(1/3-f_1)+3f_1^2}{(1-f_1)^2+3f_1^2} + Q_W^{p,LO}$
$F_{15}(1680)$	$A^\gamma_{1/2} = \sqrt{\frac{2}{5}}A_{20}(2e_u + e_d)$ $+\sqrt{\frac{3}{5}}B_{20}(\frac{4}{3}e_u - \frac{1}{3}e_d)$ $A^\gamma_{3/2} = \frac{2}{\sqrt{5}}A_{20}(2e_u + e_d)$	$\frac{2/3(1-f_2)}{(1-f_2)^2+2f_2^2} + Q_W^{p,LO}$
$S_{11}(1650)$	$A^\gamma_{1/2} = -\sqrt{\frac{2}{27}}B_{10}(e_u + 2e_d)$	$\frac{1/3+2f_1}{1+2f_1} + Q_W^{p,LO}$
$P_{11}(1440)$	$A^\gamma_{1/2} = B_{00}(\frac{4}{3}e_u - \frac{1}{3}e_d)$	$2/3 + Q_W^{p,LO}$
$F_{37}(1950)$	$A^\gamma_{1/2} \propto (e_u - e_d)$	$1 + Q_W^{p,LO}$

3.2.2 Alternative Modification of $F_{1,2}^{\gamma\gamma}(x,Q^2) \rightarrow F_{1,2}^{\gamma Z}(x,Q^2)$

The transition amplitudes for C_{res} can be modeled using a different technique. The vector contribution to the Z-boson transition amplitudes can be isospin rotated into a sum of electromagnetic transition amplitudes, $p\gamma \rightarrow N_p^*$ and $n\gamma \rightarrow N_n^*$. This type of analysis was used by Gorchtein *et al.* [29].

Neglecting strange quark contributions, the transition amplitudes are

$$\langle N_p^* | J_\mu^{\gamma(Z,V)} | p \rangle = e_u (g_V^u) \langle N_p^* | \bar{u}\gamma_\mu u | p \rangle + e_d (g_V^d) \langle N_p^* | \bar{d}\gamma_\mu d | p \rangle \tag{3.54}$$

and

$$\langle N_n^* | J_\mu^{\gamma} | n \rangle = e_u \langle N_n^* | \bar{u}\gamma_\mu u | n \rangle + e_d \langle N_n^* | \bar{d}\gamma_\mu d | n \rangle. \tag{3.55}$$

After performing an isopin rotation the neutron amplitude becomes

$$\langle N_n^* | J_\mu^{\gamma} | n \rangle = e_u \langle N_p^* | \bar{d}\gamma_\mu d | p \rangle + e_d \langle N_p^* | \bar{u}\gamma_\mu u | p \rangle. \tag{3.56}$$

Further algebra on these amplitudes reveals

$$\langle N_p^* | J_\mu^{Z,V} | p \rangle = \frac{1}{2}(1 - 4\sin^2\theta_W(0)) \langle N_p^* | J_\mu^{\gamma} | p \rangle - \frac{1}{2} \langle N_n^* | J_\mu^{\gamma} | n \rangle. \tag{3.57}$$

C_{res} can now be written as

$$\begin{aligned} C_{res} &= 2\frac{\sum_\lambda A_\lambda^{\gamma,p} A_\lambda^{Z,p}}{\sum_\lambda (A_\lambda^{\gamma,p})^2} \\ &= Q_W^{p,LO} - \frac{\sum_\lambda A_\lambda^{\gamma,p} A_\lambda^{\gamma,n}}{\sum_\lambda (A_\lambda^{\gamma,p})^2} \end{aligned} \tag{3.58}$$

where superscripts "p" and "n" indicate proton and neutron amplitudes, respectively.

Gorchtein *et al.* [29] constructed their corrective ratios using photoproduction amplitudes listed in the Particle Data Group [2] to modify the resonance contributions of the Christy-Bosted fit [39]. Thus, their C_{res} expressions lack Q^2-dependence. To account for the amplitudes' Q^2-dependence, resonance amplitude fits from MAID [34] can be used.

Gorchtein *et al.* [29] disregarded the background of the Christy-Bosted fit and instead modified two Generalized Vector Dominance (GVD) models. Their Model I is based on the color dipole model of Cvetic *et al.* [44]. In this model a photon fluctuates into a $q-\bar{q}$ pair which interacts with the proton through gluon exchange. Their fit's parameters are constrained by data and are valid for low Q^2, high energy scattering. Gorchtein *et al.* isospin rotate this model to apply it to the γZ case. Their Model II is based on the generalized vector meson model of Alwall and Ingelman [45]. In this model the photon couples to the proton via vector meson intermediaries, given by ρ, ω, and ϕ as well as a background. It is valid for low Q^2, high energy scattering. As with the Model I modifications, the vector meson model is extrapolated to low energy and isospin rotated for the γZ case. Fig. 3.5 compares the $F_2^{\gamma\gamma}(x,Q^2)$ and $F_2^{\gamma Z}(x,Q^2)$ models obtained from our constituent quark model and Gorchtein *et al.*'s two models.

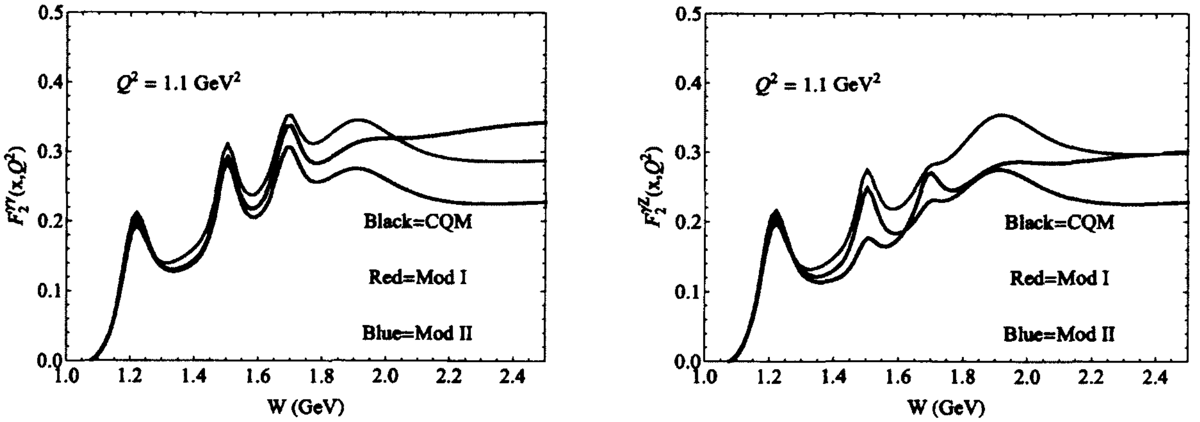

FIG. 3.5: Comparison of $F_2^{\gamma\gamma}(x,Q^2)$ and $F_2^{\gamma Z}(x,Q^2)$ obtained from our constituent quark model and Gorchtein *et al.*'s fits.

3.2.3 Evaluation of $F_3^{\gamma Z}(x, Q^2)$

Blunden *et al.* [31] split their $\mathrm{Re}\,\Box^A_{\gamma Z}$ analysis into elastic ($W^2 = M^2$), resonance ($W_\pi^2 \leq W^2 \leq 4$ GeV^2), and deep inelastic scaling ($W^2 > 4$ GeV^2) regions. To allow for an easier comparison between our analysis and theirs, we used the same energy regions in our evaluation of $\mathrm{Re}\,\Box^A_{\gamma Z}$ (see Fig. 3.6).

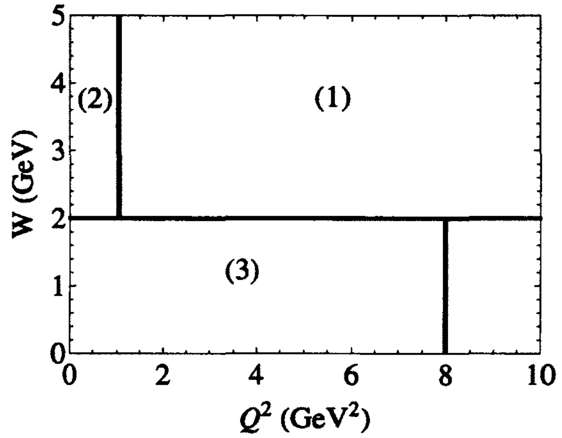

FIG. 3.6: Breakdown of our $F_3^{\gamma Z}$ fits. (1) is the scaling region. In region (2) we modify the scaling region fit. (3) is the resonance region. We consider contributions outside of these regions to be negligible.

The average Q^2 value within the $\mathrm{Re}\,\Box^V_{\gamma Z}$ integral is about 0.4 GeV^2. In contrast, the average Q^2 value within the $\mathrm{Re}\,\Box^A_{\gamma Z}$ integral is about 80 GeV^2. Thus, the axial contribution to the γZ-box diagram is less sensitive to the modifications of the structure functions in the resonance region. It is still important to construct as accurate a model as possible. Since the axial box integral is sensitive to high Q^2, we follow the example of Bunden *et al.* and evaluate the integral using one loop running values of $\alpha(Q^2)$ and $\sin^2\theta_W(Q^2)$.

Evaluation of Nonresonance Region

In the scaling region, ($W^2 > 4$ GeV^2 and $Q^2 \geq 1$ GeV^2), $F_3^{\gamma Z}$ can be directly calculated using parton distribution functions

$$F_3^{\gamma Z}(x,Q^2) = \sum_q 2e_q g_A^q \left(q(x,Q^2) - \bar{q}(x,Q^2)\right). \tag{3.59}$$

Blunden *et al.* use PDFs from [46]. As with our vector analysis, we use PDFs given by CTEQ [35]. To be conservative, we estimated a 10% uncertainty in the PDFs.

In the region ($W^2 > 4$ GeV^2 and $Q^2 < 1$ GeV^2) we use Blunden *et al.*'s Model I:

$$F_3^{\gamma Z}(x,Q^2) = \left(\frac{1+\Lambda^2/Q_0^2}{1+\Lambda^2/Q^2}\right) F_3^{\gamma Z}(x,Q_0^2) \tag{3.60}$$

where $Q_0^2 = 1$ GeV^2 and $\Lambda^2 = 0.7$ GeV^2.

We also estimated an uncertainty of 10% for this modification. Roughly 74% of the total uncertainty of $\mathrm{Re}\,\Box_{\gamma Z}^{A}(E = 1.165 \text{ GeV})$ is due to the scaling region while only 3% is due to Model I.

For the elastic contribution we exactly follow the technique used by Blunden *et al.* For elastic interactions, the structure function reduces to a form factor,

$$F_3^{\gamma Z}(Q^2) = -Q^2 G_M^p(Q^2) G_A^Z(Q^2) \delta(W^2 - M^2) \tag{3.61}$$

where G_M^P and G_A^Z and magnetic and axial vector form factors for the proton. G_M^p is parameterized by [47]. Like Blunden *et al.*, we also use $G_A^Z(Q^2) = -1.267/(1+Q^2/1 \text{ GeV}^2)^2$.

Evaluation of Resonance Region

The most significant departure from the Blunden *et al.* analysis is in the resonance region. In this region Blunden *et al.* constructed $F_3^{\gamma Z}$ using axial current parameters of Lalakulich *et al.* [48]. Lalakulich *et al.* obtained their parameters through a PCAC analysis of pionic decays of baryons. Their fit accounts for four resonances but makes no attempt at estimating a smooth background, defering the determination of its form to future experiments. As an aside, Lattice QCD calculations have reached a sufficient level of accuracy to calculate axial form factors [49, 50].

Instead of repeating the Blunden *et al.* resonance region analysis, we constructed $F_3^{\gamma Z}$ by once again modifying the Christy-Bosted fit. Not only does this modification provide a smooth background, it also accounts for three more resonances. In our analysis of the resonance region we repeated the technique outlined in Sec. 3.2.1. In the non-relativistic limit, $|\vec{k}| << m_q$, the axial currents becomes

$$\bar{u}(k',\lambda')\epsilon_+ \cdot \gamma\gamma_5 u(k,s') = \sqrt{2}\xi^\dagger_{\lambda'} S_+ \xi_{s'}. \tag{3.62}$$

Continuing the use of the parameters in Sec. 3.2.1, $F_3^{\gamma Z}$ can be expressed as

$$\begin{aligned} F_3^{\gamma Z}\Big|_{N\rightarrow res} &= \\ & 3\left(2g_A^{q(3)}\right)\frac{2\nu}{q_z}\langle\psi_N\phi_N\chi_s\big|[\frac{2m_q}{q_z}BS_+]^\dagger\big|\psi_{res}\phi_{res}\chi_\lambda\rangle \\ & \times 3e_q^{(3)}\langle\psi_{res}\phi_{res}\chi_\lambda\big|[AL_+ + BS_+]\big|\psi_N\phi_N\chi_s\rangle, \end{aligned} \tag{3.63}$$

where ν is the energy of the exchanged boson. For our calculation we took the mass of the struck quark m_q to be 0.3 GeV. Table 3.4 summarizes the corrective prefactors to obtain $F_3^{\gamma Z}$. As with the corrective prefactors for $F_{1,2}^{\gamma Z}$, we estimated a 10% uncertainty for this modification.

The smooth background is once again modified by taking the low x and valence quark limits. For low x, a quark and anti-quark are equally likely to be struck. Thus,

$$C_{bkgd}|_{x\to 0} = \frac{\sum_{q=u,d,s} 2e_q g_A^q f_q(x)}{\frac{1}{2}\sum_{q=u,d,s}(e_q)^2 f_q(x)} = 0. \tag{3.64}$$

In the limit where valence quarks are equally likely to be struck

$$C_{bkgd}|_{\text{valence quarks}} = \frac{\sum_{q=u,u,d} 2e_q g_A^q f_q(x)}{\frac{1}{2}\sum_{q=u,u,d}(e_q)^2 f_q(x)} = \frac{10}{3}. \tag{3.65}$$

We took their average as the modification for the smooth background. The limits were taken as the uncertainty bounds. About 23% of the total uncertainty of $\mathrm{Re}\,\Box_{\gamma Z}^{A}(E = 1.165\text{ GeV})$ is due to the resonance region.

3.3 $\mathrm{Re}\Box_{\gamma Z}(E)$ Results

3.3.1 Evaluation of $\mathrm{Re}\Box_{\gamma Z}^{V}(E)$

Fig. 3.7 shows $\mathrm{Re}\,\Box_{\gamma Z}^{V}$ calculated using the constituent quark model corrections to the Christy-Bosted fit. With the modified f_1 and f_2 parameters, the value at the Qweak energy is $\mathrm{Re}\,\Box_{\gamma Z}^{V}(E = 1.165\text{ GeV}) = 0.0056 \pm 0.00075$. To be conservative, the uncertainties were added directly rather than in quadrature. The figure also splits up the contributions from the resonant and nonresonant regions. At the Qweak energy, roughly 77% of the box contribution comes from the modified Christy-Bosted electromagnetic fits, 19% is from the modified Capella *et al.* fit, and the remaining 3% is from CTEQ.

It is necessary to explain why our paper [28] reports $\mathrm{Re}\,\Box_{\gamma Z}^{V}(E = 1.165\text{ GeV}) = 0.0057 \pm 0.0009$. Modified f_1 and f_2 values are not the dominant source of the discrepancy.

TABLE 3.4: The seven Christy-Bosted resonances along with their axial helicity amplitudes and corrective prefactors for proton. The neutron amplitude is calculated by exchanging $g_A^u \leftrightarrow g_A^d$.

resonance	proton axial current amplitudes	C^p_{res}
$P_{33}(1232)$	$A^{Z,A}_{1/2} \propto (g_A^u - g_A^d)\frac{4m_q\nu}{q_z^2}$	$2\frac{4m_q\nu}{q_z^2}$
$S_{11}(1535)$	$A^{Z,A}_{1/2} = -\frac{1}{\sqrt{6}}B_{10}\left(\frac{5}{3}g_A^u + \frac{1}{3}g_A^d\right)\frac{4m_q\nu}{q_z^2}$	$\frac{1}{3(2f_1+1)}\frac{16m_q\nu}{q_z^2}$
$D_{13}(1520)$	$A^{Z,A}_{1/2} = \sqrt{\frac{2}{6}}B_{10}\left(\frac{5}{3}g_A^u + \frac{1}{3}g_A^d\right)\frac{4m_q\nu}{q_z^2}$ $A^{Z,A}_{3/2} = 0$	$\frac{1-f_1}{(f_1-1)^2+3f_1^2}\frac{16m_q\nu}{q_z^2}$
$F_{15}(1680)$	$A^{Z,A}_{1/2} = \sqrt{\frac{3}{5}}B_{20}\left(\frac{4}{3}g_A^u - \frac{1}{3}g_A^d\right)\frac{4m_q\nu}{q_z^2}$ $A^{Z,A}_{3/2} = 0$	$\frac{(1-f_2)}{(1-f_2)^2+2f_2^2}\frac{20m_q\nu}{3q_z^2}$
$S_{11}(1650)$	$A^{Z,A}_{1/2} = -\sqrt{\frac{2}{27}}B_{10}\left(g_A^u + 2g_A^d\right)\frac{4m_q\nu}{q_z^2}$	$\frac{1}{3(2f_1+1)}\frac{16m_q\nu}{q_z^2}$
$P_{11}(1440)$	$A^{Z,A}_{1/2} = B_{00}\left(\frac{4}{3}g_A^u - \frac{1}{3}g_A^d\right)\frac{4m_q\nu}{q_z^2}$	$\frac{20m_q\nu}{3q_z^2}$
$F_{37}(1950)$	$A^{Z,A}_{1/2} \propto (g_A^u - g_A^d)\frac{4m_q\nu}{q_z^2}$	$2\frac{4m_q\nu}{q_z^2}$

My advisor calculated $\mathrm{Re}\,\Box^V_{\gamma Z}(E = 1.165\ \mathrm{GeV}) = 0.0058 \pm 0.00075$. We averaged our results together and increased the error bar.

Fig. 3.8 compares the predictions of various resonance modifications. Better agreement between MAID and the quark model was naively expected as the MAID fits were used to parameterize $\Lambda^2_{1,2}$. The overall smaller value for $\mathrm{Re}\,\Box^V_{\gamma Z}$ calculated by MAID is almost entirely due to the Roper resonance. For the Roper, the quark model calculates a constant corrective ratio while the MAID ratio rapidly approaches $Q_W^{p,LO}$ as Q^2 increases. The differences in the Roper resonance corrective ratios between the constituent quark model and.MAID were also the primary cause for the different deuteron asymmetry predictions in [51].

Another notable feature of Fig. 3.8 is that $\mathrm{Re}\,\Box^V_{\gamma Z}$ hardly changes when the corrective ratios are calculated using PDG photoproduction amplitudes in place of the Q^2-dependent quark model. $\mathrm{Re}\,\Box^V_{\gamma Z}$ calculated using the quark model also remains relatively unchanged when using different values for $\Lambda^2_{1,2}$ values. Both features are due to low Q^2 values dominating the integral. Indeed, an analysis of the integral indicates that the mean Q^2 value is 0.4 GeV^2. In applications with higher Q^2, such as the calculation of the deuteron asymmetry in [51], the quark model and photoproduction corrective prefactors give quite different values.

Since the Particle Data Group corrections to the resonances vary little from the constituent quark model, the bulk of the Gorchtein *et al.* model differences are due to their background modifications.

Table 3.5 displays the numerical results for the vector contribution of $\Box_{\gamma Z}$ calculated by each group. Hall *et al.* [30] recently published an updated vector calculation and argue that that Gorchtein *et al.* background uncertainty was overestimated.

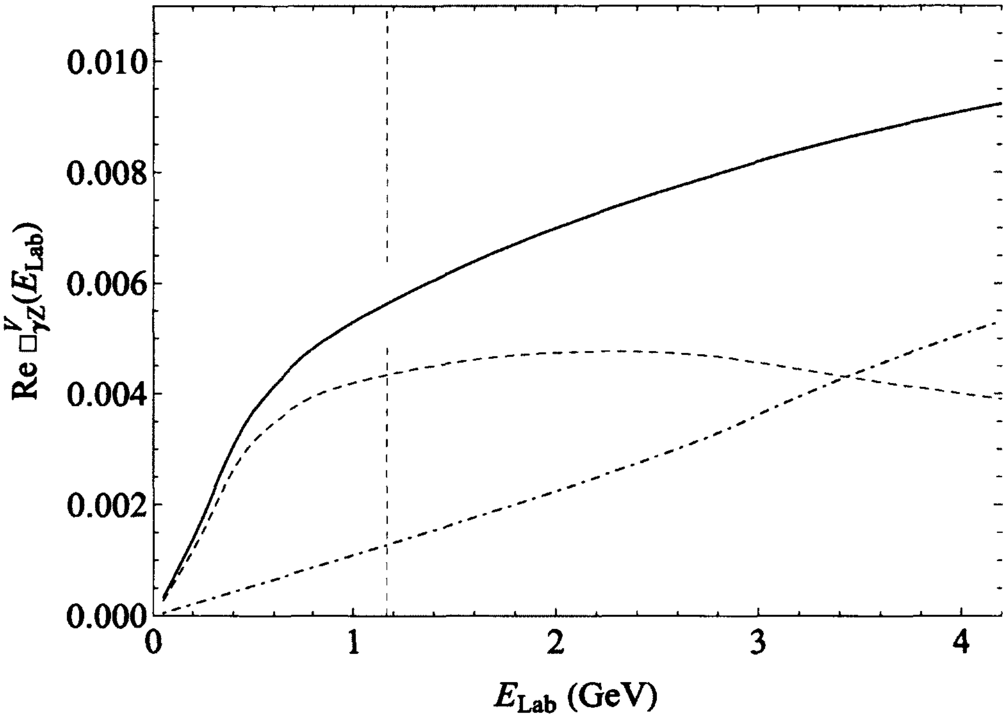

FIG. 3.7: Re $\Box^{V}_{\gamma Z}$ as a function of incoming electron energy for our constituent quark model. The black curve is the total result. The blue, dot dashed curve is the contribution from the nonresonant background while the red dashed curve is the resonant contribution. The pink band is the sum of the uncertainties from the resonant and nonresonant contributions.

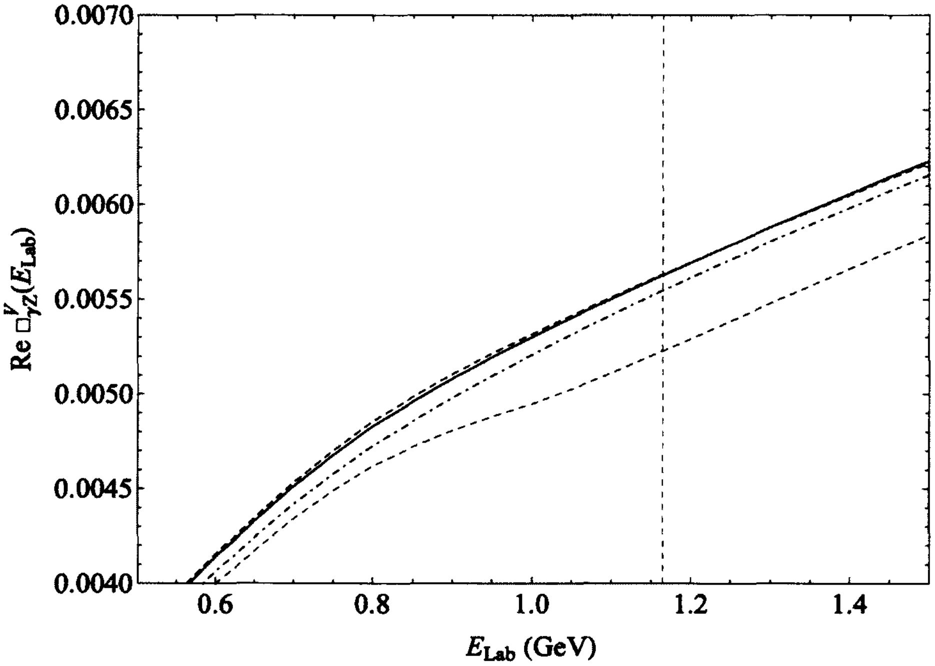

FIG. 3.8: Re $\square^V_{\gamma Z}$ as a function of incoming electron energy for different models. The black curve is the result from our previous work and uses helicity amplitudes given by the constituent quark model. The blue, dot dashed curve is the result with resonance corrections from photoproduction data of the Particle Data Group. The red dashed curve is the result when MAID helicity amplitudes are used for the resonance corrections. The green dashed curve also involves MAID helicity amplitudes, with the notable exception that the Roper correction is from our constituent quark model. Both the quark model and MAID models use the same modifications for isospin 3/2 resonances and the smooth background.

TABLE 3.5: $\mathrm{Re}\,\Box^V_{\gamma Z} \times 10^3$ evaluated at E = 1.165 GeV.

Sibirtsev *et al.* [27]	$4.7^{+1.1}_{-0.4}$
Rislow and Carlson [28]	5.7 ± 0.9
Gorchtein *et al.* [29]	5.4 ± 2.0
Hall *et al.* [30]	5.60 ± 0.36

TABLE 3.6: $\mathrm{Re}\,\Box^A_{\gamma Z} \times 10^3$ evaluated at E = 1.165 GeV.

Blunden *et al.* [31]	3.7 ± 0.4
Rislow and Carlson [33]	4.0 ± 0.5

3.3.2 Evaluation of $\mathrm{Re}\Box^A_{\gamma Z}(E)$

Fig. 3.10 displays the result for $\mathrm{Re}\,\Box^A_{\gamma Z}$. The value at the Qweak energy is $\mathrm{Re}\,\Box^V_{\gamma Z}(E = 1.165\ \mathrm{GeV}) = 0.0040 \pm 0.0005$. The uncertainties were added directly rather than in quadrature. Fig. 3.9 splits up the contributions from the resonance, elastic, and Model I regions. At the Qweak energy, roughly 90% of the box contribution comes from the scaling region, 4% is from the modified Christy Bosted fit, 4% is from Model I, and only 1% from the elastic. Fig. 3.10 displays the axial box as well as the sum of the axial and vector boxes. The uncertainties are added directly.

Table 3.6 displays the numerical results for the axial contribution of $\Box_{\gamma Z}$ calculated by each group. There is much better agreement for the axial box because its evaluation is less sensitive to resonance region structure function models.

To one loop order, $Q^p_W \approx 0.07$. A 4% measurement of this value has an error budget of about 0.0028. Our constituent quark model yields the total

$$\mathrm{Re}\,\Box_{\gamma Z}(E = 1.165\ \mathrm{GeV})|_{\mathrm{total}} = (9.5 \pm 1.3) \times 10^{-3}. \qquad (3.66)$$

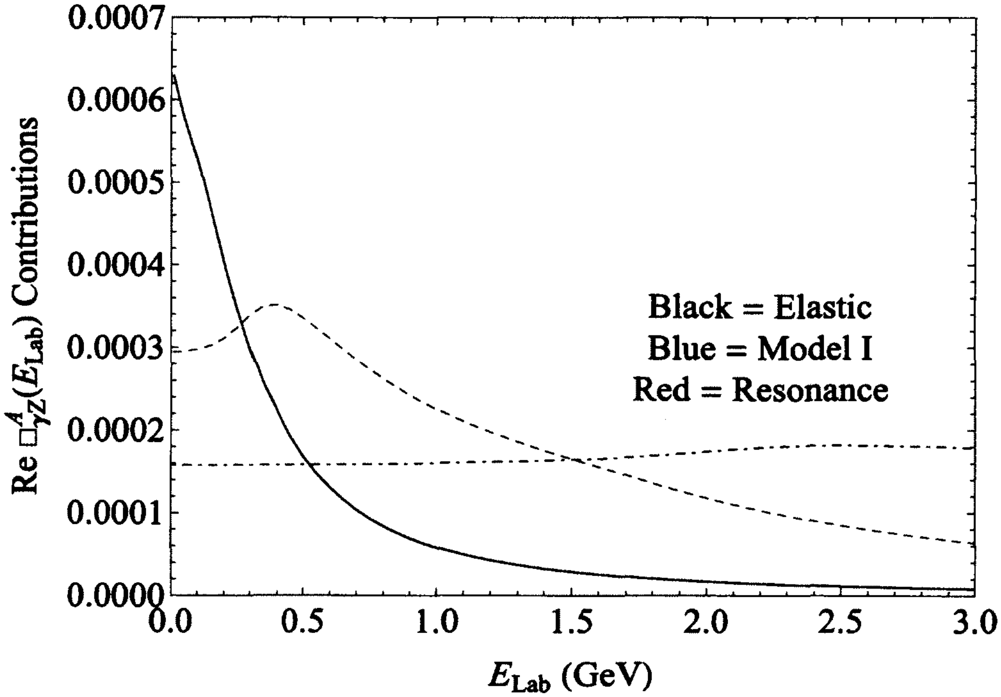

FIG. 3.9: Elastic (blue), resonance (red dashed), and model I (black dot dashed) contributions to the axial box.

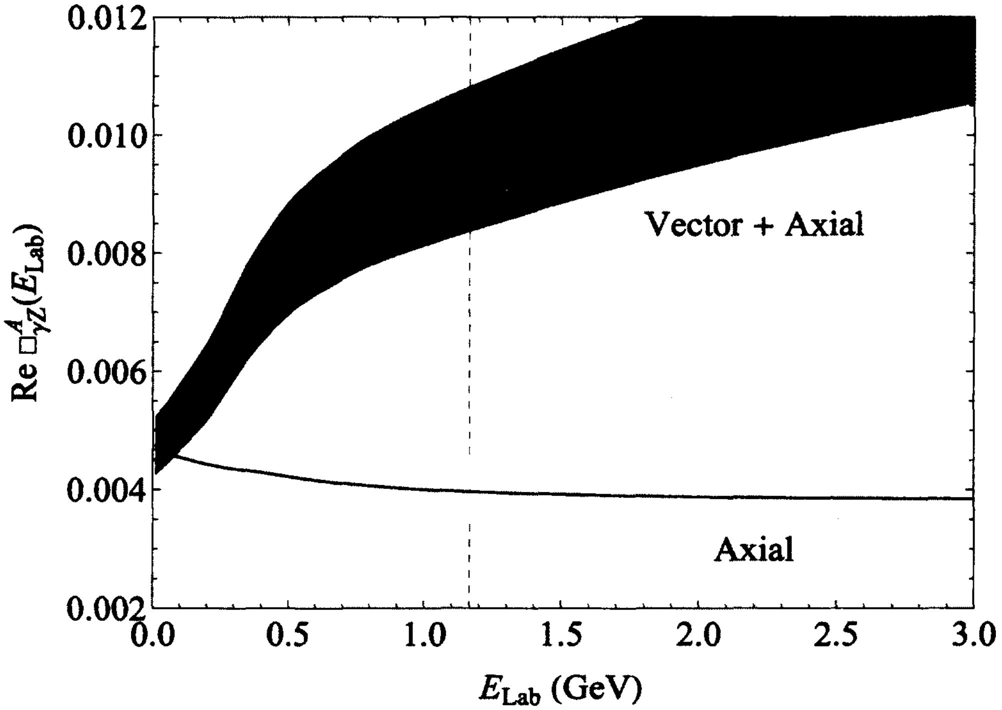

FIG. 3.10: The axial box. We also add the axial and vector boxes to obtain the total box.

At 0.0013, the direct sum of the uncertainties for our axial and vector boxes respects the allotted error budget.

The total γZ box value from Blunden *et al.* [31] is

$$\mathrm{Re}\,\Box_{\gamma Z}(E = 1.165\ \mathrm{GeV})|_{\mathrm{total}} = (8.4^{+1.1}_{-0.6}) \times 10^{-3}. \tag{3.67}$$

These two calculations are in agreement within uncertainties. Each calculation also has error bounds below the error budget of the Qweak experiment.

The question remains which calculations the Qweak collaboration should use in their analysis. The disagreement between the various calculations is largely due to the treatment of the γZ structure functions in the resonance region. We believe the collaboration will be equally well-served by either $\mathrm{Re}\,\Box^{A}_{\gamma Z}$ calculation. $\mathrm{Re}\,\Box^{A}_{\gamma Z}$ is not very sensitive to the resonance region modifications since its integrals get much of their support from high Q^2. $F_3^{\gamma Z}$ in the scaling region can be constructed using fits to parton distribution data.

Which $\mathrm{Re}\,\Box^{V}_{\gamma Z}$ calculation to use is more open to debate. The vector integrals receive much of their support from the resonance region and are thus sensitive to the modification $F_{1,2}^{\gamma\gamma} \to F_{1,2}^{\gamma Z}$. In Sec. 3.2.2 we showed that there is little difference between modifying the Christy-Bosted resonance fits using our constituent quark model [28] or photoproduction amplitudes from the Particle Data Group (as in [29]). Differences arise between [28] and [29] because of the treatments of the resonance region background. We continue modifying the Christy-Bosted background fit while Gorchtein *et al.* modify two GVD fits to low Q^2, high W^2 data and extrapolate them down to the resonance region. We believe our modification is more satsifactory since it does not involve any extrapolations. We cannot comment on the vector calculation of [27] since they provide few details of their model. It is our understanding that they are currently working on improving their calculation.

Without constraints from experimental data, it is impossible to make a definitive statement on which γZ structure function model is the most valid. All of the various fits give very similar results for the Qweak kinematics. A question remains of the models' robustness at different kinematics. Do the γZ structure function models yield similar predictions for different experimental conditions? This question will be addressed in the next chapter.

CHAPTER 4

Experimental Determination of $F_{1,2,3}^{\gamma Z}(x, Q^2)$

It is hoped that one day the models for $F_{1,2,3}^{\gamma Z}(x, Q^2)$ can be replaced in favor of fits to experimental data (I also share this hope despite the fact such fits will nullify much of my graduate research). The present data are insufficient to construct fits, but can be used as a first test of the robustness of competing $F_{1,2,3}^{\gamma Z}(x, Q^2)$ models at kinematics different than the Qweak experiment. In this chapter we present the model predictions for two present experiments. In Sec. 4.1 we derive and calculate the asymmetry for the PVDIS experiment at Jefferson Lab [4]. In Sec. 4.2 we calculate the asymmetry for the final days of the Qweak experimental run. During the last days of Qweak the electron beam kinematics were changed to test the competing $F_{1,2,3}^{\gamma Z}(x, Q^2)$ models.

4.1 PVDIS Test of $F^{\gamma Z}_{1,2,3}(x, Q^2)$

The PVDIS experiment at JLAB [4] measured the parity-violating asymmetry of electron scattering off a deuteron target. The kinematics were chosen to probe $2C_{2u} - C_{2d}$. At tree level these parameters are defined as

$$\begin{aligned} C_{1u} &= 2g^e_A g^u_V = -\frac{1}{2} + \frac{4}{3}\sin^2\theta_W \\ C_{1d} &= 2g^e_A g^d_V = \frac{1}{2} - \frac{2}{3}\sin^2\theta_W \\ C_{2u} &= 2g^e_V g^u_A = -\frac{1}{2} + 2\sin^2\theta_W \\ C_{2d} &= 2g^2_V g^d_A = \frac{1}{2} - 2\sin^2\theta_W. \end{aligned} \tag{4.1}$$

The PVDIS proposal [4] stated that two kinematics would be examined: $Q^2 = 1.1$ and 1.9 GeV^2 at $x \approx 0.3$. We were particularly interested in this experiment since a) the asymmetry can also be expressed as a sum of $F^{\gamma Z}_{1,2,3}(x, Q^2)$ and b) the kinematics would allow a first test of the validity of the different $F^{\gamma Z}_{1,2,3}(x, Q^2)$ models in the resonance region.

4.1.1 Derivation of PVDIS Asymmetry

The equation for the scattering asymmetry is

$$A_{PVDIS} \equiv \frac{\sigma_R - \sigma_L}{\sigma_R + \sigma_L} \tag{4.2}$$

where once again $\sigma_{L(R)}$ is the cross section for left (right) polarized electrons (for reasons unknown, publications for PVDIS and Qweak tend to choose opposite sign conventions for their asymmetries). Since σ is proportional to the modulus squared of the amplitude, the dominant terms of the tree level asymmetry can be rewritten as

$$A_{PVDIS} = \frac{(\mathcal{M}_\gamma^\dagger \mathcal{M}_Z + \mathcal{M}_\gamma \mathcal{M}_Z^\dagger)|_{\lambda=1/2} - (\mathcal{M}_\gamma^\dagger \mathcal{M}_Z + \mathcal{M}_\gamma \mathcal{M}_Z^\dagger)|_{\lambda=-1/2}}{2|\mathcal{M}_\gamma|^2}. \tag{4.3}$$

In Chap. 3, we proceeded to evaluate the tree level asymmetry by canceling a factor of $\mathcal{M}_\gamma$. For this application we are interested in the off-diagonal structure functions at tree level and we will analyze the numerator and denominator as expressed in Eq. (4.3).

To evaluate the numerator we return to our γZ box analysis. Our study of the γZ box began with the optical theorem. Removing the integral and factor of 1/2 from Eq. (3.3) returns the numerator multiplied by a δ-function,

$$\begin{aligned}(\mathcal{M}_\gamma^\dagger \mathcal{M}_Z + \mathcal{M}_\gamma \mathcal{M}_Z^\dagger)(2\pi)^4\delta^4(k+p-k_1-p') &= \left(-\frac{2}{\sqrt{2}}G_F\right) 4\pi\alpha \frac{1}{Q^2\left(\frac{Q^2}{M_Z^2}+1\right)} \\ &\quad \times 8\pi(g_V^e - (2\lambda)g_A^e)Q^2\Bigg\{[F_1^{\gamma Z}(x,Q^2) \\ &\quad + AF_2^{\gamma Z}(x,Q^2) - (2\lambda)BF_3^{\gamma Z}(x,Q^2)\Bigg\}. \end{aligned} \tag{4.4}$$

where $A = \frac{2p\cdot k_1 p\cdot k}{Q^2 p\cdot q} - \frac{p^2}{2p\cdot q}$, $B = \frac{p\cdot k + p\cdot k_1}{2p\cdot q}$, and k_1 is the final momentum of the electron. Performing the substitutions $x = Q^2/(2p\cdot q)$ and $y = p\cdot q/p\cdot k$ the above expression becomes

$$\begin{aligned}(\mathcal{M}_\gamma^\dagger \mathcal{M}_Z + \mathcal{M}_\gamma \mathcal{M}_Z^\dagger)(2\pi)^4\delta^4(k+p-k_1-p') &= \left(-\frac{2}{\sqrt{2}}G_F\right) 4\pi\alpha \frac{1}{Q^2\left(\frac{Q^2}{M_Z^2}+1\right)} \\ &\quad \times 8\pi(g_V^e - (2\lambda)g_A^e)\Bigg\{Q^2F_1^{\gamma Z}(x,Q^2) \\ &\quad + \left(\frac{Q^2}{xy^2} - \frac{Q^2}{xy} - M^2x\right)F_2^{\gamma Z}(x,Q^2) \\ &\quad - (2\lambda)\left(\frac{1}{y} - \frac{1}{2}\right)Q^2F_3^{\gamma Z}(x,Q^2)\Bigg\}. \end{aligned} \tag{4.5}$$

To account for the introduction of a δ-function in the numerator of Eq. (4.3) we also multiply the denominator by the same,

$$\begin{aligned}
|\mathcal{M}_\gamma|^2(2\pi)^4\delta^4(k+p-k_1-p') &= \frac{(4\pi\alpha)^2}{Q^4} \\
&\times (k_1^\mu k^\nu + k_1^\nu k^\mu - k_1 \cdot k g^{\mu\nu} - i(2\lambda)\epsilon^{\mu\nu\alpha\beta}k_\alpha k_{1\beta}) \\
&\times 4\pi\Bigg[\left(-g_{\mu\nu} + \frac{q_\mu q_\nu}{q^2}\right) F_1^{\gamma\gamma}(x,Q^2) + \frac{p_\mu p_\nu}{p\cdot q} F_2^{\gamma\gamma}(x,Q^2) \\
&- i\epsilon_{\mu\nu\sigma\tau}\frac{q^\sigma p^\tau}{2p\cdot q}F_3^{\gamma\gamma}(x,Q^2)\Bigg] \\
&= 8\pi\frac{(4\pi\alpha)^2}{Q^4} \\
&\times \left[Q^2 F_1^{\gamma\gamma}(x,Q^2) + \left(\frac{Q^2}{xy^2} - \frac{Q^2}{xy} - M^2 x\right) F_2^{\gamma\gamma}(x,Q^2)\right].
\end{aligned} \tag{4.6}$$

Substituting Eqs.(4.5) and (4.6) into Eq. (4.3) gives

$$\begin{aligned}
A_{PVDIS} &= \frac{G_F M_Z^2}{2\sqrt{2}\pi\alpha}\frac{Q^2}{Q^2+M_Z^2}g_A^e \\
&\times \frac{xy^2 F_1^{\gamma Z}(x,Q^2) + \left(1 - y - \frac{M^2x^2y^2}{Q^2}\right)F_2^{\gamma Z}(x,Q^2) + \frac{g_V^e}{g_A^e}\left(y - \frac{y^2}{2}\right)xF_3^{\gamma Z}(x,Q^2)}{xy^2 F_1^{\gamma\gamma}(x,Q^2) + \left(1 - y - \frac{M^2x^2y^2}{Q^2}\right)F_2^{\gamma\gamma}(x,Q^2)}.
\end{aligned} \tag{4.7}$$

The above expression indicates that the PVDIS asymmetry can be used as a first test of the validity of off-diagonal structure function models. Note that for the PVDIS kinematics, the third term multiplying $F_2^{\gamma Z}$ is small.

To complete the derivation of primary interest to the experimentalists, the structure functions are rewritten in terms of parton distribution functions. For large x,

$$
\begin{aligned}
F_1^{\gamma Z} = \frac{1}{2x} F_2^{\gamma Z} &= \sum_q e_q g_V^q (q + \bar{q}), \\
F_1^{\gamma\gamma} = \frac{1}{2x} F_2^{\gamma\gamma} &= \frac{1}{2} \sum_q e_q^2 (q + \bar{q}), \\
F_3^{\gamma Z} &= \sum_q 2 e_q g_A^q (q - \bar{q}).
\end{aligned} \tag{4.8}
$$

where q ($\bar{q}$) are quark (antiquark) parton distributions for the proton. For the neutron, $u_n = d$ and $d_n = u$.

In the light quark limit, the off-diagonal structure functions for the deuteron are

$$
\begin{aligned}
F_1^{\gamma Z} = \frac{1}{2x} F_2^{\gamma Z} &= \frac{2}{3} g_V^u (u + \bar{u}) - \frac{1}{3} g_V^d (d + \bar{d}) - \frac{1}{3} g_V^s (s + \bar{s}) \\
&\quad + \frac{2}{3} g_V^u (d + \bar{d}) - \frac{1}{3} g_V^d (u + \bar{u}) - \frac{1}{3} g_V^s (s + \bar{s}), \\
F_1^{\gamma\gamma} = \frac{1}{2x} F_2^{\gamma\gamma} &= \frac{1}{2} \left[\frac{4}{9} (u + \bar{u}) + \frac{1}{9} (d + \bar{d}) + \frac{1}{9} (s + \bar{s}) \right. \\
&\quad \left. + \frac{4}{9} (d + \bar{d}) + \frac{1}{9} (u + \bar{u}) + \frac{1}{9} (s + \bar{s}) \right], \\
F_3^{\gamma Z} &= 2 \left[\frac{2}{3} g_A^u (u - \bar{u}) - \frac{1}{3} g_A^d (d - \bar{d}) \right].
\end{aligned} \tag{4.9}
$$

Substituting for the off-diagonal structure functions and dropping the third prefactor of $F_2^{\gamma Z}$, Eq. (4.7) becomes

$$
\begin{aligned}
A_{PVDIS} = {} & \frac{G_F M_Z^2}{2\sqrt{2}\pi\alpha} \frac{Q^2}{Q^2 + M_Z^2} \frac{1}{\frac{x}{2}(1 + (1-y)^2) \left[\frac{5}{9}(u + \bar{u} + d + \bar{d}) + \frac{2}{9}(s + \bar{s}) \right]} \\
& \times g_A^e x \left\{ (1 + (1-y)^2) \left[\left(\frac{2}{3} g_V^u - \frac{1}{3} g_V^d \right) (u + \bar{u} + d + \bar{d}) - \frac{2}{3} g_V^s (s - \bar{s}) \right] \right. \\
& \left. + \frac{g_V^e}{g_A^e} (1 - (1-y)^2) \left(\frac{2}{3} g_A^u - \frac{1}{3} g_A^d \right) (u_v + d_v) \right\},
\end{aligned} \tag{4.10}
$$

where the subscript "v" indicates the distribution of valence quarks.

Defining,

$$\begin{aligned} Y &= \frac{1-(1-y)^2}{1+(1-y)^2}, \\ R_s &= \frac{2(s+\bar{s})}{u+\bar{u}+d+\bar{d}}, \\ R_v &= \frac{u_v+d_v}{u+\bar{u}+d+\bar{d}}, \end{aligned} \tag{4.11}$$

and substituting $C_{1,2}$ parameters into Eq. (4.10) yields

$$\begin{aligned} A_{PVDIS} = {} & 3\frac{G_F M_Z^2}{2\sqrt{2}\pi\alpha}\frac{Q^2}{Q^2+M_Z^2} \\ & \times \frac{2C_{1u}-C_{1d}(1+R_s)+Y(2C_{2u}-C_{2d})R_v}{5+R_s}. \end{aligned} \tag{4.12}$$

4.1.2 Asymmetry Predictions from different γZ Structure Function Models

In our paper [51] we calculated the PVDIS asymmetry based on the kinematics in the experimental proposal [4]. Since our structure function models for the Qweak experiment were for protons, we made predictions for both the PVDIS experiment and a hypothetical proton scattering experiment with identical kinematics.

In fact, the PVDIS experiment took data at four kinematics [52]. The measurements were published a year after our paper. We present both our paper's results and new predictions for the actual PVDIS measurements. Our paper's results are still revelant because they demonstrate how the structure function models evolve as a function of W.

As previously discussed, all models for the proton's $F_{1,2,3}^{\gamma Z}(x,Q^2)$ in the resonance region are rooted in the Christy-Bosted fit to electromagnetic data [39]. We chose to modify their fit using amplitudes constructed by the constituent quark model. Alternatively, these amplitudes could be constructed using fits from MAID [34]. Gorchtein *et al.* [29] used photoproduction data from the Particle Data Group [2].

Fig. 4.1 displays the proton asymmetry predictions of the various $F^{\gamma Z}_{1,2,3}(x, Q^2)$ models. Uncertainties were estimated for the constituent quark and MAID models following the error discussion of Chap. 3. The pink band indicates the uncertainty due to the resonances of the Christy-Bosted fit. The gray band indicates the uncertainty due to the background modifications.

We do not estimate the uncertainty in the two models of Gorchtein *et al.* They averaged their two models together and used them as extrema for their uncertainty estimate.

One thing to note in the MAID fit is that much of the disagreement with the constituent quark model lies with the Roper fit. Fig. 4.2 shows the MAID fit for all resonances except the Roper. The Roper modification in this case is due to the constituent quark model. With this change the MAID and constituent quark model predictions are in better agreement.

The reason for the Roper discrepancy is the modifications' behavior as a function of Q^2. The MAID modification for the Roper resonance features a sign change in the helicity amplitude at around $Q^2 = 2/3$ GeV^2. As it happens, the constituent quark model modification to the Roper resonance is Q^2 independent.

Bosted and Christy also have fits for electromagnetic deuteron data [53]. This fit contains contributions from the same resonances as their proton fit. As with the proton, we sought a corrective factor,

$$F_1^{\gamma Z}|_d = \sum_{res} C_{res} \times F_1^{\gamma\gamma}|_{d,res} \tag{4.13}$$

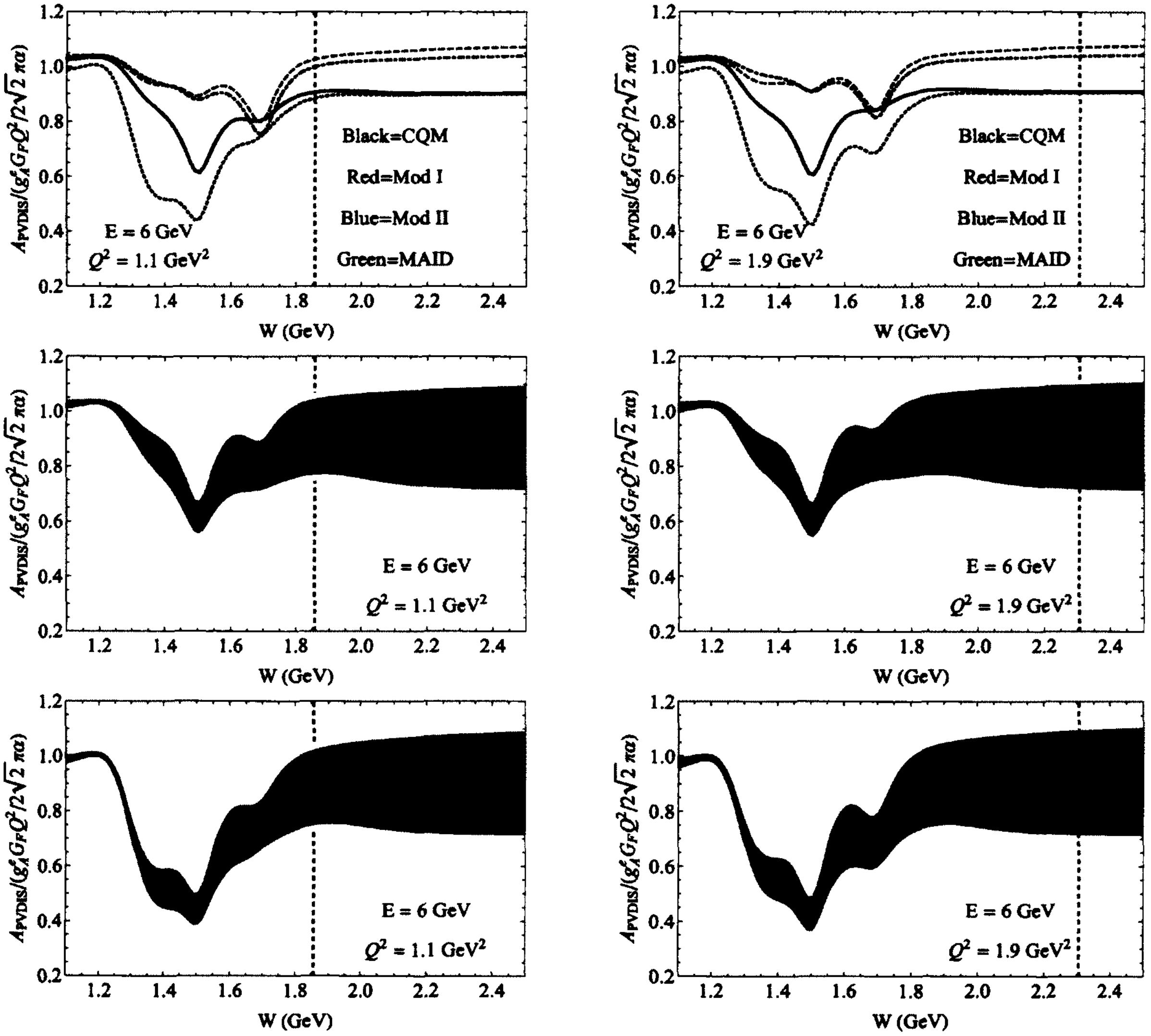

FIG. 4.1: Normalized proton asymmetry for $Q^2 = 1.1$ GeV^2 and 1.9 GeV^2 as a function of W. The top panel displays the predictions from several different off-diagonal structure function models. The solid line indicates the prediction of a constituent quark modification to the Christy-Bosted electromagnetic fits. The red, dashed and blue, dot-dashed curves are models used by Gorchtein *et al.* The green, dotted curve is the modification of the Christy-Bosted fits using MAID resonance helicity amplitudes. The middle and bottom panels are the constituent quark model and MAID fits, respectively, with uncertainty limits. The gray band is the uncertainty due to the nonresonance background while the pink band includes the resonance contributions. The dashed vertical lines indicate the kinematic points for the 6 GeV PVDIS (deuteron) experiment; each corresponds to $x \approx 0.3$.

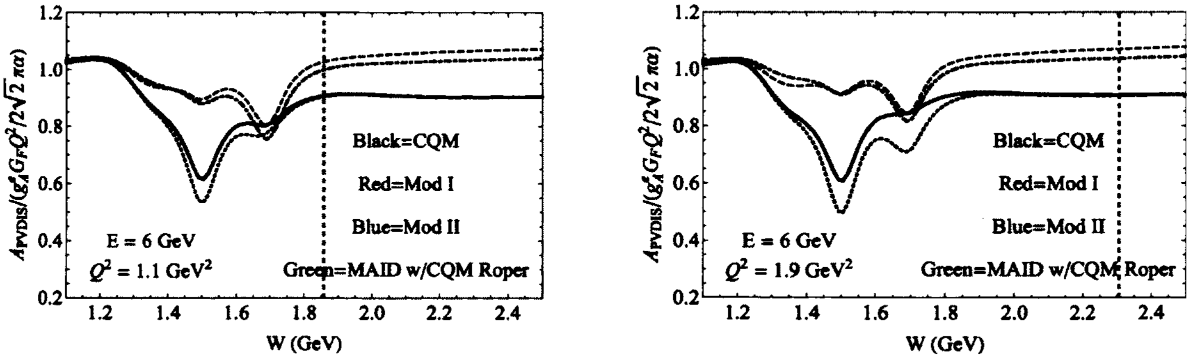

FIG. 4.2: Normalized proton asymmetry for $Q^2 = 1.1$ GeV^2 and 1.9 GeV^2 as a function of W. The solid line indicates the prediction of a constituent quark modification to the Christy-Bosted electromagnetic fits. The red, dashed and blue, dot-dashed curves are models used by Gorchtein *et al.* The green, dotted curve is the modification of the Christy-Bosted fits using MAID resonance helicity amplitudes with the exception of the Roper resonance. For the Roper, the constituent quark model was used. The dashed vertical lines indicate the kinematic points for the 6 GeV PVDIS (deuteron) experiment; each corresponds to $x \approx 0.3$.

such that

$$\begin{aligned} C_{res} &= \left.\frac{F_1^{\gamma Z,p} + F_1^{\gamma Z,n}}{F_1^{\gamma\gamma,p} + F_1^{\gamma\gamma,n}}\right|_{res} \\ &= 2\frac{\sum_\lambda A_\lambda^{\gamma,p} A_\lambda^{Z,p} + \sum_\lambda A_\lambda^{\gamma,n} A_\lambda^{Z,n}}{\sum_\lambda (A_\lambda^{\gamma,p})^2 + \sum_\lambda (A_\lambda^{\gamma,n})^2}, \end{aligned} \tag{4.14}$$

where superscripts "p" and "n" indicate proton and neutron amplitudes, respectively. Table 4.1 shows the amplitudes associated with $n\gamma \to N_n^*$ transitions and the corrective prefactor for each resonance.

The transition amplitudes can also be found using amplitudes from MAID or photoproduction fits from PDG. We already showed how an isospin rotation produces

$$\langle N_p^* | J_\mu^{Z,V} | p \rangle = \frac{1}{2}(1 - 4\sin^2\theta_W(0))\langle N_p^* | J_\mu^\gamma | p \rangle - \frac{1}{2}\langle N_n^* | J_\mu^\gamma | n \rangle. \tag{4.15}$$

A parallel algebraic analysis of neutron amplitudes gives

$$\langle N_n^*|J_\mu^{Z,V}|n\rangle = \frac{1}{2}(1-4\sin^2\theta_W(0))\langle N_n^*|J_\mu^\gamma|n\rangle - \frac{1}{2}\langle N_p^*|J_\mu^\gamma|p\rangle. \tag{4.16}$$

C_{res} can also be written as

$$C_{res} = Q_W^{p,LO} - 2\frac{\sum_\lambda A_\lambda^{\gamma,p}A_\lambda^{\gamma,n}}{\sum_\lambda (A_\lambda^{\gamma,p})^2 + \sum_\lambda (A_\lambda^{\gamma,n})^2}. \tag{4.17}$$

We also calculated $F_3^{\gamma Z}$ for the deuteron in [51]. The corrective ratios for the deuteron resonances are listed in Table 4.2. Following the above analysis for the proton background, the limits to the deuteron background are 0 and 18/5. We used these limits as uncertainty bounds and their average as the actual background.

Fig. 4.3 shows the comparison of different modifications to the Bosted-Christy fit. With the uncertainties, the different models cannot be resolved.

As for the proton fits, the MAID Roper modification is the main source of disagreement with the constituent quark model. Fig. 4.4 shows the model comparisons when the constituent quark model Roper is substituted in the MAID fit.

The actual PVDIS data can help us determine which Roper modification is more valid. Table 4.3 presents the measured asymmetries at the four kinematic points compared to the predictions of the constituent quark model, MAID, and Gorchtein *et al.* modifications. At $W = 1.263$ GeV, MAID is the only modification that agrees with the measured asymmetry. This agreement suggests the MAID Roper modification is better at low W. However, at $W = 1.591$ MAID significantly underestimates the asymmetry whereas the other two models agree with the measurement.

TABLE 4.1: The seven Christy-Bosted resonances along with their electromagnetic helicity amplitudes along and corresponding corrective ratios for the deuteron. The ($pZ \rightarrow N_p^*$) helicity amplitudes are calculated by substituting $e_q \rightarrow g_q^v = T_q^3 - 2e_q\sin^2\theta_W(0)$. The ($n\gamma \rightarrow N_n^*$) and ($nZ \rightarrow N_n^*$) helicity amplitudes are calculated by exchanging $e_u \leftrightarrow e_d$ and $g_u^v \leftrightarrow g_d^v$, respectively, in the proton analysis.

resonance	neutron electroproduction amplitudes	C^d_{res}
$P_{33}(1232)$	$A^{\gamma}_{1/2} \propto (e_d - e_u)$	$1 + Q_W^{p,LO}$
$S_{11}(1535)$	$A^{\gamma}_{1/2} = \frac{1}{\sqrt{6}}\big(\sqrt{2}A_{10}(e_d - e_u)$ $-B_{10}(\frac{5}{3}e_d + \frac{1}{3}e_u)\big)$	$2\frac{(1+2f_1)(1/3+2f_1)}{(1+2f_1)^2+(1/3+2f_1)^2} + Q_W^{p,LO}$
$D_{13}(1520)$	$A^{\gamma}_{1/2} = \frac{1}{\sqrt{6}}\big(A_{10}(e_d - e_u)$ $+\sqrt{2}B_{10}(\frac{5}{3}e_d + \frac{1}{3}e_u)\big)$ $A^{\gamma}_{3/2} = \frac{1}{\sqrt{2}}A_{10}\,(e_d - e_u)$	$\frac{2(1-f_1)(1/3-f_1)+6f_1^2}{(1-f_1)^2+(1/3-f_1)^2+6f_1^2} + Q_W^{p,LO}$
$F_{15}(1680)$	$A^{\gamma}_{1/2} = \sqrt{\frac{2}{5}}A_{20}(2e_d + e_u)$ $+\sqrt{\frac{3}{5}}B_{20}(\frac{4}{3}e_d - \frac{1}{3}e_u)$ $A^{\gamma}_{3/2} = \frac{2}{\sqrt{5}}A_{20}\,(2e_d + e_u)$	$4\frac{1-f_2}{3(1-f_2)^2+6f_2^2+4/3} + Q_W^{p,LO}$
$S_{11}(1650)$	$A^{\gamma}_{1/2} = -\sqrt{\frac{2}{27}}B_{10}\,(e_d + 2e_u)$	$2\frac{(1+2f_1)(1/3+2f_1)}{(1+2f_1)^2+(1/3+2f_1)^2} + Q_W^{p,LO}$
$P_{11}(1440)$	$A^{\gamma}_{1/2} = B_{00}\,(\frac{4}{3}e_d - \frac{1}{3}e_u)$	$12/13 + Q_W^{p,LO}$
$F_{37}(1950)$	$A^{\gamma}_{1/2} \propto (e_d - e_u)$	$1 + Q_W^{p,LO}$

TABLE 4.2: The seven Christy-Bosted resonances along with their axial helicity amplitudes and corrective coefficients for the deuteron. The neutron amplitude is calculated by exchanging $g_A^u \leftrightarrow g_A^d$ in the proton amplitude.

resonance	neutron axial current amplitudes	C^d_{res}
$P_{33}(1232)$	$A^{Z,A}_{1/2} \propto (g_A^d - g_A^u)\frac{4m_q\nu}{q_z^2}$	$2\frac{4m_q\nu}{q_z^2}$
$S_{11}(1535)$	$A^{Z,A}_{1/2} = -\frac{1}{\sqrt{6}}B_{10}\left(\frac{5}{3}g_A^d + \frac{1}{3}g_A^u\right)\frac{4m_q\nu}{q_z^2}$	$\frac{(1+2f_1)+(1/3+2f_1)}{(1+2f_1)^2+(1/3+2f_1)^2}\frac{16m_q\nu}{3q_z^2}$
$D_{13}(1520)$	$A^{Z,A}_{1/2} = \sqrt{\frac{2}{6}}B_{10}\left(\frac{5}{3}g_A^d + \frac{1}{3}g_A^u\right)\frac{4m_q\nu}{q_z^2}$ $A^{Z,A}_{3/2} = 0$	$\frac{(1-f_1)-(f_1-1/3)}{(1-f_1)^2+(f_1-1/3)^2+6f_1^1}\frac{16m_q\nu}{3q_z^2}$
$F_{15}(1680)$	$A^{Z,A}_{1/2} = \sqrt{\frac{3}{5}}B_{20}\left(\frac{4}{3}g_A^d - \frac{1}{3}g_A^u\right)\frac{4m_q\nu}{q_z^2}$ $A^{Z,A}_{3/2} = 0$	$\frac{(1-f_2)+2/3}{(1-f_2)^2+2f_2^2+4/9}\frac{20m_q\nu}{3q_z^2}$
$S_{11}(1650)$	$A^{\gamma}_{1/2} = -\sqrt{\frac{2}{27}}B_{10}\left(g_A^d + 2g_A^u\right)\frac{4m_q\nu}{q_z^2}$	$\frac{(1+2f_1)+(1/3+2f_1)}{(1+2f_1)^2+(1/3+2f_1)^2}\frac{16m_q\nu}{3q_z^2}$
$P_{11}(1440)$	$A^{Z,A}_{1/2} = B_{00}\left(\frac{4}{3}g_A^d - \frac{1}{3}g_A^u\right)\frac{4m_q\nu}{q_z^2}$	$\frac{100m_q\nu}{13q_z^2}$
$F_{37}(1950)$	$A^{Z,A}_{1/2} \propto (g_A^d - g_A^u)\frac{4m_q\nu}{q_z^2}$	$2\frac{4m_q\nu}{q_z^2}$

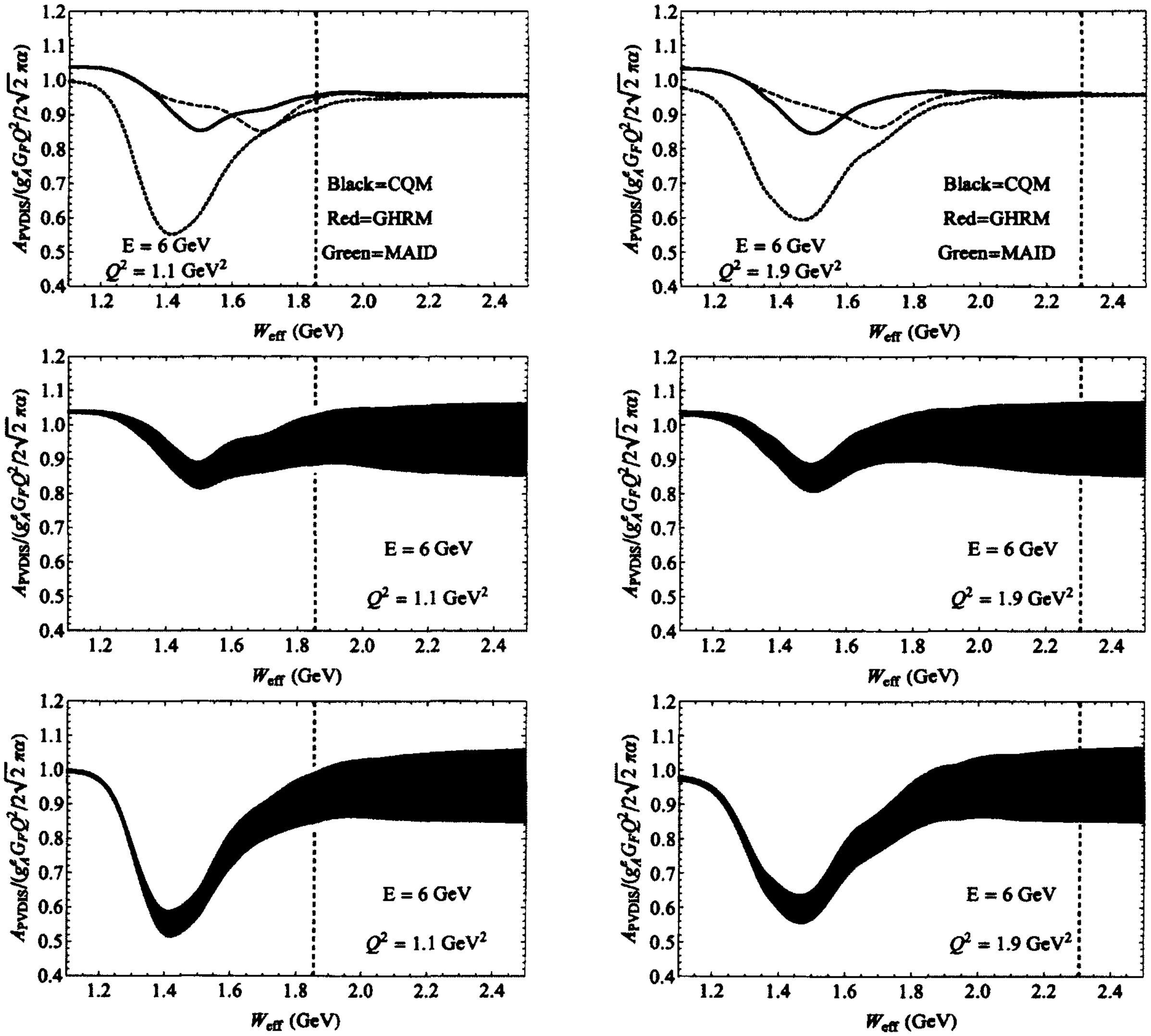

FIG. 4.3: Deuteron asymmetry for $Q^2 = 1.1$ GeV^2 and 1.9 GeV^2 as a function of W_{eff}, where $W_{\text{eff}}^2 = M^2 + 2M\nu - Q^2$. The top panel displays the predictions from several different off-diagonal structure function models. The solid line indicates the prediction of a constituent quark modification to the Christy-Bosted electromagnetic fits. The red, dashed and blue, dot-dashed curves are models used by Gorchtein *et al.* The green, dotted curve is the modification of the Christy-Bosted fits using MAID resonance helicity amplitudes. The middle and bottom panels are the constituent quark model and MAID fits, respectively, with uncertainty limits. The gray band is the uncertainty due to the nonresonance background while the pink band includes the resonance contributions. The dashed vertical lines again indicate the kinematic points for the 6 GeV PVDIS experiment; each corresponds to $x \approx 0.3$.

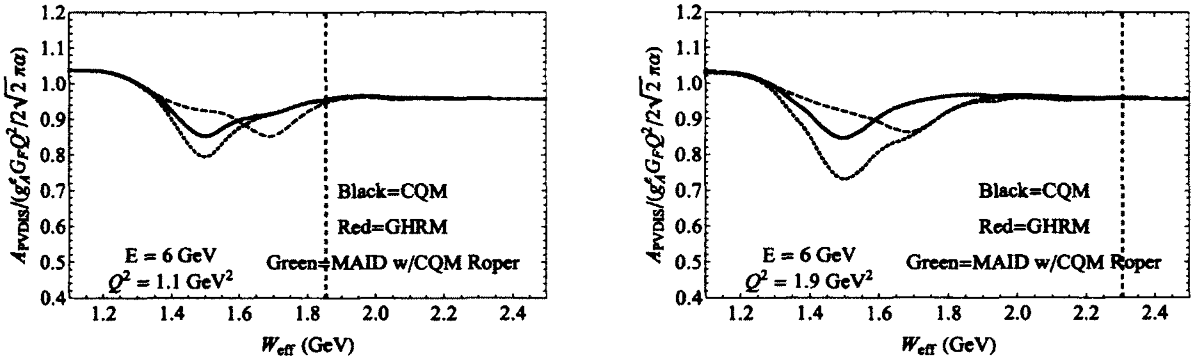

FIG. 4.4: Normalized proton asymmetry for $Q^2 = 1.1$ GeV^2 and 1.9 GeV^2 as a function of W. The solid line indicates the prediction of a constituent quark modification to the Christy-Bosted electromagnetic fits. The red, dashed and blue, dot-dashed curves are models used by Gorchtein *et al.* The green, dotted curve is the modification of the Christy-Bosted fits using MAID resonance helicity amplitudes with the exception of the Roper resonance. For the Roper, the constituent quark model was used. The dashed vertical lines indicate the kinematic points for the 6 GeV PVDIS (deuteron) experiment; each corresponds to $x \approx 0.3$.

TABLE 4.3: The measured and predicted PVDIS asymmetry.

PVDIS kinematics	I	II	III	IV
E (GeV)	4.867	4.867	4.867	6.067
Q^2 (GeV^2)	0.950	0.831	0.757	1.472
W_{eff} (GeV)	1.263	1.591	1.857	1.981
A_{PVDIS} (ppm)				
Measured	−68.97 ±9.09	−74.12 ±7.43	−61.80 ±5.50	−119.56 ±18.42
CQM	−87.4 ±8.9	−67.1 ±7.0	−64.9 ±6.8	−128.1 ±13.3
MAID	−75.2 ±7.7	−56.9 ±6.1	−63.2 ±6.5	−125.5 ±13.0
GHRM	−87.3	−67.6	−64.6	−127.6

4.2 Qweak Test of $F_{1,2,3}^{\gamma Z}(x, Q^2)$

Our comparison of $F_{1,2,3}^{\gamma Z}$ model predictions for the PVDIS experiment [51] helped motivate a look at different kinematics at the end of the Qweak run. During the final days of data taking, the kinematics were changed from $Q^2 = 0.028$ to $Q^2 = 0.09$ GeV^2 and $E = 1.165$ to $E = 3.35$ GeV in an attempt to constrain the different structure function models.

Fig. 4.5 displays the predictions of the different models. At these kinematics it will be difficult to resolve the different models. The region with the largest model discrepancies is unfortunately not probed.

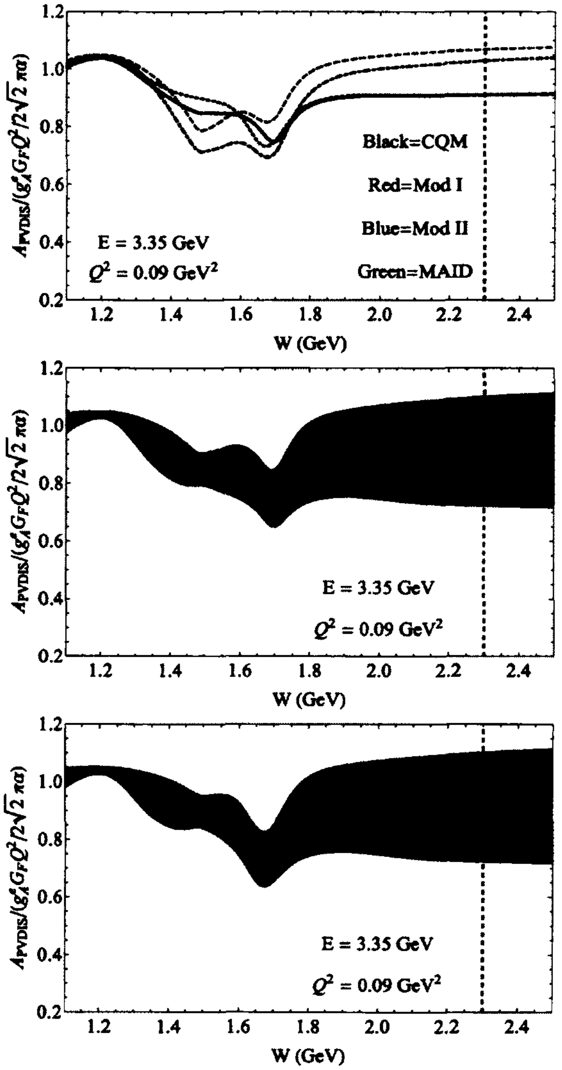

FIG. 4.5: Proton asymmetry for the final days of the Qweak run as a function of W. The kinematics were changed from $Q^2 = 0.028$ to $Q^2 = 0.09$ GeV^2 and $E = 1.165$ to $E = 3.35$ GeV. The top panel displays the predictions from several different off-diagonal structure function models. The solid line indicates the prediction of a constituent quark modification to the Christy-Bosted electromagnetic fits. The red, dashed and blue, dot-dashed curves are models used by Gorchtein *et al.* The green, dotted curve is the modification of the Christy-Bosted fits using MAID resonance helicity amplitudes. The middle and bottom panels are the constituent quark model and MAID fits, respectively, with uncertainty limits. The gray band is the uncertainty due to the nonresonance background while the pink band includes the resonance contributions. The dashed vertical line indicates the experimental value of W which is approximately 2.3 GeV. Notice that this kinematic choice unfortunately does not probe the region where the models differ the most.

CHAPTER 5

Proton Charge Radius Puzzle

As discussed in the Introduction, the charge radius is defined as the derivative of the electronic Sachs form factor with respect to the momentum exchange:

$$R_E^2 = \langle r_p^2 \rangle \equiv -6 \frac{dG_E(Q^2)}{dQ^2}\bigg|_{Q^2=0}. \tag{5.1}$$

The charge radius can be extracted from experiments where the Sachs form factor is measured over a range of small Q^2 values and the resulting fit extrapolated down to $Q^2 = 0$.

One experimental technique for probing the charge radius is electron scattering off a proton target. The differential cross section at tree level is given by the Rosenbluth formula,

$$\frac{d\sigma}{d\Omega} = \left(\frac{d\sigma}{d\Omega}\right)\bigg|_{Mott} \frac{\epsilon G_E^2(Q^2) + \tau G_M^2(Q^2)}{\epsilon(1+\tau)}. \tag{5.2}$$

The parameters of the Rosenbluth formula are

$$\epsilon = [1 + 2(1+\tau)\tan^2(\theta/2)]^{-1} \; ; \; \tau = Q^2/(4M^2), \tag{5.3}$$

where θ is the scattering angle of the electron.

The most recent scattering experiment was conducted at Mainz [54]. They recorded 1400 cross sections of scattering events ranging from $Q^2 = 0.004 - 1$ GeV^2. and obtained a charge radius of 0.879(8) fm.

A more precise measurement can be made by measuring the Lamb shift in hydrogen. The Lamb shift is caused by quantum field corrections to the 2S and 2P energy levels. CODATA [5] combined the published Lamb Shift and ep scattering measurements and quote a proton charge radius of $R_E = 0.8775(51)$ fm.

It has long been a dream to use muonic hydrogen to measure the charge radius of the proton. Since the Bohr radius is inversely proportional to lepton mass, the muon orbitals are roughly 200 times closer to the proton and are more sensitive to proton size effects.

Pohl *et al.* [6] measured the Lamb Shift between the energy levels $2S_{1/2}^{F=1} - 2P_{3/2}^{F=2}$ of muonic hydrogen. Their measured Lamb Shift was compared to the Standard Model prediction

$$\Delta E = 209.9779(49) - 5.2262 R_E^2 + 0.0347 R_E^3 \text{ meV}. \tag{5.4}$$

In the above expression, R_E is in fermi. Vacuum polarization (also referred to as the Uehling potential) is the largest contributor to the Lamb shift because the Compton wavelength for electrons is at same scale as the Bohr radius for muons. The one loop vacuum polarization contributes 205 meV and was calculated, along with many other corrections, by Pachucki [55, 56]. Other important calculations for the Standard Model prediction were performed by Martynenko [57, 58] and Borie [59].

Pohl and collaborators first reported charge radius measurement was $R_E = 0.84184(67)$ fm. The most recently reported charge radius from their collaboration is $R_E = 0.84087(39)$ fm [7]. Both values are 7σ smaller than the CODATA value. The discrepancy could be due to missing Standard Model corrections. It could also be due to the presence of New Physics that is wrongly attributed to Standard Model corrections. To bring the charge radius determined by muonic hydrogen into agreement with the radius obtained from electronic hydrogen measurements, New Physics must lower the Lamb shift by 310 μeV. Compared to the measured muonic Lamb Shift of 206.2949(32) meV, this discrepancy is about 1500 ppm.

5.1 New Physics Solutions to the Proton Charge Radius Puzzle

There have been several proposals to explain the discrepancy. The muon also has another well-known discrepancy between the measured and theoretical $(g-2)_\mu$. The experimental results [60, 61] and latest theory [62] calculation are expressed as $F_2(0) = a_\mu = (g-2)_\mu/2$,

$$\begin{aligned} a_\mu(\text{data}) &= (116\,592\,089 \pm 63) \times 10^{-11} \quad [0.5 \text{ ppm}], \\ a_\mu(\text{thy.}) &= (116\,591\,840 \pm 59) \times 10^{-11} \quad [0.5 \text{ ppm}], \\ \delta a_\mu &= (249 \pm 87) \times 10^{-11} \quad [2.1 \text{ ppm} \pm 0.7 \text{ ppm}]. \end{aligned} \tag{5.5}$$

It is desirable to introduce new models that account for both discrepancies. However, the scale of the $(g-2)_\mu$ discrepancy is roughly one thousand times smaller than that of the proton charge radius. It is a challenge to explain both discrepancies simultaneously.

Several groups have looked into the proton charge radius problem. Jaeckel and Roy [63] considered the possibility that a dark photon could be responsible. This new $U(1)$ gauge boson kinetically mixes with hypercharge. They pointed out that dark photons which couple equally to both electrons and muons could not explain the discrepancy. In this model the electron shift would actually be greater for ordinary hydrogen.

Tucker-Smith and Yavin [64] considered two models that introduced a scalar or vector particle that preferentially couples to muons. They first used the $(g-2)_\mu$ discrepancy to find the couplings as a function of particle mass. They then plotted the resulting energy shift as a function of mass. Their model found that masses of order 1 MeV "explain" both discrepancies. The details of their analysis overlap with our own and can be deduced from the discussion of our model.

Batell *et al.* [65] modified the dark photon model by including an additional coupling to right-handed muons. Their model also required a new particle with scalar coupling to match the muon anamolous magnetic moment discrepancy.

Barger *et al.* wrote a couple of papers [66, 67] pointing out further constraints model-makers need to consider. The first paper covered meson decay constraints placed by Υ, J/ψ, π, and η decays. The second focused on the Batell *et al.* model and pointed out that kaon decays would put severe limitations on the model for dark photons that decay invisibly. The Batell *et al.* model's dark photon mixes with ordinary electrodynamics and is unaffected by the kaon decay constraint.

It has recently been proposed that the proton charge radius puzzle could be due to extra dimensions [68].

5.2 Our Model

5.2.1 Coupling Constraints placed by the Proton Charge Radius Puzzle.

We considered two models to account for the charge radius puzzle, $(g-2)_\mu$, and the kaon constraint [69]. Like Tucker-Smith and Yavin, our two models contain a scalar and vector particle, respectively. These couplings are chosen to account for the energy shift needed to solve the proton charge radius problem. In addition, the scalar particle also has a pseudoscalar partner particle with its coupling fine-tuned to account for the $(g-2)_\mu$ discrepancy. Likewise, the vector particle has an axial vector particle with fine-tuned coupling. The kaon decay constraint is applied to each model and provides mass bounds for the particles.

The Lagrangian for scalar and pseudoscalar particles coupled to a proton and muon is given by

$$\begin{aligned}\mathcal{L}_S = &- C_S^\mu \phi \bar{\psi}_\mu \psi_\mu - iC_P^\mu \varphi \bar{\psi}_\mu \gamma_5 \psi_\mu \\ &- C_S^p \phi \bar{\psi}_p \psi_p - iC_P^p \varphi \bar{\psi}_p \gamma_5 \psi_p,\end{aligned} \tag{5.6}$$

where ϕ is a scalar, φ is a pseudoscalar field, and ψ are fermion fields identified by their subscripts.

Muonic hydrogen is a bound system and therefore can be treated nonrelativistically. At low momentum, $\bar{\psi}\gamma^5\psi \to 0$. Thus, interactions between the muon and proton occur almost solely through the exchange of a scalar particle. The energy shift needed to solve the proton charge radius problem can be used to constrain the strength of the scalar coupling.

The energy shift is found using the Born approximation. The amplitude for scalar particle exchange is

$$i\mathcal{M} = -C_S^\mu C_S^p \frac{i}{q^2 - m_\phi^2} \bar{u}_\mu u_\mu \bar{u}_p u_p \tag{5.7}$$

where m_ϕ is the mass of the scalar particle. The Born approximation allows us to identify the potential energy in momentum space as

$$\Delta\tilde{V}(\vec{q}) = \frac{-C_S^\mu C_S^p}{|\vec{q}|^2 + m_\phi^2} \tag{5.8}$$

Performing a Fourier transformation yields the Yukawa-type potential

$$\Delta V(r) = -\frac{C_S^\mu C_S^p}{4\pi r} e^{-m_\phi r}. \tag{5.9}$$

The energy shift between the 2S and 2P radial wave functions is given by

$$\Delta E_{2S-2P} = \int r^2 dr \Delta V(r)(R_{20}^2 - R_{21}^2). \tag{5.10}$$

The radial wave functions are

$$\begin{aligned} R_{20} &= \frac{1}{(2a)^{3/2}}\left(2 - \frac{r}{a}\right)e^{-r/2a} \\ R_{21} &= \frac{1}{(2a)^{3/2}}\frac{r}{\sqrt{3}a}e^{-r/2a} \end{aligned} \tag{5.11}$$

where $a = 1/(m_r\alpha)$ is the Bohr radius and m_r is the reduced mass of muonic hydrogen. The result of of the integral is

$$\Delta E_{2S-2P} = -\frac{C_S^\mu C_S^p}{4\pi}\frac{1}{2a^3 m_\phi^2}\frac{(am_\phi)^4}{(1+am_\phi)^4}. \tag{5.12}$$

Eq. (5.12) highlights the key point made by Jaeckel and Roy. Electrons have a larger Bohr radius than muons, so models with new particles that couple equally to both electrons and muons cannot explain the proton charge radius puzzle. In a dark photon model electron orbitals would be shifted much more than muon orbitals. New Physics proposals that address the proton charge radius problem must contain additional muon couplings. In other words, lepton universality must be tossed out.

Setting $\Delta E = -310$ μeV to account for the energy shift needed for the muonic hydrogen measurement to comply with electronic measurements of the proton charge radius and making the stipulation $C_S^\mu = C_S^p = C_S$ allows us to determine the coupling strength as a function of particle mass. This function is plotted in Fig. 5.1.

The Lagrangian for our model of new polar and axial vector particles is

$$\begin{aligned}\mathcal{L}_V = &- C_V^\mu \phi^\nu \bar{\psi}_\mu \gamma_\nu \psi_\mu - C_A^\mu \varphi^\nu \bar{\psi}_\mu \gamma_\nu \gamma_5 \psi_\mu \\ &- C_V^p \phi^\nu \bar{\psi}_p \gamma_\nu \psi_p - C_A^p \varphi^\nu \bar{\psi}_p \gamma_\nu \gamma_5 \psi_p. \end{aligned} \tag{5.13}$$

where ϕ^ν is a polar vector and φ^ν is an axial vector field.

Finding the strength of the vector coupling follows similar steps involved with the scalar coupling. The axial vector particle does not contribute to muon-proton interactions in the nonrelativistic limit. The amplitude for the interaction in this model is given by

$$i\mathcal{M} = -C_V^\mu C_V^p \frac{-i}{q^2 - m_\phi^2} \bar{u}_\mu \gamma^\mu u_\mu \bar{u}_p \gamma_\mu u_p. \tag{5.14}$$

The only difference in the potential energies of the two models is a sign. Fig. 5.2 shows the vector couplings strength, $C_V^\mu = -C_V^p = C_V$ needed to account for the 310 μeV shift as a function of particle mass.

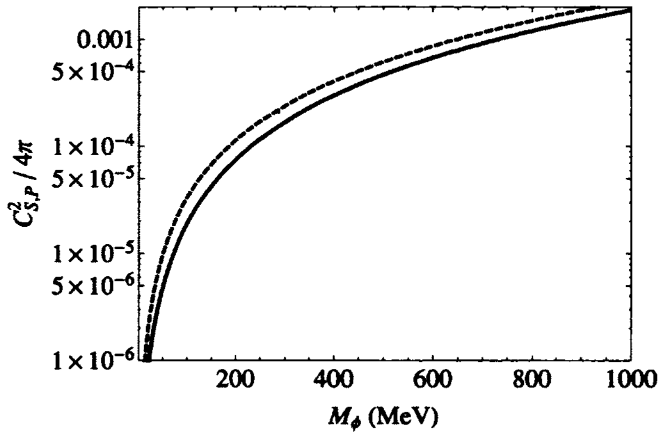

FIG. 5.1: The scalar and pseudoscalar couplings needed to satisfy the experimental constraints. The scalar coupling (solid line) is required to give an extra 310 μeV to the muonic hydrogen 2S-2P Lamb shift. The dashed line is the pseudoscalar coupling needed to satisfy the constraint placed by the muon anomalous moment. We assume the two particle masses are identical.

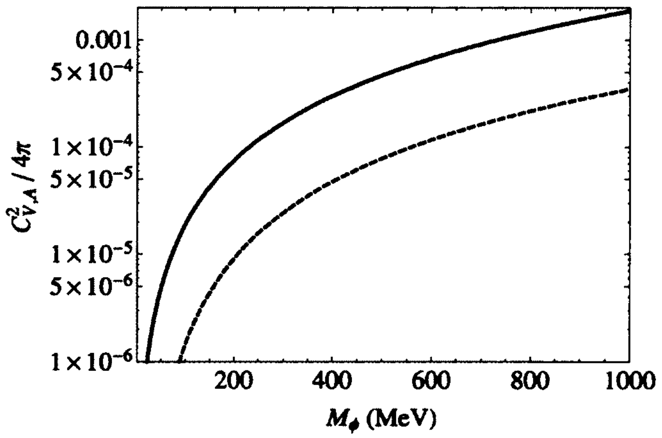

FIG. 5.2: The polar and axial vector couplings needed to satisfy the experimental constraints. The vector coupling (solid line) is required to give an extra 310 μeV to the muonic hydrogen 2S-2P Lamb shift. The dashed line is the axial coupling needed to satisfy the constraint placed by the muon anomalous moment. We assume the two particle masses are identical.

5.2.2 Coupling Constraints placed by the Muon's Anomalous Magnetic Moment.

Since our model contains couplings to muons, it will contribute to δa_μ. As we will show, the scalar (vector) and pseudoscalar (axial vector) couplings enter the expression for the anomalous magnetic moment with opposite signs. This fortuitous situation allows us to fine tune the coupling strength of the pseudoscalar (axial vector) couplings to account for δa_μ.

To simplify our model we choose identical masses for the scalar (vector) and pseudoscalar (axial vector) particles.

The new particles contribute to the anomalous magnetic moment at one loop order as shown in Fig. 5.3. This amplitude can be expressed in terms of form factors,

$$\bar{u}(p_2)\delta\Gamma_\mu u(p_1) = \bar{u}(p_2)\left(\gamma_\mu F_1(Q^2) + \frac{i\sigma_{\mu\nu}}{2M}q^\nu F_2(Q^2)\right)u(p_1)|_{Q^2\to 0} \tag{5.15}$$

We do not need to evaluate the entire amplitude to extract $F_2(0)$. From Eqs. (5.15) we see that terms proportional to γ^μ contribute to F_1 and can be dropped. In fact, we only need to keep terms proportional to $(p_1 + p_2)^\mu$. An examination of the Gordon identity,

$$\bar{u}(p_2)\gamma_\mu u(p_1) = \bar{u}(p_2)\left(\frac{(p_1 + p_2)_\mu}{2M} + \frac{i\sigma_{\mu\nu}}{2M}q^\nu\right)u(p_1), \tag{5.16}$$

reveals that $(p_1 + p_2)^\mu$ can be substituted in favor of $-\frac{i\sigma_{\mu\nu}}{2M}q^\nu$ (the γ^μ term is associated with F_1 and can be dropped). Thus, terms proportional to $(p_1 + p_2)^\mu$ are identified as F_2.

A loop involving our scalar and pseudoscalar particles has an amplitude

$$\bar{u}(p_2)\delta\Gamma^\mu u(p_1) = \bar{u}(p_2)\int \frac{d^dk}{(2\pi)^2}\frac{i}{k^2-m_\phi^2}(-iC_S+C_P\gamma^5)\frac{i(\not{p}_2-\not{k}+m_\mu)}{(p_2-k)^2-m_\mu^2}$$
$$\times\gamma^\mu\frac{i(\not{p}_1-\not{k}+m_\mu)}{(p_1-k)^2-m_\mu^2}(-iC_S+C_P\gamma^5)u(p_1). \tag{5.17}$$

Using FFF and redefining our momentum variable as $l = k - xp_1 - yp_2$, the amplitude becomes

$$\bar{u}(p_2)\delta\Gamma^\mu u(p_1) = \bar{u}(p_2)\int dxdydz2\delta(x+y+z-1)\int\frac{d^dl}{(2\pi)^2}\frac{i}{(l^2-\Delta)^3}$$
$$\times(-iC_S+C_P\gamma^5)i(\not{p}_2-\not{k}+m_\mu)\gamma^\mu i(\not{p}_1-\not{k}+m_\mu)(-iC_S+C_P\gamma^5)u(p_1), \tag{5.18}$$

where $\Delta = -xyq^2 + zm_\phi^2 + (1-z)^2m_\mu^2$.

Because of the symmetry of the integrals in Eq. (5.18), we can substitute $x, y \to 1/2(x+y)$. Keeping only terms proportional to p_1^μ and p_2^μ, the remaining term is

$$\bar{u}(p_2)\delta\Gamma^\mu u(p_1)|_{p_1,p_2} = \bar{u}(p_2)\int dxdydz2\delta(x+y+z-1)\int\frac{d^dl}{(2\pi)^2}\frac{1}{(l^2-\Delta)^3}$$
$$\times(-im_\mu)(p_1+p_2)^\mu\left[C_S^2(1-z^2)-C_P^2(1-z)^2\right]u(p_1), \tag{5.19}$$

Performing the substitution $(p_1+p_2)^\mu = -\frac{i\sigma_{\mu\nu}}{2M}q^\nu$ we find

$$F_2(0)|_{S,P} = \frac{m_\mu^2}{8\pi^2}\int_0^1 dz\frac{C_S^2(1-z)^2(1+z)-C_P^2(1-z)^3}{zm_\phi^2+(1-z)^2m_\mu^2}. \tag{5.20}$$

Fig. 5.1 plots the strength of C_P needed to produce the anomalous magnetic moment discrepancy as a function of particle mass.

In $\xi = 1$ gauge a loop involving our polar and axial vector particles has two amplitudes.

The first is

$$\bar{u}(p_2)\delta\Gamma^\mu u(p_1) = \bar{u}(p_2)\int \frac{d^dk}{(2\pi)^2}\frac{-i}{k^2-m_\phi^2}\gamma^\nu(-iC_V - iC_A\gamma^5)\frac{i(\not{p}_2 - \not{k} + m_\mu)}{(p_2-k)^2-m_\mu^2}$$
$$\times\gamma^\mu\frac{i(\not{p}_1 - \not{k} + m_\mu)}{(p_1-k)^2-m_\mu^2}\gamma_\nu(-iC_V - iC_A\gamma^5)u(p_1). \tag{5.21}$$

Redefining our momentum variable as $l = k - xp_1 - yp_2$, the amplitude becomes

$$\bar{u}(p_2)\delta\Gamma^\mu u(p_1) = \bar{u}(p_2)\int dxdydz2\delta(x+y+z-1)\int\frac{d^dl}{(2\pi)^2}\frac{1}{(l^2-\Delta)^3}(-i)\gamma^\nu$$
$$\times(-iC_V - iC_A\gamma^5)i(\not{p}_2 - \not{k} + m_\mu)\gamma^\mu i(\not{p}_1 - \not{k} + m_\mu)(-iC_V - iC_V\gamma^5)u(p_1), \tag{5.22}$$

where $\Delta = -xyq^2 + zm_\phi^2 + (1-z)^2m_\mu^2$.

Exploiting the same x, y symmetry as in the scalar case and keeping only terms proportional to p_1^μ and p_2^μ, the remaining term is

$$\bar{u}(p_2)\delta\Gamma^\mu u(p_1)|_{p_1,p_2} = \bar{u}(p_2)\int dxdydz2\delta(x+y+z-1)\int\frac{d^dl}{(2\pi)^2}\frac{1}{(l^2-\Delta)^3}$$
$$\times(-2im_\mu)(p_1+p_2)^\mu\left[C_V^2(z-z^2) - C_A^2(3z+z^2)\right]u(p_1), \tag{5.23}$$

Performing the substitution $(p_1+p_2)^\mu = -\frac{i\sigma_{\mu\nu}}{2M}q^\nu$ we find the contribution of the first diagram to $F_2(0)$ to be

$$F_2(0)|_{\text{1st term}} = \frac{m_\mu^2}{4\pi^2}\int_0^1 dz\frac{C_V^2z(1-z)^2 - C_A^2z(3+z)(1-z)}{zm_\phi^2 + (1-z)^2m_\mu^2}. \tag{5.24}$$

Next, we calculate the loop due to the Goldstone boson:

$$\bar{u}(p_2)\delta\Gamma^\mu u(p_1) = \bar{u}(p_2)\int \frac{d^dk}{(2\pi)^2}\frac{i}{k^2-m_\phi^2}\Big(\frac{2m_\mu}{m_\phi}\Big)\gamma^5\frac{i(\not{p}_2-\not{k}+m_\mu)}{(p_2-k)^2-m_\mu^2}$$
$$\times\,\gamma^\mu\frac{i(\not{p}_1-\not{k}+m_\mu)}{(p_1-k)^2-m_\mu^2}\Big(\frac{2m_\mu}{m_\phi}\Big)\gamma^5 u(p_1). \qquad (5.25)$$

The Goldstone boson's contribution to $F_2(0)$ is

$$F_2(0)|_{GB} = -\frac{m_\mu^2}{4\pi^2}\int_0^1 dz\frac{2m_\mu^2}{m_\phi^2}\frac{C_A^2(1-z)^3}{zm_\phi^2+(1-z)^2m_\mu^2}. \qquad (5.26)$$

The total contribution of new vector and axial vector particles to the muon's anomalous magnetic moment is

$$F_2(0)|_{V,A} = \frac{m_\mu^2}{4\pi^2}\int_0^1 dz\frac{1}{zm_\phi^2+(1-z)^2m_\mu^2}\{C_V^2z(1-z)^2$$
$$-\,C_A^2\big[z(3+z)(1-z)+\frac{2m_\mu^2}{m_\phi^2}(1-z)^3\big]\}. \qquad (5.27)$$

Fig. 5.2 plots the strength of C_A needed to produce the anomalous magnetic moment discrepancy as a function of particle mass.

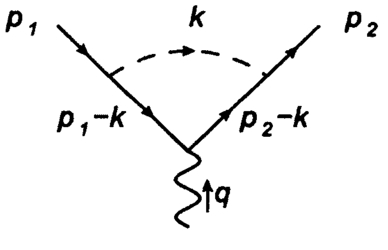

FIG. 5.3: One-loop magnetic moment correction

5.2.3 Mass Constraints placed by Kaon Decay.

Barger *et al.* [67] brought attention to another model constraint due to kaon decay. Pang *et al.* [70] performed a search for $K^+ \to \mu^+ \nu\bar{\nu}\nu$. They generalized their experimental limit to apply it to any decay $K \to \mu\nu X$, where X is a neutral particle (see Fig. 5.4, where the invisible particle X is our new particle ϕ). We can use this limit to place mass constraints on our new particles. The Pang *et al.* limit is

$$\frac{1}{\Gamma(K \to \mu\nu)} \int \frac{d\Gamma(K \to \mu\nu X)}{dE_\mu} D(T_\mu)\, dE_\mu < 2 \times 10^{-6}, \tag{5.28}$$

where E_μ is the energy of the muon and $D(T_\mu)$ is their detector efficiency as a function of the muon's kinetic energy. Their detector had variable sensitivity to muons with kinetic energy between 60-100 MeV. We had to deduce an analytic expression for $D(T_\mu)$ by examining their plot for their efficiency. The expression we used was

$$D(T_\mu) = \frac{1}{1650}(T_\mu - 60)(100 - T_\mu)^{1.5}\Theta(T_\mu - 60)(1 - \Theta(T_\mu - 100)). \tag{5.29}$$

The denominator contains the simple $K \to \mu\nu$ decay rate

$$\Gamma(K \to \mu\nu) = \frac{G_F^2 f_K^2 V_{us}^2}{4\pi m_K^3} m_\mu^2 \left(m_K^2 - m_\mu^2\right)^2. \tag{5.30}$$

The kaon decay constant, f_k, is defined from

$$\langle 0|\, \bar{u}\gamma_\mu(1 - \gamma_5)s\, |K\rangle = \sqrt{2} f_K k_\mu . \tag{5.31}$$

Note that many groups define the decay constant without the factor of $\sqrt{2}$. The convention used must be checked when comparing to the results of other calculations.

Three body decay is given by the well known expression

$$\Gamma(K \to \mu\nu\phi) = \frac{1}{64\pi^3 m_K} \int dE_\mu \, dE_\nu \sum_{\text{spins}} |\mathcal{M}|^2 \,, \tag{5.32}$$

with integration limits

$$m_\mu \leq E_\mu \leq \frac{m_K^2 + m_\mu^2 - m_\phi^2}{2m_K} \,, \tag{5.33}$$

and

$$\left\{ \begin{array}{c} max \\ min \end{array} \right\} E_\nu = \frac{m_K^2 + m_\mu^2 - m_\phi^2 - 2m_K E_\mu}{2\left(m_K - E_\mu \mp \sqrt{E_\mu^2 - m_\mu^2}\right)} \,. \tag{5.34}$$

The matrix element for the decay into a muon, neutrino, and particle with both scalar and pseudoscalar couplings is

$$\begin{aligned} \mathcal{M}_{S,P} = & -\frac{G_F f_K V_{us}}{Q^2 - m_\mu^2} \bar{u}(l) \\ & \times \left[(C_S - iC_P)Q^2 + m_\mu(C_S + iC_P) \not{k}\right] (1 - \gamma_5) v(q) \,, \end{aligned} \tag{5.35}$$

where $Q^2 = (k - q)^2 = m_K^2 - 2m_K E_\nu$.

The matrix element squared and summed is

$$\begin{aligned} \sum_{\text{spins}} |\mathcal{M}_{S,P}|^2 = \frac{4G_F^2 f_K^2 V_{us}^2}{(Q^2 - m_\mu^2)^2} \Big\{ & (C_S^2 + C_P^2) \\ & \times \Big[2m_K E_\mu Q^2 (Q^2 - m_\mu^2) \\ & - (Q^4 - m_\mu^2 m_K^2)(Q^2 + m_\mu^2 - m_\phi^2)\Big] \\ & + 2(C_S^2 - C_P^2)\, m_\mu^2 Q^2 (m_K^2 - Q^2) \Big\} \,. \end{aligned} \tag{5.36}$$

Plugging Eq. (5.36) into Eq. (5.28) places mass constraints on the new scalar-pseudoscalar particle. Fig. 5.5 shows the range of masses allowed by the kaon decay measurement. Masses between 100-200 MeV are not allowed.

We began our kaon decay analysis by assuming the presence of one new particle with both scalar and pseudoscalar couplings. However, the squared amplitude of Eq. (5.36) does not contain any coupling cross terms and we are also free to interpret this result as describing a new scalar particle and pseudoscalar particle with equal mass.

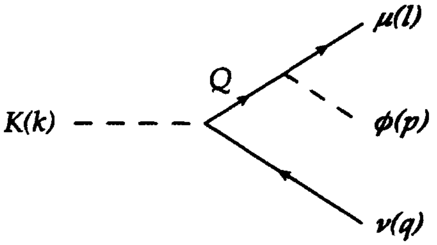

FIG. 5.4: Kaon decay into a muon, neutrino, and new particle, ϕ. Q is the intermediate momentum of the muon.

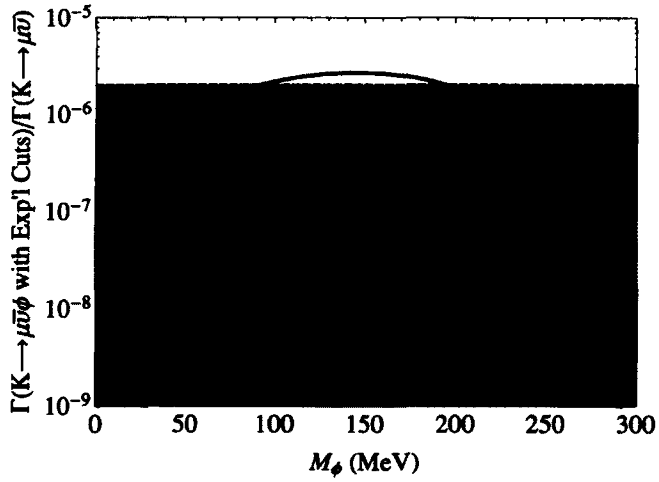

FIG. 5.5: Mass limits on scalar and pseudoscalar particles due to constraints placed by $K \rightarrow \mu\nu X$ searches. The solid curve is the full result, accounting for the experimental efficiency, obtained through satisfying the Lamb shift and magnetic moment criteria. The contributions of the scalar (dashed curve) and pseudoscalar (dash-dotted curve) couplings are indicated separately. The experimental limit is the horizontal line, and the shaded region is allowed.

The matrix element for the decay into a muon, neutrino, and a particle with both polar and axial vector couplings is

$$
\begin{aligned}
\mathcal{M}_{V,A} = & \frac{G_F f_K V_{us}}{Q^2 - m_\mu^2} \epsilon_\nu \bar{u}(l) \gamma^\nu \\
& \times \left[(C_V - C_A) Q^2 + m_\mu (C_V + C_A) \not{k} \right] (1 - \gamma_5) v(q) \, ,
\end{aligned}
\tag{5.37}
$$

where ϵ_ν is the polarization vector of the new particle. The square of this amplitude is

$$
\begin{aligned}
\sum_{\textbf{spins}} |\mathcal{M}_{V,A}|^2 = & \frac{8 G_F^2 f_K^2 V_{us}^2}{(Q^2 - m_\mu^2)^2} \Big\{ (C_V - C_A)^2 Q^4 \Big[m_k E_\mu \big(1 - \frac{1}{m_\phi^2}(Q^2 - m_\mu^2 - m_\phi^2)\big) \\
& - \frac{1}{2}(Q^2 - m_\phi^2)\big(1 - \frac{1}{m_\phi^2}(m_\mu^2 + m_k^2 - m_\phi^2)\big) \\
& - \frac{1}{2} m_\mu^2 \big(1 - \frac{1}{m_\phi^2}(m_\mu^2 + m_k^2 - m_\phi^2)\big) \Big] \\
& + (C_V + C_A)^2 m_\mu^2 \Big[m_k Q^2 (\frac{1}{2} m_k - E_\mu) + \frac{1}{2} m_k^2 (m_\mu^2 - m_\phi^2) \\
& + \frac{1}{m_\phi}^2 (Q^2 - m_\mu^2 - m_\phi^2) \times \big(Q^2 (m_k E_\mu - \frac{1}{2} Q^2) - \frac{1}{2} m_k^2 (m_\mu^2 - m_\phi^2)\big) \Big] \\
& - 3 (C_V^2 - C_A^2) m_\mu^2 Q^2 (m_k^2 - Q^2) \Big\} \, .
\end{aligned}
\tag{5.38}
$$

Plugging Eq. (5.38) into Eq. (5.28) places mass constraints on the new polar-axial vector particle. Fig. 5.6 shows the range of masses allowed by the kaon decay measurement. Masses below about 160 MeV are not allowed.

To consider a model where we have new polar and axial particles of equal mass, all we must do is eliminate the coupling cross terms in the amplitude squared. The blue, dashed curve describes the predicted decay ratio for such a model. Masses below about 220 MeV are not allowed.

New particles with fine-tuned scalar and pseudoscalar (vector and axial vector) couplings can "explain" the proton charge radius puzzle while satisfying constraints placed by $(g-2)_\mu$ and kaon decays. In the next chapter we will discuss the possibility of further kaon decay constraints from an upcoming experiment at the Japanese Proton Accelerator Research Complex.

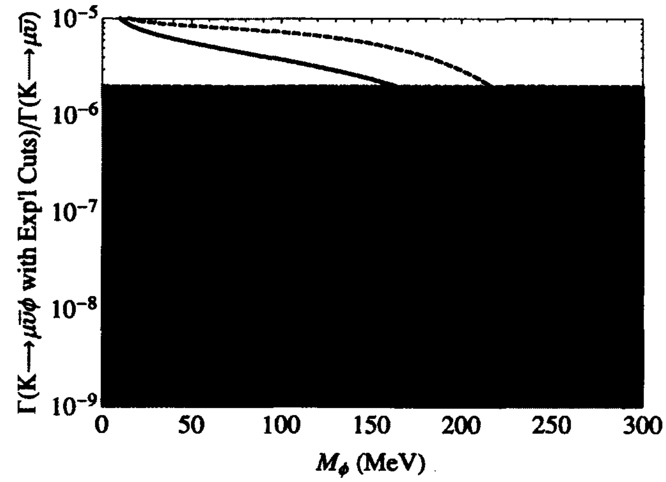

FIG. 5.6: Mass limits on polar and axial vector particles due to constraints placed by $K \to \mu\nu X$ searches. The solid curve is the result for a single particle with both polar and axial vector couplings, accounting for the experimental efficiency, obtained through satisfying the Lamb shift and magnetic moment criteria. The dashed curve is the result for separate polar and axial vector particles with equal masses. The experimental limit is the horizontal line, and the shaded region is allowed.

CHAPTER 6

Concluding Remarks

As demonstrated in Chap. 4, present experiments are insufficient to produce accurate fits for $F^{\gamma Z}_{1,2,3}(x,Q^2)$. The Qweak collaboration must use γZ box calculations dependent on models for $F^{\gamma Z}_{1,2}(x,Q^2)$ [27, 28, 29, 30] and $F^{\gamma Z}_{3}(x,Q^2)$ [31, 33]. I am of course biased that our model is the best, but the close agreement of the models suggests the collaboration will be equally well-served using any model or an average of models. In Sec. 6.1 we discuss whether these models and their uncertainties are acceptable for the next generation of low energy, weak charge measurements.

The present New Physics models for the proton charge radius problem [64, 65, 69] are speculative and must be confronted by more experimental constraints. It is also still unclear if the proton charge radius puzzle is the result of overlooked Standard Model processes. Sec. 6.2 provides details of future measurements of the proton charge radius and upcoming experimental constraints for New Physics models.

6.1 Future Measurements of the Proton's Weak Charge.

The Mainz P2 experiment plans on performing a 2% measurement of the weak charge by scattering polarized electrons of $E \approx 200$ MeV [71]. This error budget is half that of the Qweak experiment. At this energy, our vector model gives 0.00125 ± 0.00018 [28]. Adding in our axial model calculation, the total box value is

$$\mathrm{Re}\,\Box_{\gamma Z}(E = 200\text{ MeV})|_{\text{total}} = (5.8 \pm 0.7) \times 10^{-3}. \tag{6.1}$$

Based on Fig. 2 of [31], their prediction for the P2 experiment is about

$$\mathrm{Re}\,\Box_{\gamma Z}(E = 200\text{ MeV})|_{\text{total}} = (5.4 \pm 0.5) \times 10^{-3}. \tag{6.2}$$

A 2% measurement of the proton's weak charge at one loop order has an error budget of about 0.0014. Both fits are within the uncertainty allocations, but it is desirable to reduce them.

It is unlikely that the resonance coefficients uncertainties for our constituent quark model can be greatly reduced. The greatest reduction is probably in the resonance background. Our current background is found by averaging the valence quark and sea quark limits, and these limits are used as the uncertainty bounds.

Ideally, we would like to do away with models for γZ structure functions and instead rely on fits to data. The PVDIS experiment [52] represents a first attempt to constrain the deuteron version of these structure functions. However, this experiment was only conducted at four kinematic points. To construct fits, a wide range of Q^2 will have to be measured. A new PVDIS experiment will be run after JLAB's 12 GeV upgrade [4]. The plan is to measure electrons scattering off a deuteron target for several kinematics ranging from x from 0.3 to 0.7 and Q^2 from 5 to 10 GeV^2. This data could be used to constrain

$F_{1,2,3}^{\gamma Z}(x, Q^2)$ models at moderate Q^2. Unfortunately, the new PVDIS experiment will not probe the resonance region.

6.2 Future Tests of Proton Charge Radius Puzzle.

6.2.1 μp Scattering Determination of the Proton Charge Radius at PSI.

There are two independent techniques to extract the proton's charge radius using leptons. One can either measure lepton scattering or the Lamb shift of the lepton's atomic orbitals. Both techniques have been utilized for electrons and the most recent extractions [54, 5] have found proton charge radius values that agree within uncertainties. For muons, only the Lamb Shift has been measured and the extracted proton charge radius is 7σ smaller than the electronic measurements [6, 7]. It is of obvious interest to see if the puzzle persists in measurements using muon scattering.

The MUon proton Scattering Experiment (MUSE) [72] at the Paul Sherrer Institut seeks to measure the proton's charge radius using muon elastic scattering. MUSE was approved in January 2013 and has a goal of system tests in late 2015. Once operational, MUSE will perform simultaneous measurements of *ep* and μp elastic scattering. The system will be able to scatter both $+$ and $-$ charged leptons. It is important to measure the cross sections of both charged leptons to separate 2-photon effects from G_E. A large range of kinematics will be measured using beam momenta of 115 MeV, 153 MeV, and 210 MeV.

6.2.2 Testing Charge Radius Puzzle Models at JPARC.

There are currently three models for the proton charge radius puzzle that involve the introduction of new, lepton universality-violating particles [64, 65, 69]. A new kaon decay experiment, E36, at the Japan Proton Accelerator Research Complex (JPARC) may be used to eliminate or constrain these models [73]. The main goal of the experiment is to measure the ratio $\Gamma(K^+ \to \mu^+ + \nu_\mu)/\Gamma(K^+ \to e^+ + \nu_e)$. They expect to see 10^{10} $K^+ \to \mu^+ + \nu_\mu$ events [74]. The branching ratio for this decay channel is 0.6355 [2].

Of particular interest for new particle searches is the decay channel $K^+ \to \mu^+ + \nu_\mu + e^+ + e^-$. Fig. 6.1 shows the lowest order diagrams for Standard Model QED. The full branching ratio for this decay channel is calculated to be 2.49×10^{-5} [75]. For their expected 50% acceptance of e^+e^- coincidences, the total number of such decays E36 can expect is

$$\begin{aligned} N(K^+ &\to \mu^+ + \nu_\mu + e^+ + e^-) \\ &= \frac{1}{2}\frac{\Gamma(K^+ \to \mu^+ + \nu_\mu + e^+ + e^-)}{\Gamma(K^+ \to \mu^+ + \nu_\mu)} N(K^+ \to \mu^+ + \nu_\mu) \\ &\approx 2 \times 10^5. \end{aligned} \tag{6.3}$$

If no new particles are present, there will be about 1000 such events per bin (bin size of 1 MeV) in the vicinity of $m_{ee} = 30$ MeV. Here, m_{ee} is the energy of the e^+e^- pair. The amplitude for the QED prediction is

$$i\mathcal{M} = -\frac{G_F}{\sqrt{2}}(-ie)^2 V_{us}\bar{u}(p_1)\gamma_\rho v(p_2)\frac{-i}{q'^2}(\sqrt{2}f_k m_\mu L^\rho - H^{\rho\nu}j_\nu) \tag{6.4}$$

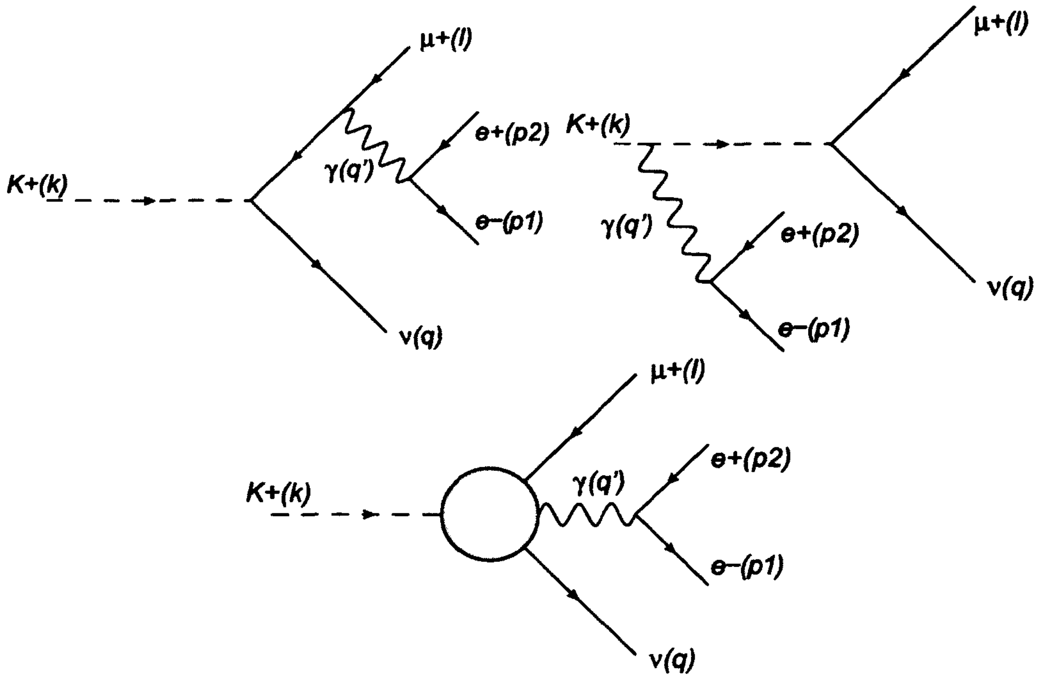

FIG. 6.1: QED background for $K^+ \to \mu^+ + \nu_\mu$.

where

$$
\begin{aligned}
L^\rho &= \bar{u}(q)(1+\gamma^5)\left(\frac{(2k-q')^\rho}{2k\cdot q' + q'^2} - \frac{2l^\rho + \not{q}'\gamma^\rho}{2l\cdot q' + q'^2}\right)v(l), \\
H^{\rho\nu} &= -iV_1\epsilon^{\rho\nu\alpha\beta}q'_\alpha k_\beta - A_1(q'\cdot(k-q')g^{\rho\nu} - (k-q')^\rho q'^\nu) - A_2(q'^2 g^{\rho\nu} - q'^\rho q'^\nu),
\end{aligned}
\tag{6.5}
$$

and

$$
j_\nu = \bar{u}(q)\gamma_\nu(1+\gamma^5)v(l). \tag{6.6}
$$

Values for V_1, A_1, A_2, and f_k can be found in Poblaguev *et al.* [76]. V_1, A_1, A_2 are given by

$$-\sqrt{2}m_k(A_1, A_2, V_1) = (F_A, R, F_V), \tag{6.7}$$

where $F_A = 0.031$, $R = 0.235$, and $F_V = 0.124$. It is important to note that our normalization of f_k is different from Poblaguev *et al.* Their value of $f_k = 160$ MeV corresponds to $\sqrt{2}f_k$ in our normalization.

A sign of a new particle would be the observation of more events than the QED prediction at some value of m_{ee}. One extension to the Standard Model that will produce more events is the dark photon. As the name suggests, the dark photon shares many properties with the photon of QED. To account for the amplitude of dark photon interactions, the photon's propagator and coupling in Eq. (6.4) are modified:

$$\frac{-i}{q^2} \to \frac{-i}{q^2 - m_{A'}^2 + i m_{A'}\Gamma}, \tag{6.8}$$

$$-ie\gamma^\mu \to -i\epsilon e\gamma^\mu. \tag{6.9}$$

In the above expressions $m_{A'}$ is the mass of the dark photon, Γ is its decay rate into $e^+ + e^-$, and ϵe is its coupling. If a dark photon exists, a bump in the data will be centered around the propagator's pole and will determine the dark photon's mass. The size of the deviation will indicate the value of ϵ. Of course, a lack of deviation from the Standard Model will place constraints on $m_{A'}$ and ϵe.

There are already many experimental constraints on dark photon parameters (see Beranek and Vanderhaeghen [77] for a constraints plot in the low energy region relevant to the JPARC experiment). As an example of JPARC's experimental resolution, we calculated the signal of a dark photon with the currently allowed parameters $m_{A'} = 30$ MeV and $\epsilon = 10^{-3}$. The result is shown in Fig. 6.2. The dotted red curve is the expected signal from QED while the black curve is the signal due to QED and an additional dark photon. The simulated data points possess error bars accounting for the statistical uncertainty of 1000 events per bin. Given the relative size of the bump and error bars, it will be very hard for JPARC to detect the presence of dark photons.

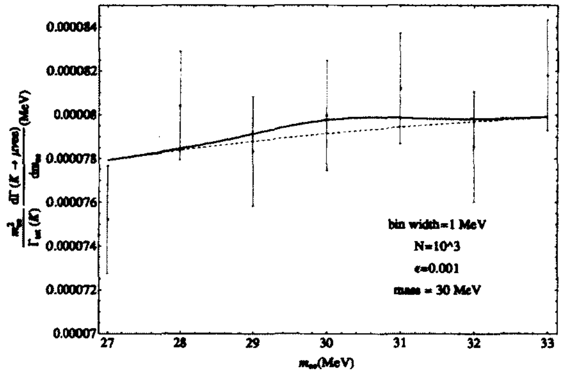

FIG. 6.2: QED prediction for $K^+ \to \mu^+ + \nu_\mu + e^+ + e^-$ (red, dashed curve) and the prediction with an additional dark photon (black curve). Data points are simulated and possess error bars accounting for the statistical uncertainty.

JPARC could be quite sensitive to the lepton universality-violating particles present in proton charge radius puzzle models. The model of Batell *et al.* [65] contains dark photon-esque particles that possess an additional coupling to right-handed muons. To account for this particle's effect on the amplitude $K^+ \to \mu^+ + \nu_\mu + e^+ + e^-$, the photon's propagator and coupling are modified to

$$\frac{-i}{q^2} \to \frac{-i}{q^2 - m_{A'}^2 + i m_{A'} \Gamma}, \tag{6.10}$$

$$-ie\gamma^\mu \to -i\kappa e\gamma^\mu - i\frac{g_R}{2}\gamma^\mu(1+\gamma^5), \tag{6.11}$$

where $m_{A'}$ is the mass of the new particle, Γ is its decay rate into $e^+ + e^-$, and κe is its coupling to all particles, and $g_R/2$ is its additional coupling to right-handed muons. Batell *et al.* give several values of $m_{A'}$, κ, and g_R that they claim satisfy all present constraints.

Fig. 6.3 displays the predictions of their parameter values. This signal is several orders of magnitude greater than the one due to "standard" dark photons. A dark photon with the Batell *et al.* parameters should be detectable.

The particles in our model for the proton charge radius puzzle do not couple to electrons and would not contribute to this decay channel. In future work we may introduce a small electronic coupling to our model and calculate its contribution to $\Gamma(K^+ \to \mu^+ + \nu_\mu + e^+ + e^-)$.

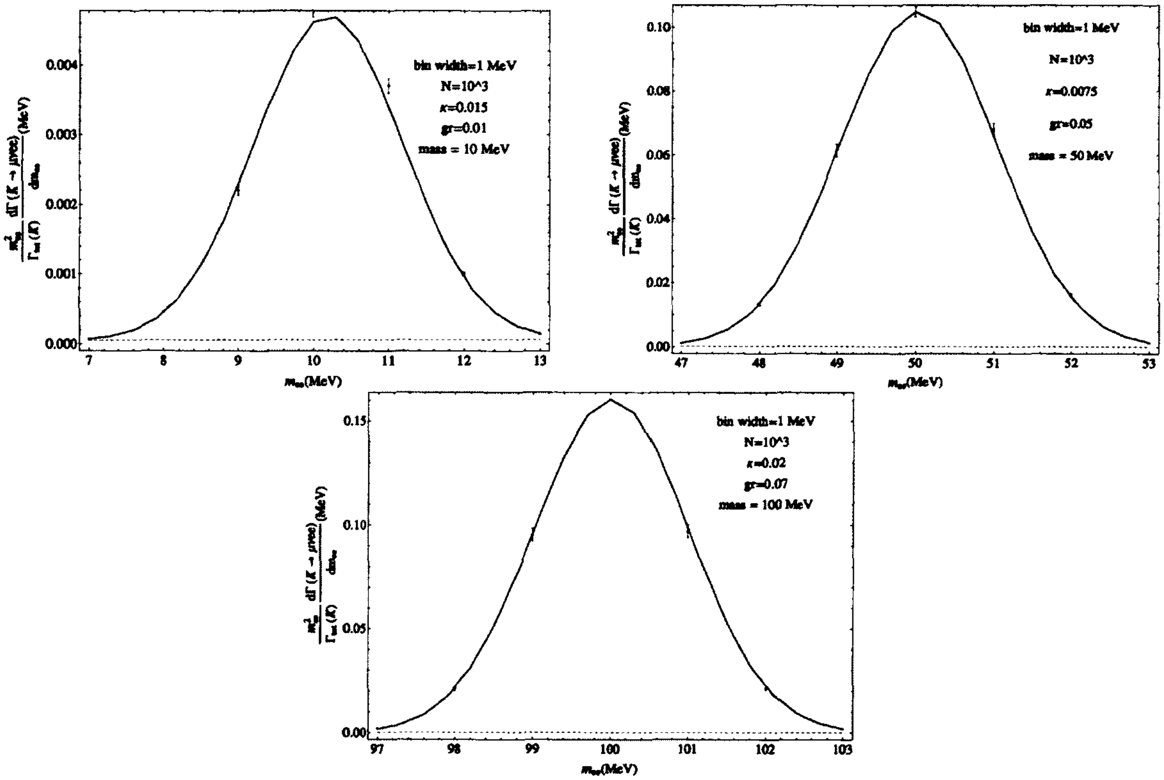

FIG. 6.3: QED prediction for $K^+ \to \mu^+ + \nu_\mu + e^+ + e^-$ (red, dashed curve) and the prediction with the additional lepton-universality violating particle of Batell *et al.* (black curve). Data points are simulated and possess error bars accounting for the statistical uncertainty.

BIBLIOGRAPHY

[1] F. Halzen and A. D. Martin, *Quarks and Leptons: An Introductory Course in Modern Particle Physics* (Wiley, 1984).

[2] Particle Data Group, K. Nakamura *et al.*, J. Phys. **G37**, 075021 (2010).

[3] D. Armstrong *et al.*, (2012), arXiv:1202.1255.

[4] The 12-GeV JLab proposal may be found at http://hallaweb.jlab.org/parity/PR-10-007-SoLID-PVDIS.pdf , with references to earlier 6 GeV proposals therein.

[5] P. J. Mohr, B. N. Taylor, and D. B. Newell, Rev. Mod. Phys. **84**, 1527 (2012), arXiv:1203.5425.

[6] R. Pohl *et al.*, Nature **466**, 213 (2010).

[7] A. Antognini *et al.*, Science **339**, 417 (2013).

[8] ALEPH Collaboration, DELPHI Collaboration, L3 Collaboration, OPAL Collaboration, SLD Collaboration, LEP Electroweak Working Group, SLD Electroweak Group, SLD Heavy Flavour Group, ALEPH Collaboration, DELPHI Collaboration, L3 Collaboration, OPAL Collaboration, SLD Collaboration, LEP Electroweak Working Group, SLD Electroweak Group, SLD Heavy Flavour Group, Phys.Rept. **427**, 257 (2006), arXiv:hep-ex/0509008, 302 pages, v2: minor corrections and updates of references. Accepted for publication by Physics Reports, v3: further small corrections and journal version Report-no: CERN-PH-EP/2005-041, SLAC-R-774.

[9] SAMPLE Collaboration, T. Ito *et al.*, Phys. Rev. Lett. **92**, 102003 (2004), arXiv:nucl-ex/0310001.

[10] SAMPLE Collaboration, D. Spayde *et al.*, Phys. Lett. **B583**, 79 (2004), arXiv:nucl-ex/0312016.

[11] A4 Collaboration, F. Maas *et al.*, Phys. Rev. Lett. **93**, 022002 (2004), arXiv:nucl-ex/0401019.

[12] F. Maas *et al.*, Phys. Rev. Lett. **94**, 152001 (2005), arXiv:nucl-ex/0412030.

[13] HAPPEX Collaboration, K. Aniol *et al.*, Phys. Rev. Lett. **96**, 022003 (2006), arXiv:nucl-ex/0506010.

[14] HAPPEX Collaboration, K. Aniol *et al.*, Phys. Lett. **B635**, 275 (2006), arXiv:nucl-ex/0506011.

[15] G0 Collaboration, D. Armstrong *et al.*, Phys. Rev. Lett. **95**, 092001 (2005), arXiv:nucl-ex/0506021.

[16] J. Erler, A. Kurylov, and M. J. Ramsey-Musolf, Phys. Rev. **D68**, 016006 (2003), arXiv:hep-ph/0302149.

[17] A. Czarnecki and W. J. Marciano, Phys. Rev. **D53**, 1066 (1996), arXiv:hep-ph/9507420.

[18] A. Czarnecki and W. J. Marciano, Int. J. Mod. Phys. **A13**, 2235 (1998), arXiv:hep-ph/9801394.

[19] A. Czarnecki and W. J. Marciano, Int. J. Mod. Phys. **A15**, 2365 (2000), arXiv:hep-ph/0003049.

[20] J. Erler and M. J. Ramsey-Musolf, Phys. Rev. **D72**, 073003 (2005), arXiv:hep-ph/0409169.

[21] W. Marciano and A. Sirlin, Phys. Rev. **D29**, 75 (1984).

[22] A. Ferroglia, G. Ossola, and A. Sirlin, Eur. Phys. J. **C34**, 165 (2004), arXiv:hep-ph/0307200.

[23] G. Degrassi and A. Sirlin, Phys. Rev. **D46**, 3104 (1992).

[24] W. Marciano and A. Sirlin, Phys. Rev. **D22**, 2695 (1980).

[25] W. Marciano and A. Sirlin, Phys. Rev. **D27**, 552 (1983).

[26] M. Gorchtein and C. J. Horowitz, Phys. Rev. Lett. **102**, 091806 (2009), arXiv:0811.0614.

[27] A. Sibirtsev, P. G. Blunden, W. Melnitchouk, and A. W. Thomas, Phys. Rev. **D82**, 013011 (2010), arXiv:1002.0740.

[28] B. C. Rislow and C. E. Carlson, Phys. Rev. **D83**, 113007 (2011), arXiv:1011.2397.

[29] M. Gorchtein, C. Horowitz, and M. J. Ramsey-Musolf, Phys. Rev. **C84**, 015502 (2011), arXiv:1102.3910.

[30] N. Hall, P. Blunden, W. Melnitchouk, A. Thomas, and R. Young, (2013), arXiv:1304.7877.

[31] P. Blunden, W. Melnitchouk, and A. Thomas, Phys. Rev. Lett. **107**, 081801 (2011), arXiv:1102.5334.

[32] P. Blunden, W. Melnitchouk, and A. Thomas, Phys. Rev. Lett. **109**, 262301 (2012), arXiv:1208.4310.

[33] B. C. Rislow and C. E. Carlson, (2013), arXiv:1304.8113.

[34] L. Tiator, D. Drechsel, S. Kamalov, and M. Vanderhaeghen, Eur. Phys. J. ST **198**, 141 (2011), arXiv:1109.6745.

[35] H.-L. Lai *et al.*, Phys. Rev. **D82**, 074024 (2010), arXiv:1007.2241.

[36] A. Capella, A. Kaidalov, C. Merino, and J. Tran Thanh Van, Phys. Lett. **B337**, 358 (1994), arXiv:hep-ph/9405338.

[37] H. Q. Zhou, C. W. Kao, and S. N. Yang, Phys. Rev. Lett. **99**, 262001 (2007), arXiv:0708.4297, Erratum *ibid.* **100**, 059903(E) (2008).

[38] J. A. Tjon, P. G. Blunden, and W. Melnitchouk, Phys. Rev. **C79**, 055201 (2009), arXiv:0903.2759.

[39] M. E. Christy and P. E. Bosted, Phys. Rev. **C81**, 055213 (2010), arXiv:0712.3731.

[40] F. Close, *An Introduction to Quarks and Partons* (Academic Press, 1979).

[41] S. J. Brodsky and G. P. Lepage, Phys. Rev. **D24**, 2848 (1981).

[42] C. E. Carlson, Phys. Rev. **D34**, 2704 (1986).

[43] R. G. Moorhouse, Phys. Rev. Lett. **16**, 772 (1966).

[44] G. Cvetic, D. Schildknecht, B. Surrow, and M. Tentyukov, Eur. Phys. J. **C20**, 77 (2001), arXiv:hep-ph/0102229.

[45] J. Alwall and G. Ingelman, Phys .Lett. **B596**, 77 (2004), arXiv:hep-ph/0402248.

[46] A. D. Martin, W. J. Stirling, R. S. Thorne, and G. Watt, Eur. Phys. J. **C63**, 189 (2009), arXiv:0901.0002.

[47] J. Arrington, W. Melnitchouk, and J. Tjon, Phys. Rev. **C76**, 035205 (2007), arXiv:0707.1861.

[48] O. Lalakulich, E. A. Paschos, and G. Piranishvili, Phys. Rev. **D74**, 014009 (2006), arXiv:hep-ph/0602210.

[49] C. Alexandrou, G. Koutsou, J. Negele, Y. Proestos, and A. Tsapalis, Phys. Rev. **D83**, 014501 (2011), arXiv:1011.3233.

[50] ETM Collaboration, C. Alexandrou *et al.*, Phys. Rev. **D83**, 045010 (2011), arXiv:1012.0857.

[51] C. E. Carlson and B. C. Rislow, Phys. Rev. **D85**, 073002 (2012), arXiv:1201.3323.

[52] D. Wang *et al.*, (2013), arXiv:1304.7741.

[53] P. E. Bosted and M. E. Christy, Phys. Rev. **C77**, 065206 (2008), arXiv:0711.0159.

[54] A1 Collaboration, J. Bernauer *et al.*, Phys. Rev. Lett. **105**, 242001 (2010), arXiv:1007.5076.

[55] K. Pachucki, Phys. Rev. **A53**, 2092 (1996).

[56] K. Pachucki, Phys. Rev. **A60**, 3593 (1999).

[57] A. Martynenko, Phys. Rev. **A71**, 022506 (2005), arXiv:hep-ph/0409107.

[58] A. Martynenko, Phys. Atom. Nucl. **71**, 125 (2008), arXiv:hep-ph/0610226.

[59] E. Borie, Phys. Rev. **A71**, 032508 (2005), arXiv:physics/0410051.

[60] Muon g-2 Collaboration, G. Bennett *et al.*, Phys. Rev. Lett. **92**, 161802 (2004), arXiv:hep-ex/0401008.

[61] B. L. Roberts, Chin. Phys. **C34**, 741 (2010), arXiv:1001.2898.

[62] T. Aoyama, M. Hayakawa, T. Kinoshita, and M. Nio, (2012), arXiv:1205.5370.

[63] J. Jaeckel and S. Roy, Phys. Rev. **D82**, 125020 (2010), arXiv:1008.3536.

[64] D. Tucker-Smith and I. Yavin, Phys. Rev. **D83**, 101702 (2011), arXiv:1011.4922.

[65] B. Batell, D. McKeen, and M. Pospelov, Phys. Rev. Lett. **107**, 011803 (2011), arXiv:1103.0721.

[66] V. Barger, C.-W. Chiang, W.-Y. Keung, and D. Marfatia, Phys. Rev. Lett. **106**, 153001 (2011), arXiv:1011.3519.

[67] V. Barger, C.-W. Chiang, W.-Y. Keung, and D. Marfatia, Phys. Rev. Lett. **108**, 081802 (2012), arXiv:1109.6652.

[68] L.-B. Wang and W.-T. Ni, (2013), arXiv:1303.4885.

[69] C. E. Carlson and B. C. Rislow, Phys. Rev. **D86**, 035013 (2012), arXiv:1206.3587.

[70] C. Pang, R. Hildebrand, G. Cable, and R. Stiening, Phys. Rev. **D8**, 1989 (1973).

[71] K. Kumar, S. Mantry, W. Marciano, and P. Souder, (2013), arXiv:1302.6263.

[72] MUSE Collaboration, R. Gilman *et al.*, (2013), arXiv:1303.2160.

[73] M. Kohl, The TREK/E36 Experiment at J-PARC, 2013, Presented at Workshop to Explore Physics Opportunities with Intense, Polarized Electron Beams up to 300 MeV, Cambridge, MA.

[74] M. Kohl, 2013, private communication.

[75] J. Bijnens, G. Ecker, and J. Gasser, Nucl. Phys. **B396**, 81 (1993), arXiv:hep-ph/9209261.

[76] A. Poblaguev *et al.*, Phys. Rev. Lett. **89**, 061803 (2002), arXiv:hep-ex/0204006.

[77] T. Beranek and M. Vanderhaeghen, Phys. Rev. **D87**, 015024 (2013), arXiv:1209.4561.

VITA

Benjamin Rislow

Benjamin Rislow was born on November 21, 1986. Growing up on a dairy farm provided him ample opportunity to daydream about space exploration (grain bins look a lot like Apollo spacecraft). Poor eyesight and a proclivity for motion sickness forced him to consider alternative scientific careers. After graduating from Lewiston-Altura High School in 2004, he majored in physics at the University of Minnesota, Morris. He finished his bachelor degree in 2008 and entered the physics graduate program at the College of William and Mary. He began working with Dr. Carl Carlson in 2009 on the γZ box calculation. He has also performed calculations for the proton charge radius puzzle. After receiving his Ph.D. he will begin a postdoctoral position in Mainz, Germany.